



**CHALMERS**  
UNIVERSITY OF TECHNOLOGY



UNIVERSITY OF GOTHENBURG

---



# J-factors of Dwarf Spheroidal Galaxies with Self-Interacting Dark Matter

A likelihood-based analysis of  $\gamma$ -ray flux from annihilations of self-interacting dark matter

Bachelor of Science Thesis for the Engineering Physics Programme

Magdalena Eriksson, Björn Eurenus, Susanna Larsson, Rikard Wadman

---

Department of Physics  
CHALMERS UNIVERSITY OF TECHNOLOGY  
UNIVERSITY OF GOTHENBURG  
Gothenburg, Sweden 2017



BACHELOR OF SCIENCE THESIS FOR THE ENGINEERING PHYSICS  
PROGRAMME

## **J-factors of Dwarf Spheroidal Galaxies with Self-Interacting Dark Matter**

A likelihood-based analysis of  $\gamma$ -ray flux from annihilations of self-interacting dark  
matter

MAGDALENA ERIKSSON  
BJÖRN EURENIUS  
SUSANNA LARSSON  
RIKARD WADMAN



Department of Physics  
*Division of Subatomic and Plasma Physics*  
Theoretical Subatomic Physics Group  
CHALMERS UNIVERSITY OF TECHNOLOGY  
UNIVERSITY OF GOTHENBURG  
Gothenburg, Sweden 2017

J-factors of Dwarf Spheroidal Galaxies with Self-Interacting Dark Matter

A likelihood-based analysis of  $\gamma$ -ray flux from annihilations of self-interacting dark matter

MAGDALENA ERIKSSON, BJÖRN EURENIUS, SUSANNA LARSSON, RIKARD WADMAN

© MAGDALENA ERIKSSON, BJÖRN EURENIUS, SUSANNA LARSSON, RIKARD WADMAN,  
2017.

Supervisor: Riccardo Catena, Department of Physics

Examiner: Jan Swensson, Department of Physics

Bachelor's Thesis 2017:TIFX04-17-01

Department of Physics

Division of Subatomic and Plasma Physics

Theoretical Subatomic Physics Group

Chalmers University of Technology

SE-412 96 Gothenburg

Telephone +46 31 772 1000

Cover: Picture of Sculptor dwarf galaxy, taken by the 2.2-meter MPG/ESO telescope [1].

Typeset in L<sup>A</sup>T<sub>E</sub>X

Printed by [Name of printing company]

Gothenburg, Sweden 2017

J-factors of Dwarf Spheroidal Galaxies with Self-Interacting Dark Matter

A likelihood-based analysis of  $\gamma$ -ray flux from annihilations of self-interacting dark matter

MAGDALENA ERIKSSON, BJÖRN EURENIUS, SUSANNA LARSSON, RIKARD WADMAN

Department of Physics

Chalmers University of Technology

## Abstract

Most of the matter in the Universe is unidentified and invisible, i.e. dark. Detecting dark matter particles from the Cosmos is arguably one of the most pressing research questions in science today. In the standard paradigm of modern cosmology, dark matter is assumed to consist of weakly interacting massive particles, which may annihilate in pairs into gamma photons. Such annihilations give rise to a measurable gamma ray flux, the amplitude of which is proportional to a so-called  $J$ -factor. Current  $J$ -factor calculations usually neglect dark matter self-interactions. However, dark matter self-interactions are compatible with current astrophysical observations, and can potentially solve long-standing problems regarding the formation and evolution of galaxies. The purpose of this thesis is to perform the first self-consistent  $J$ -factor calculation which includes dark matter self-interactions. This calculation is based upon the combined use of non-relativistic quantum mechanics and Newtonian galactic dynamics. The formalism developed in this thesis has been applied to a sample of 20 dwarf spheroidal galaxies, which are known to be dark matter dominated astrophysical objects. For each galaxy in the sample, a likelihood analysis based on actual stellar velocity data has been performed in order to extract the distribution of dark matter in the galaxy, and estimate the induced error on the associated  $J$ -factor. We have found that the  $J$ -factors for self-interacting dark matter can be larger than standard  $J$ -factors by several orders of magnitude. Previous attempts to include dark matter self-interactions in the  $J$ -factor calculation neglect the details of the dark matter distribution in dwarf spheroidal galaxies. We have shown that this approximation leads to relative errors on the  $J$ -factors as large as two orders of magnitude. A paper illustrating these results is currently in preparation and is to be submitted to JCAP (impact factor 5.634).

Keywords: dark matter, self-interaction,  $J$ -factor, dwarf spheroidal galaxies, Sommerfeld enhancement, likelihood.

---

## Sammandrag

Den största andelen materia i universum är oidentifierad och osynlig, d.v.s. mörk. Detektion av mörk materia-partiklar från universum kan i skrivande stund anses vara en av de viktigaste frågorna inom forskarvärlden. I standardparadigmen för modern kosmologi antas det att mörk materia består av svagt interagerande massiva partiklar, som kan annihilera parvis till gammafotoner. Dessa annihilationer ger upphov till ett mätbart fotonflöde, vars amplitud är proportionell mot den så kallade  $J$ -faktorn. Nuvarande beräkningar av  $J$ -faktorer tar generellt inte hänsyn till självinteraktioner. Det har visat sig att självinteragerande mörk materia överensstämmer med astrofysiska observationer och har potential att lösa problem gällande galaxers rörelser och uppkomst. Syftet med denna rapport är att utföra den första konsekventa uträkningen av  $J$ -faktorer som inkluderar självinteragerande mörk materia. Dessa beräkningar är baserade på den kombinerade användningen av icke-relativistisk kvantmekanik och Newtonsk galaxdynamik. Formalismen som utvecklas i denna rapport har tillämpats på 20 sfäriska dvärggalaxer, vilka är kända att vara objekt dominerade av mörk materia. För varje galax i denna undersökning används en likelihoodanalys baserad på stjärnhastighetsdata för att därigenom extrahera distributionen av mörk materia i galaxen. Utifrån detta kan det inducerade felet på den aktuella  $J$ -faktorn uppskattas. Tidigare försök att inkludera självinteragerande mörk materia i beräkningen av  $J$ -faktorer tar inte full hänsyn till detaljerna kring distributionen för mörk materia i sfäriska dvärggalaxer. Vi har visat att denna approximation leder till relativa fel i beräkningarna så stora som två storleksordningar. En forskningsartikel som visar dessa resultat är under konstruktion och ska bli framlagd till JCAP (Impact factor 5.634).

Nyckelord: mörk materia, självinteraktion,  $J$ -faktor, sfäriska dvärggalaxer, Sommerfeldförstärkning, likelihood.



## Acknowledgements

We wish to thank our supervisor Riccardo Catena without whose guidance and patience answering our questions, this project wouldn't have been possible. Furthermore we wish to express gratitude towards Sebastian Bergström, Emelie Olsson, Michael Högberg, and Andreas Unger in the group behind “Dwarf Spheroidal J-factors with Self-interacting Dark Matter” for our close collaboration during the working process. In addition we would like to thank Andrea Chiappo for sharing the galaxy data used in our calculations.

The Authors, Gothenburg, May 2017



## Svensk sammanfattning

I modellerandet av galaxers födelse och evolution uppträder en skiljaktighet mellan mängden materia som är nödvändig för att förklara observationer teoretiskt och mängden materia som optiskt har observerats. För att dessa ska överensstämja har det uppskattats att det behövs ungefär 6 gånger mer massa i universum än vad som har observerats. Den mest accepterade förklaringen till detta är att universum består av, förutom baryonisk materia, en osynlig 'mörk' materia (MM).

Den dominerande modellen för MM grundar sig på att MM består av svagt interagerande massiva partiklar (WIMPs). Interaktionen mellan dessa sker, utöver gravitation, genom svag växelverkan och/eller möjligen en för standardmodellen okänd kraft. Interaktion mellan två MM-partiklar kan resultera i annihilation av partiklarna följt av emission av två gammafotoner. Detta fotonflöde beskrivs traditionellt som

$$\Phi_\gamma = \frac{N_\gamma \overline{\sigma v_{\text{rel}}}}{4\pi m_\chi^2} J$$

där  $N_\gamma$  är antalet fotoner producerade vid varje annihilation,  $\overline{\sigma v_{\text{rel}}}$  är annihileringstvårsnittet multiplicerat med MM-partiklarnas relativa hastighet medelvärdesbildat över hastighetsdistributionen,  $m_\chi$  är MM-partiklarnas massa och

$$J = \int_{\Delta\Omega} d\Omega \int_{\text{l.o.s.}} ds \rho_\chi(s, \Omega)^2$$

är den så kallade  $J$ -faktorn. Här är  $\Omega$  galaxens rymdvinkel sett från jorden, den inre integralen tar längs en siktlinje, *line of sight* (l.o.s.), och  $\rho_\chi$  är masstätheten för MM.

Hastigheten av partiklarna i en dvärggalax antas ofta vara konstant, vilket även gör termen  $\overline{\sigma v_{\text{rel}}}$  konstant. Däremot vore ett mer generellt antagande att hastigheten följer en hastighetsdistribution. Vi har i detta arbete visat att ett sådant antagande har stora konsekvenser för beräkningen av  $J$ -faktorn.

Syftet med detta arbete är att ta fram en motsvarande  $J$ -faktor för självinteragerande MM och bestämma denna för 20 sfäriska dvärggalaxer. Sfäriska dvärggalaxer är optimala objekt för detektion av MM, då de har visat sig bestå nästan uteslutande av MM.

Antydningar till annihilationsprodukter har observerats av bland annat teleskopet AMS-02, vilket har detekterat ett överflöd av positroner, som också är möjliga annihilationsprodukter, med okänt ursprung. Om annihilande MM antas ligga bakom dessa skulle ett interaktionstvårsnitt uppskattningsvis 100 gånger större än vad som är möjligt för växelverkan via svaga krafter vara nödvändigt. Som en lösning på detta föreslogs den kvantmekaniska mekanismen *Sommerfeldförstärkning*. Ett Sommerfeldförstärkt tvårsnitt tar hänsyn till interaktionspotentialen mellan två partiklar. Ett analogt exempel är en asteroid som rör sig i närheten av en stjärna. Den attraktiva gravitationspotentialen förstärker avsevärt sannolikheten för kollision, och därmed effektivt tvårsnittet. Sommerfeldförstärkning betecknad  $S$  beror på de ingående partiklarnas relativa hastigheter, och har visat sig vara större för låga farter.

Om Sommerfeldförstärkningen faktoriseras ut ur tvårsnittet fås att  $\overline{\sigma v_{\text{rel}}} = \overline{S(v_{\text{rel}})\sigma_0 v_{\text{rel}}} = \overline{S(v_{\text{rel}})\sigma_0} v_{\text{rel}}$  där  $\sigma_0$  är det oförstärkta tvårsnittet och till god approximation kan antas bero som  $1/v_{\text{rel}}$ , varför produkten  $\sigma_0 v_{\text{rel}}$  är konstant och kan tas utanför integralen. Den kvarvarande  $S(v_{\text{rel}})$  är dock hastighetsberoende, dvs. beroende på kinematiken hos den studerade dvärggalaxen. För att inkludera allt objektspecifikt beroende kan nu  $J$ -faktorn på ett naturligt sätt omdefinieras till

$$J_S = \int_{\Delta\Omega} d\Omega \int_{\text{l.o.s.}} ds \int d^3\mathbf{v}_{\text{rel}} P_{r,\text{rel}}(\mathbf{v}_{\text{rel}}) S(v_{\text{rel}}) \rho_\chi^2(s, \Omega).$$

där  $\mathbf{v}_{rel}$  är den relativa hastigheten mellan ett par MM-partiklar,  $P_{r,rel}(\mathbf{v}_{rel})$  en sannolikhetsfördelning över den relativa hastigheten, och  $\rho_\chi(s, \Omega)$  densiteten av MM.

För att kunna beräkna den Sommerfeldförstärkta  $J_S$ -faktorn behöver de ingående termerna i uttrycket ovan utvärderas. Inledningsvis betraktas Sommerfeldfaktorn. Genom att anta att annihilationen sker i en punkt, säg origo, så är systemets motsvarande Hamiltonian en deltafunktion med  $H = V_{ann}\delta$ . Det följer då att sannolikheten för annihilation är proportionell mot sannolikheten att MM-partikeln är lokaliserad vid origo  $|\psi_k(0)|^2$ , så att förstärkningsfaktorn kan skrivas som

$$S = \frac{|\psi(0)|^2}{|\psi^{(0)}(0)|^2} = |\psi(0)|^2,$$

där  $\psi_k^{(0)}(0)$  är den normaliserade vågfunktionen med  $V_{ann} = 0$ . Då det har visats troligt att MM-partiklar interagerar genom en Yukawapotential används denna för att bestämma  $S$  med hjälp av Schrödingerekvationen. Yukawapotentialen är definierad som

$$V_Y(r) = \pm \frac{\alpha}{r} e^{-m_\phi r},$$

där  $\alpha$  är kopplingsstyrkan och  $m_\phi$  massan av den kraftbärande partikeln mellan de interagerande MM-partiklarna. Motsvarande radiella Schrödingerekvation kan då skrivas

$$\Phi'' + \frac{2}{x}\Phi' + \left(1 + \frac{2a}{x}e^{-bx}\right)\Phi = 0,$$

där  $x$  är proportionell mot  $r$ ,  $a = \alpha/2v_{rel}$ , och  $b = m_\phi/m_\chi v_{rel}$  där  $v_{rel}$  betecknar partiklarnas relativa hastighet. Med hjälp av Schrödingerekvationen ovan kan förstärkningsfaktorn med lämpliga begynnelsevillkor bestämmas till

$$S = \frac{1}{\lim_{x \rightarrow \infty} \left[ x^2 \Phi(x)^2 + (x - \pi/2)^2 \Phi(x - \pi/2)^2 \right]}.$$

Vi fortsätter utvärderingen av  $J$ -faktorn med en undersökning av den relativa hastighetsdistributionen  $P_{r,rel}(\mathbf{v}_{rel})$ . Då de sfäriska dvärggalaxerna har svaga gravitationsfält kommer MM-partiklarna röra sig med ickerelativistiska hastigheter, vilket gör att de kan beskrivas med en Newtonsk distributionsfunktion (DF)  $f$  i det 6-dimensionella fasrummet. Massdensiteten av MM-partiklarna kan definieras som  $\rho_\chi \equiv \int d^3\mathbf{v} f(\mathbf{r}, \mathbf{v})$ , vilket leder till en normaliserad hastighetsdistribution på formen

$$P_{\mathbf{r}}(\mathbf{v}) = \frac{f(\mathbf{r}, \mathbf{v})}{\rho_\chi(\mathbf{r})}.$$

Med ett koordinatsystem centrerat i masscentrum kan uttrycket förenklas och den eftersökta relativa hastighetsdistributionen erhålls genom integration över hastigheten  $\mathbf{v}_{cm}$  enligt

$$P_{r,rel}(\mathbf{v}_{rel}) = \int P_{r,pair}(\mathbf{v}_{cm}, \mathbf{v}_{rel}) d^3\mathbf{v}_{cm}.$$

Det är därmed möjligt att beräkna  $P_{r,rel}(\mathbf{v}_{rel})$  om DF kan bestämmas. Detta förenklas genom att anta sfärisk symmetri, vilket är en god approximation för de aktuella galaxerna. Sfärisk symmetri ger nämligen att DF kan skrivas om som en funktion av systemets Hamiltonian enligt

$$f(r, v) = f(-\Phi(r) - v^2/2).$$

där  $\Phi(r)$  är systemets gravitationspotential och  $v$  en MM-partikels hastighet i systemet. Användning av Eddingtons formel leder vidare till ett allmänt uttryck för DF som funktion av

$\Phi(r)$  och massdensitetsdistributionen  $\rho(r)$ . Detta uttryck kan sedan användas för att härleda ett uttryck för den relativa hastighetsdistributionen,

$$P_{r,\text{rel}}(v_{\text{rel}}) = \frac{16\pi^2 v_{\text{rel}}^2}{\rho_\chi^2(r)} \int_0^\infty dv_{\text{cm}} v_{\text{cm}}^2 \int_0^1 dz f\left(r, v_{\text{cm}}^2 + \frac{v_{\text{rel}}^2}{4} - v_{\text{cm}} v_{\text{rel}} z\right) \times f\left(r, v_{\text{cm}}^2 + \frac{v_{\text{rel}}^2}{4} + v_{\text{cm}} v_{\text{rel}} z\right).$$

För att kunna räkna ut  $J$ -faktorn saknas nu bara densitetsprofilen  $\rho_\chi(r)$ . En vanlig grupp av densitetsprofiler ges av den så kallade *generaliserade Hernquistprofilen*

$$\rho(r) = \rho_0 (r/r_0)^{-\gamma} (1 + (r/r_0)^\alpha)^{(\gamma-\beta)/\alpha},$$

där  $r$  är avståndet från galaxens centrum och  $\rho_0$ ,  $r_0$  är galaxspecifika parametrar som beskriver kurvans form. För MM används vanligen  $(\alpha, \beta, \gamma) = (1, 3, 1)$ , vilken även går under namnet *Navarro Frenk & White* (NFW) efter de som först föreslog den. Den är divergent i  $r = 0$ , vilket innebär att en stor del av massan är koncentrerad nära galaxens centrum. Observationer tyder dock på att sfäriska dvärggalaxer har en betydligt flackare massdistribution nära sina mittpunkter, varför vi väljer att även använda den planare profilen  $(\alpha, \beta, \gamma) = (1, 3, 0)$ , även kallad *cored Zhao*. För den statistiska metoden kommer även densiteten av stjärnor behövas. Den kan i en sfärisk dvärggalax modelleras med den generaliserade Hernquistprofilen och  $(\alpha, \beta, \gamma) = (2, 5, 0)$ , även kallad *Plummers profil*.

Då alla mätningar av praktiska skäl måste ske från vår observationspunkt jorden blir det problematiskt att mäta långa avstånd. Däremot kan vinklar mätas med hög noggrannhet, vilket kan användas för att få en rimlig uppskattning av avståndet, vinkelrätt mot vår siktlinje, mellan stjärnor inom en galax. Avståndet  $R$  från centrum av galaxen till siktlinjen samt hastigheten längs siktlinjen  $v_{\text{l.o.s.}}$  för enskilda stjärnor har uppmätts för flera sfäriska dvärggalaxer, vilka beräkningarna ska utföras på. Det är önskvärt att relatera dessa observabler med densitetsfördelningen av MM för att skapa en statistisk passform över densitetsparametrarna och utifrån detta beräkna  $J$ -faktorn.

Det är dock inte möjligt att förutsäga enskilda stjärnors rörelse relativt galaxens masscentrums rörelse på grund av antagandet om hastighetsisotropi. Däremot kan variansen  $\sigma_{\text{l.o.s.}}^2$  av medelhastigheten längs siktlinjen baserat på densitetsfördelningen och luminositetsfördelningen förutsägas som

$$\sigma_{\text{l.o.s.}}^2(R) = \frac{2}{I(R)} \int_R^\infty dr \frac{r}{\sqrt{r^2 - R^2}} \int_r^\infty ds \frac{\nu(s)GM(s)}{s^2},$$

där  $G$  är gravitationskonstanten,  $\nu(r)$  är luminositetsdensiteten,  $I(R) = \int_{\text{l.o.s.}} \nu(s) ds$  är ljusintensiteten och  $M$  massan innanför en given radie. Denna ekvation kan beräknas med ett givet val av densitetsprofilerna  $\rho_\chi(r)$  och  $\nu(r)$ .

För att bestämma parametrarna används en likelihoodanpassning och de numeriska värden som korresponderar bäst mellan teori och observerade resultat erhålls. Detta val av parametrar är dock svårhanterliga för en likelihoodanpassning, vilket löses genom att det är möjligt att substituera  $\rho_0 \rightarrow v_0 = r_0 \sqrt{G\rho_0}$  och likelihoodanpassningen görs därmed i termer av  $r_0$ ,  $v_0$  och  $r_*$ . Utgående från denna anpassning erhålls konfidensregioner för parametrarna  $v_0$ ,  $r_0$  för varje sfärisk dvärggalax, som sedan kan omvandlas till en grupperad likelihoodfunktion för  $J$ -faktorn genom att räkna ut denna för varje punkt i  $r_0$ ,  $v_0$ -regionerna, dela in de resulterande värdena i intervall och för varje delintervall välja den punkt har störst likelihood. Utifrån detta kan konfidensintervall för  $J$ -faktorerna beräknas.

I beräkningarna av den slutgiltiga  $\mathcal{J}$  faktorerna används Arkani-Hamedparametrarna  $\alpha = 0.01$  och  $m_\phi = 1 \text{ GeV}/c^2$  med  $m_\chi = 650 \text{ GeV}/c^2$ . Där notationen  $\mathcal{J} = \log_{10}(J)$  används med

$J$  i enheten  $\text{GeV}^2\text{cm}^{-5}$ . De beräknade  $\mathcal{J}$ ,  $\mathcal{J}_S$  och  $\mathcal{J}_{S(v^*)}$  faktorerna för både NFW- och cored Zhao-profilerna kan ses i tabell i. Som ses i tabellen är  $\mathcal{J}_S$  ofta upp till fyra gånger större än  $J$ , medan  $\mathcal{J}_{S(v^*)}$  ger en överskattning av  $J_S$  en till två storleksordningar för de flesta galaxer.

Sammanfattningsvis har vi i denna rapport konstruerat en modell för och extraherat Sommerfeldförstärkta  $J$ -faktorer för 20 sfäriska dvärggalaxer. Detta gjordes utifrån Newtonsk galaxdynamik, icke-relativistisk kvantmekanik samt en likelihoodbaserad analysmetod.

**Table i:** Beräknade  $\mathcal{J}$ -,  $\mathcal{J}_S$ - och  $\mathcal{J}_{S(v^*)}$ -faktorer för varje studerad dSph för både NFW- och cored Zhao-profilerna. Beräkningarna av de Sommerfeldförstärkta  $J$ -faktorerna använder sig av Arkani-Hamed parametrarna  $\alpha = 0.01$  och  $m_\phi = 1 \text{ GeV}/c^2$  med  $m_\chi = 650 \text{ GeV}/c^2$ . En typisk relativ hastighet av  $v^* = 10^{-5}c$  används för  $\mathcal{J}_{S(v^*)}$ -faktorberäkningarna.  $N$  är antalet stjärnor i datamängden. Det kan noteras att osäkerheten i den beräknade faktorerna tenderar att minska för ökande  $N$  vilket förväntas av en statistisk metod. Det finns också en tydlig skillnad i storleksordning mellan olika familjer av  $J$ -faktorer för både NFW- och cored Zhao-profilerna. Speciellt är  $\mathcal{J}_S$  ofta fyra storleksordningar större än den ursprungliga  $J$ , medan  $\mathcal{J}_{S(v^*)}$  ger en överskattning av den mer riktiga  $J_S$  av en till två storleksordning för de flesta galaxer. I tabellen är  $\mathcal{J}_S$  och  $\mathcal{J}_{S(v^*)}$  i enheter av  $\log_{10} \text{GeV}^2\text{cm}^{-5}$ .

Dwarf	$N$	NFW			Cored Zhao		
		$\mathcal{J}$	$\mathcal{J}_{S(v^*)}$	$\mathcal{J}_S$	$\mathcal{J}$	$\mathcal{J}_{S(v^*)}$	$\mathcal{J}_S$
Bootes I	14	$17.92^{+0.62}_{-0.75}$	22.65	$21.79^{+0.49}_{-0.36}$	$19.34^{+0.44}_{-2.07}$	24.07	$21.86^{+0.42}_{-0.48}$
Leo IV	17	$16.90^{+0.89}_{-0.94}$	21.63	$21.31^{+0.65}_{-0.85}$	$16.58^{+1.64}_{-0.73}$	21.31	$20.87^{+0.55}_{-0.56}$
Leo T	19	$17.44^{+0.49}_{-0.90}$	22.17	$21.37^{+0.34}_{-0.85}$	$17.45^{+0.48}_{-0.96}$	22.18	$21.27^{+0.29}_{-0.82}$
Bootes II	20	$18.81^{+1.39}_{-1.03}$	23.54	$23.05^{+1.16}_{-1.07}$	$18.82^{+1.44}_{-1.10}$	23.55	$23.01^{+0.90}_{-0.89}$
Ursa Major II	20	$19.84^{+0.33}_{-0.35}$	24.57	$23.22^{+0.61}_{-0.31}$	$20.29^{+0.52}_{-0.81}$	25.02	$23.10^{+0.47}_{-0.47}$
Canes Venatici II	25	$18.47^{+0.34}_{-0.68}$	23.20	$21.74^{+0.28}_{-0.30}$	$18.53^{+0.38}_{-0.79}$	23.26	$21.73^{+0.38}_{-0.42}$
Hercules	30	$18.12^{+0.28}_{-0.35}$	22.85	$22.16^{+0.30}_{-0.32}$	$18.00^{+0.34}_{-0.29}$	22.73	$21.94^{+0.27}_{-0.24}$
Ursa Major I	39	$18.24^{+0.97}_{-0.67}$	22.97	$22.40^{+0.63}_{-0.84}$	$17.84^{+0.75}_{-0.35}$	22.57	$21.88^{+0.47}_{-0.41}$
Willman 1	45	$19.64^{+0.45}_{-0.58}$	24.37	$22.95^{+0.60}_{-0.22}$	$19.40^{+1.23}_{-0.45}$	24.13	$23.14^{+0.34}_{-0.16}$
Coma Berenices	59	$19.39^{+0.36}_{-0.45}$	24.12	$22.89^{+0.27}_{-0.35}$	$19.89^{+0.82}_{-0.87}$	24.62	$23.00^{+0.17}_{-0.30}$
Segue 1	66	$19.26^{+0.57}_{-0.46}$	23.99	$23.58^{+0.40}_{-0.46}$	$19.10^{+0.47}_{-0.30}$	23.83	$23.22^{+0.29}_{-0.20}$
Ursa Minor	196	$19.62^{+0.04}_{-0.25}$	24.35	$23.41^{+0.00}_{-0.31}$	$19.47^{+0.22}_{-1.07}$	24.20	$23.14^{+0.19}_{-1.48}$
Canes Venatici I	214	$18.01^{+0.25}_{-0.29}$	22.74	$21.86^{+0.29}_{-0.33}$	$17.87^{+0.22}_{-0.99}$	22.60	$21.61^{+0.19}_{-1.09}$
Leo I	328	$17.66^{+0.27}_{-0.13}$	22.39	$21.11^{+0.45}_{-0.17}$	$17.53^{+0.22}_{-0.10}$	22.26	$21.06^{+0.29}_{-0.04}$
Draco	353	$18.74^{+0.26}_{-0.28}$	23.47	$22.10^{+0.51}_{-0.19}$	$18.58^{+0.24}_{-0.15}$	23.31	$21.92^{+0.38}_{-0.12}$
Sextans	424	$18.74^{+0.20}_{-0.20}$	23.47	$22.64^{+0.20}_{-0.20}$	$18.52^{+0.20}_{-0.30}$	23.24	$22.31^{+0.19}_{-0.30}$
Carina	758	$17.68^{+0.87}_{-0.06}$	22.41	$21.46^{+1.03}_{-0.08}$	$17.68^{+0.44}_{-0.07}$	22.41	$21.47^{+0.49}_{-0.05}$
Sculptor	1352	$18.91^{+0.12}_{-0.13}$	23.64	$22.63^{+0.12}_{-0.15}$	$18.68^{+0.15}_{-0.21}$	23.41	$22.28^{+0.16}_{-0.24}$
Sagittarius	1373	$20.22^{+0.14}_{-0.12}$	24.95	$23.68^{+0.11}_{-0.08}$	$19.78^{+0.16}_{-0.17}$	24.51	$23.04^{+0.16}_{-0.17}$
Fornax	2409	$18.96^{+0.10}_{-0.14}$	23.69	$22.59^{+0.09}_{-0.13}$	$18.69^{+0.14}_{-0.22}$	23.42	$22.19^{+0.12}_{-0.19}$

# Contents

List of Figures	xvii
List of Tables	xxi
<b>1 Introduction</b>	<b>1</b>
<b>2 Dark matter evidence and the physical impact of self-interactions</b>	<b>3</b>
2.1 Weakly interacting massive particles . . . . .	5
2.2 Self-interacting dark matter . . . . .	6
2.2.1 The physical impact of self-interaction . . . . .	7
2.2.2 Possible interactions . . . . .	7
<b>3 Photon flux from annihilating dark matter</b>	<b>10</b>
<b>4 Annihilation cross section</b>	<b>13</b>
4.1 Brief introduction to non-relativistic scattering theory . . . . .	14
4.2 General Sommerfeld enhancement factor . . . . .	17
4.3 Case of attractive Yukawa potential . . . . .	19
<b>5 Velocity distribution</b>	<b>21</b>
5.1 Eddington's formula . . . . .	22
5.2 Relative velocity distribution of an isotropic system . . . . .	23
<b>6 Density profiles</b>	<b>25</b>
6.1 Gravitational potential in a spherical system . . . . .	26
6.2 Dark matter gravitational potential of a dwarf spheroidal galaxy . . . . .	27
<b>7 Statistical methods</b>	<b>28</b>
7.1 Astronomical observations . . . . .	28
7.2 Line of sight velocity dispersion . . . . .	28
7.3 Maximum likelihood estimation of parameters . . . . .	31
<b>8 Validation of numerical implementation</b>	<b>33</b>
8.1 Sommerfeld enhancement . . . . .	33
8.2 Relative velocity distribution . . . . .	35
8.3 Maximisation of likelihood function and calculation of J-factors . . . . .	36
<b>9 Numerical results</b>	<b>38</b>
<b>10 Conclusion</b>	<b>42</b>
<b>Bibliography</b>	<b>43</b>
<b>Appendix A The unenhanced cross section</b>	<b>II</b>
<b>Appendix B Dimensionless relative velocity distribution</b>	<b>IV</b>

<b>Appendix C The Jeans equations</b>	<b>VI</b>
<b>Appendix D Additional Results</b>	<b>XI</b>
D.1 Parameter regions . . . . .	XI
D.2 Binned Likelihood Functions . . . . .	XI
<b>Appendix E Mathematica code</b>	<b>XXII</b>
E.1 Eddington Formula . . . . .	XXIII
E.2 Relative Velocity Distribution . . . . .	XXV
E.3 Sommerfeld Enhancement factor . . . . .	XXVII
E.4 Line of Sight Velocity Dispersion . . . . .	XXVIII
E.5 Integral over relative velocity . . . . .	XXIX
E.6 J-factors . . . . .	XXXI
E.7 Log Likelihood function . . . . .	XXXIV
E.8 Maximum Likelihood Estimate . . . . .	XXXVI
E.9 Tabulation of Likelihood and J-factors . . . . .	XXXVI
E.10 Construction of confidence levels . . . . .	XXXVII



# List of Figures

2.1	Rotation curve of the galaxy NGC 6503 (solid line), and the contributions from the galaxy's different mass components; gas (dotted) and disk (dashed). The rotation curve cannot consist of only the gas and disk components. The dotted-dashed line is theoretical, but is estimated to be the missing mass contribution to explain the shape of the rotation curve. This is the thought contribution of a DM halo. Graph from [14]. . . . .	4
2.2	Two different interactions between DM particles. Fig. 2.2a illustrates self-interaction through the force carrier $\phi$ . In fig. 2.2b a DM particle- anti-particle pair is annihilated through some unknown process into two gamma photons. . . . .	8
3.1	An observer located at $A$ studies some properties of the galaxy at the galactic radius $r$ . The point being studied lies at a distance $s$ and the centre of galaxy at a distance $D$ from $A$ . The angle $\beta$ represents the angle of cone tangent the locus of points a distance from the centre of the galaxy. . . . .	12
7.1	An observer located at $A$ studies some properties of the galaxy at the galactic radius $r$ . The observables are along the line of sight distance $R$ from the centre. $v_\theta$ and $v_r$ are the velocity components at radius $r$ of the galaxy. In the figure only the positive $z$ is shown. . . . .	29
8.1	Numerical computation of the wave function for the Yukawa potential using the Arkani-Hamed parameters $\alpha = 0.01$ , $m_\phi = 1 \text{ GeV}/c^2$ , with a DM particle mass of $m_\chi = 650 \text{ GeV}/c^2$ and a relative velocity of $v_{\text{rel}} = 10^{-4}c$ . The left graph shows the radial wave function while the right one the $C^2$ value. It can be seen that $C^2$ is about constant with a value of $C^2 = 0.96083 \pm 0.00004$ in the entire range. . .	33
8.2	Sommerfeld enhancement factor varied over DM particle masses $m_\chi$ and their relative velocities $v_{\text{rel}}$ with Arkani-Hamed parameters $\alpha = 0.01$ , $m_\phi = 1 \text{ GeV}/c^2$ . In (a) the enhancement factor for $m_\chi = 650 \text{ GeV}/c^2$ is close to a resonance peak and hence is significantly higher than the other three displayed masses at low relative velocities. In (b) it is clear that the enhancement factor gets larger with lower relative velocities of the DM particles. . . . .	34
8.3	Sommerfeld enhancement factor varied over DM particle masses $m_\chi$ and their relative velocities $v_{\text{rel}}$ with Lattanzi-Silk parameters $\alpha = 0.03$ , $m_\phi = 90 \text{ GeV}/c^2$ . In (a) the enhancement factor is shown to have clear resonance behaviour depending on DM mass $m_\chi$ . In (b) it is clear that the enhancement factor gets larger with lower relative velocities of the DM particles, although with a different dependence than with Arkani-Hamed parameters. Note that $S$ with $m_\chi = 4.5 \text{ TeV}/c^2$ is large because of a resonance peak at that mass. . . . .	34

8.4	Shown in the (a) is a numerical calculation of the dimensionless phase-space density $\tilde{f}(\tilde{\mathcal{E}})$ from the dimensionless Eddington formula, assuming a cuspy NFW (solid line) and a cored Zhao (1, 3, 0) density profile (dashed line) respectively. Note the divergence for both profiles at the maximum value, corresponding to $\tilde{\mathcal{E}} = \tilde{\Psi}(0)$ . The relative velocity distribution $P_{\text{rel}}(v_{\text{rel}})$ is shown in (b) and (c) at different radii for a generic dSph with an NFW and a cored Zhao DM density profile respectively, with parameters $\rho_0 = 1.3 \times 10^8 \text{ M}_{\odot} \text{ kpc}^{-3}$ and $r_0 = 0.62$ . . . .	36
8.5	The likelihood function for different dSphs using the NFW DM density profile and a Plummer profile for the surface brightness. The minimum is marked by a dot and the coloured regions corresponds to deviations $1\sigma$ , $2\sigma$ and $3\sigma$ respectively. The dashed lines corresponds to constant J factors. . . . .	37
9.1	$\mathcal{J}_S$ -factors for the Sculptor galaxy over a range of $\epsilon_{\phi}$ from $10^{-3}$ to 100. The $\mathcal{J}_S$ factors are compared against $\mathcal{J}_{S(v^*)} = \log_{10}(S(v^*)J)$ for the typical relative velocity of $v^* = 10^{-5}c$ . Fig. (a) uses the NFW density profile while fig. (b) uses the cored Zhao profile. A clear difference between the calculated $\mathcal{J}_S$ value and that of $\mathcal{J}_{S(v^*)}$ , for both the NFW and cored Zhao density profiles, is the amplitude of the oscillations are greater for $\mathcal{J}_S$ . Meanwhile the main difference between the NFW and the cored Zhao profile are in a constant vertical shift while the overall shape and the behaviour of the oscillations remain largely the same. The calculations uses $\alpha = 0.01$ and $m_{\phi} = 1 \text{ GeV}/c^2$ as in the Arkani-Hamed et al. parameter profile [55]. . . . .	40
9.2	All figures show calculated likelihood functions for the Sculptor dSph. In the left column a cuspy NFW DM distribution have been used to model the dSph, while in the right column a cored Zhao profile have been used. Shown in (a) and (b) is the likelihood function in the $r_0, v_0$ parameter space, with the MLE marked with a plus sign. The coloured regions correspond to evaluated $1\sigma$ , $2\sigma$ and $3\sigma$ confidence levels respectively and the dotted lines correspond to contours of constant $\mathcal{J}_S$ . The binned likelihood $-\log(L/L_{\text{MLE}})$ with corresponding standard deviations is plotted in (c) and (d) for $\mathcal{J}$ and in (e) and (f) for $\mathcal{J}_S$ . . . . .	41
D.1	Evaluated likelihood function and $\mathcal{J}_S$ for Bootes I and II, Carina and Coma Berenices, modelled with NFW and cored Zhao DM profiles respectively. The coloured regions correspond to $1\sigma$ , $2\sigma$ , $3\sigma$ confidence levels and the dotted lines are contour lines for $\mathcal{J}_S$ . . . . .	XII
D.2	Evaluated likelihood function and $\mathcal{J}_S$ for Canes Venatici I and II, Draco and Fornax, modelled with NFW and cored Zhao DM profiles respectively. The coloured regions correspond to $1\sigma$ , $2\sigma$ , $3\sigma$ confidence levels and the dotted lines are contour lines for $\mathcal{J}_S$ . . . . .	XIII
D.3	Evaluated likelihood function and $\mathcal{J}_S$ for Hercules, Leo I, Leo IV and Leo T, modelled with NFW and cored Zhao DM profiles respectively. The coloured regions correspond to $1\sigma$ , $2\sigma$ , $3\sigma$ confidence levels and the dotted lines are contour lines for $\mathcal{J}_S$ . . . . .	XIV
D.4	Evaluated likelihood function and $\mathcal{J}_S$ for Sculptor, Segue 1, Sextans and Sagittarius, modelled with NFW and cored Zhao DM profiles respectively. The coloured regions correspond to $1\sigma$ , $2\sigma$ , $3\sigma$ confidence levels and the dotted lines are contour lines for $\mathcal{J}_S$ . . . . .	XV

---

D.5	Evaluated likelihood function and $\mathcal{J}_S$ for Ursa Major I and II, Ursa Minor and Willman 1, modelled with NFW and cored Zhao DM profiles respectively. The coloured regions correspond to $1\sigma$ , $2\sigma$ , $3\sigma$ confidence levels and the dotted lines are contour lines for $\mathcal{J}_S$ . . . . .	XVI
D.6	Binned likelihood as a function of $\mathcal{J}_S$ for Bootes I and II, Carina and Coma Berenices, modelled with NFW and cored Zhao DM profiles respectively. The grey triangle marks the MLE and the horizontal lines correspond to $1\sigma$ , $2\sigma$ , $3\sigma$ confidence levels. . . . .	XVII
D.7	Binned likelihood as a function of $\mathcal{J}_S$ for Canes Venatici I and II, Draco and Fornax, modelled with NFW and cored Zhao DM profiles respectively. The grey triangle marks the MLE and the horizontal lines correspond to $1\sigma$ , $2\sigma$ , $3\sigma$ confidence levels. . . . .	XVIII
D.8	Binned likelihood as a function of $\mathcal{J}_S$ for Hercules, Leo I, Leo IV and Leo T, modelled with NFW and cored Zhao DM profiles respectively. The grey triangle marks the MLE and the horizontal lines correspond to $1\sigma$ , $2\sigma$ , $3\sigma$ confidence levels. . . . .	XIX
D.9	Binned likelihood as a function of $\mathcal{J}_S$ for Sculptor, Segue 1, Sextans and Sagittarius, modelled with NFW and cored Zhao DM profiles respectively. The grey triangle marks the MLE and the horizontal lines correspond to $1\sigma$ , $2\sigma$ , $3\sigma$ confidence levels. . . . .	XX
D.10	Binned likelihood as a function of $\mathcal{J}_S$ for Ursa Major I and II, Ursa Minor and Willman 1, modelled with NFW and cored Zhao DM profiles respectively. The grey triangle marks the MLE and the horizontal lines correspond to $1\sigma$ , $2\sigma$ , $3\sigma$ confidence levels. . . . .	XXI



# List of Tables

- i    Beräknade  $\mathcal{J}$ -,  $\mathcal{J}_S$ - och  $\mathcal{J}_{S(v^*)}$ -faktorer för varje studerad dSph för både NFW- och cored Zhao-profilerna. Beräkningarna av de Sommerfeldförstärkta  $J$ -faktorerna använder sig av Arkani-Hamed parametrarna  $\alpha = 0.01$  och  $m_\phi = 1 \text{ GeV}/c^2$  med  $m_\chi = 650 \text{ GeV}/c^2$ . En typisk relativ hastighet av  $v^* = 10^{-5}c$  används för  $\mathcal{J}_{S(v^*)}$ -faktorberäkningarna.  $N$  är antalet stjärnor i datamängden. Det kan noteras att osäkerheten i den beräknade faktorerna tenderar att minska för ökande  $N$  vilket förväntas av en statistisk metod. Det finns också en tydlig skillnad i storleksordning mellan olika familjer av  $J$ -faktorer för både NFW- och cored Zhao-profilerna. Speciellt är  $J_S$  ofta fyra storleksordningar större än den ursprungliga  $J$ , medan  $J_{S(v^*)}$  ger en överskattning av den mer riktiga  $J_S$  av en till två storleksordning för de flesta galaxer. I tabellen är  $\mathcal{J}_S$  och  $\mathcal{J}_{S(v^*)}$  i enheter av  $\log_{10} \text{ GeV}^2 \text{ cm}^{-5}$ . . .    xiii
- 8.1   Shown are central masses  $\mathcal{M} = \log_{10} M_{300}$  in  $\log_{10} M_\odot$  and J-factors  $\mathcal{J} = \log_{10} J$  without Sommerfeld enhancement in  $\log_{10}(\text{GeV}^2 \text{ cm}^{-5})$  for 20 dSphs. The central masses in column one are obtained from previous studies [6–8] of dSph kinematics while the second column contain J-factors with  $1\sigma$  error levels as calculated by [59] using an NFW profile. The middle two columns contain  $\mathcal{M}$  as calculated from the MLE obtained in this study using an NFW profile and the connected J-factor with  $1\sigma$  error levels. The last two columns show the same for a cored Zhao profile. Note that the MLE central masses all come within the expected range. Notable is also that 15 of the NFW MLE J-factors of this study have  $1\sigma$  confidence regions that overlap the  $1\sigma$  region given by [59]. Five of them have not, but only Fornax and Sextans differ by an order of magnitude or more. . . .    37
- 9.1   Computed  $\mathcal{J}$ ,  $\mathcal{J}_S$ , and  $\mathcal{J}_{S(v^*)}$  factors for each of the considered dSph for both the NFW and the cored Zhao profiles. The calculations of the Sommerfeld enhanced  $J$ -factors make use of the Arkani-Hamed parameters  $\alpha = 0.01$  and  $m_\phi = 1 \text{ GeV}/c^2$  with  $m_\chi = 650 \text{ GeV}/c^2$ . A typical relative velocity of  $v^* = 10^{-5}c$  is used for the  $\mathcal{J}_{S(v^*)}$  factor calculations.  $N$  is the number of stars in the data set. As seen the uncertainty the computed factors tend to decrease with increasing  $N$  as is expected with a statistical method. There is also a clear difference in magnitude between the different flavours of  $J$ -faktorer för både NFW och cored Zhao profile. Specificly,  $J_S$  is often four orders of magnitude larger than the original  $J$ , while  $J_{S(v^*)}$  seem to give an overestimation compared to  $J_S$  of one to two orders of magnitude for most galaxies. As shown here,  $\mathcal{J}_S$  and  $\mathcal{J}_{S(v^*)}$  are in units of  $\log_{10} \text{ GeV}^2 \text{ cm}^{-5}$ . . . . .    39



# Chapter 1

## Introduction

When describing the formation and evolution of galaxies, a discrepancy arises between the amount of matter that is needed to explain observations theoretically and the amount of matter that is actually observed. A notable example is the rotational velocities of outer stars in spiral galaxies which are, by current understanding, far too large for the stars to be kept in orbit by only the visible matter of the galaxy [2]. Current estimates suggest that there would need to be as much as about six times more mass in the universe than can be observed, in order for current theories to be consistent with observations [3]. To account for this, several explanations have been proposed, the most widely accepted being the the existence of some invisible “dark” matter making up the bulk of the mass in the universe [2].

The nature of dark matter (DM) is still largely unknown. The only known macroscopic property of DM is that it does not interact through the electromagnetic force [3], unlike baryonic matter. At the time of writing the most accepted hypothesis is that DM is made up of weakly interacting massive particles (WIMPs) [4], although several other models are still considered likely. Apart from gravity, WIMPs only interact through the weak force, and/or possibly through a new force not described in the standard model (SM).

This thesis focuses on DM self-interactions and on their impact on DM astrophysics, an area that have recently attracted a great deal of attention especially in the context of galaxy formation and evolution. The theory in this thesis will be used to study DM annihilation in a sample of 20 dwarf spheroidal galaxies (dSphs). Self-interactions allow DM particles to transfer energy across a galaxy, which have several interesting physical consequences that may resolve conflicts between theoretical predictions and observations. A special kind of self-interaction is the annihilation of two DM particles, which may lead to the production of gamma rays in the order of a few GeV. The Fermi Large Area Telescope (LAT) and ground based imaging air Cherenkov telescopes [5] are currently searching for signals of DM annihilations in a variety of astrophysical targets.

The photon flux originated from WIMP annihilation can be described analytically, and depends on the so-called *J-factor*

$$J = \int_{\Delta\Omega} \int_{\text{l.o.s.}} ds d\Omega \rho_\chi^2(s, \Omega), \quad (1.1)$$

where l.o.s. indicates integration along the line of sight and  $\rho_\chi(s, \Omega)$  is the DM density at line of sight distance  $s$  and solid angle  $\Omega$  as seen from the Earth. The purpose of this thesis is to modify eq. (1.1) to the case of self-interacting DM, and perform an ab initio calculation of the modified J-factor based upon non-relativistic quantum mechanics and Newtonian galactic dynamics. Dwarf galaxies are known to be optimal targets for detecting gamma rays from DM annihilations, since they are DM dominated and their mass-to-light ratio is generally much larger than those of bright galaxies.

For each galaxy in the sample, calculations will be performed for a representative set of particle physics parameters for the interaction, for two different DM density profiles and one luminosity density profile. The dSphs will be assumed to be spherically symmetric and to have isotropic velocity distributions. The optimum values of the J-factors will be extracted using a likelihood estimation based on star velocity data calculated in [6–8] from measured Doppler shift.

The structure of the report is as follows. We present a summary of DM evidences together with an overview of WIMPs and their annihilation process in chapter 2. Chapter 3 aims to give a qualitative understanding of the  $J$ -factor; where it arises and a concise expression for it. The following chapters 4 to 6 describe each of the included terms in the  $J$ -factor expression. Chapter 4 describes the impact of a self-interaction potential on the annihilation cross section. In chapter 5 DM velocity distribution in galaxies is explained. Lastly, the density distribution of DM in a dSph is evaluated in chapter 6. In chapter 7 the theoretical tools necessary for a likelihood estimation and numerical calculation is introduced. In chapter 8 the constituent parts of the numerical calculations are cross-checked against earlier results, after which the calculated  $J$ -factors are presented in chapter 9. The final chapter 10 contains a discussion that concludes our work and results.

## Chapter 2

# Dark matter evidence and the physical impact of self-interactions

Many reports [9–12] have reviewed the large amount of evidence for DM, whose existence today is considered well-established. Without any attempt to make a full review, in this chapter we present some of the main reasons to consider DM as a real entity for the sake of completeness.

The perhaps most well-known motivation for DM comes from galactic *rotation curves*. That is, a graph of circular velocities of stars and gas as a function of their distance to the corresponding galactic centre. Common for all observed rotation curves is that they exhibit a characteristic flat behaviour at large distances [13], i.e. the velocity of the outer regions of the galaxy is close to constant. This is illustrated in fig. 2.1, where the rotation curve of the galaxy NGC 6503 is plotted together with its mass constituents. The shape of the observed rotation curves from other galaxies are mostly very similar to the one of NGC 6503 in fig. 2.1. Apart from the visible gas and disk matter contributors, there is a theoretical DM halo which is needed to add up to the appearance of the rotation curve. The circular velocity of matter around galactic cores, in Newtonian dynamics, is expected to be

$$v_c(r) = \sqrt{\frac{GM(r)}{r}}, \quad (2.1)$$

where  $G$  is the gravitational constant,  $M(r) = 4\pi \int \rho(r)r^2 dr$  is the mass of the system and  $\rho(r)$  the mass density profile. According to this formula, the circular velocity should be decreasing as  $1/\sqrt{r}$  as the distance from the optical disk increases. The fact that the observed circular velocity becomes approximately constant with increasing distance implies the existence of a halo with mass  $M(r) \propto r$  and  $\rho \propto 1/r^2$  [10], thus resembling an isothermal sphere.

Low Surface Brightness (LSB) galaxies also exhibit flat rotation curves but have, as their name suggest, small stellar populations and thus very limited amounts of visible matter. Taken together, the flat rotation curves and small amount of visible matter implies that the LSBs have a DM halo larger than the one of brighter galaxies, thus making them interesting targets to DM searches.

Another important piece of evidence is *gravitational lensing*. General relativity predicts that mass bends, or lenses, light. The effect can be used to gravitationally ascertain the existence of mass even if an object emits no light. Gravitational lensing is most easily observed in the strong lensing regime, that is, when space-time is so warped that light can travel along multiple paths around the lens, and still be deflected back towards the observer. If a bright source is placed directly behind a circular lens, its light can travel around any side of it, and will appear as a so-called Einstein ring. The radius of the Einstein ring  $r$  is related to the mass  $M$  of the gravitational lens through  $r \propto \sqrt{M}$  [15]. If the bright source behind the lens is slightly offset, or if the lens has a more complex shape, the light from the source can still appear in multiple locations, viewed from slightly different angles. The DM evidence lies in the proportionality between the Einstein radius, or its equivalent, and the mass of the lens. The radii are always found *much* larger than the visible matter could account for, which implies the existence of some "dark" matter.

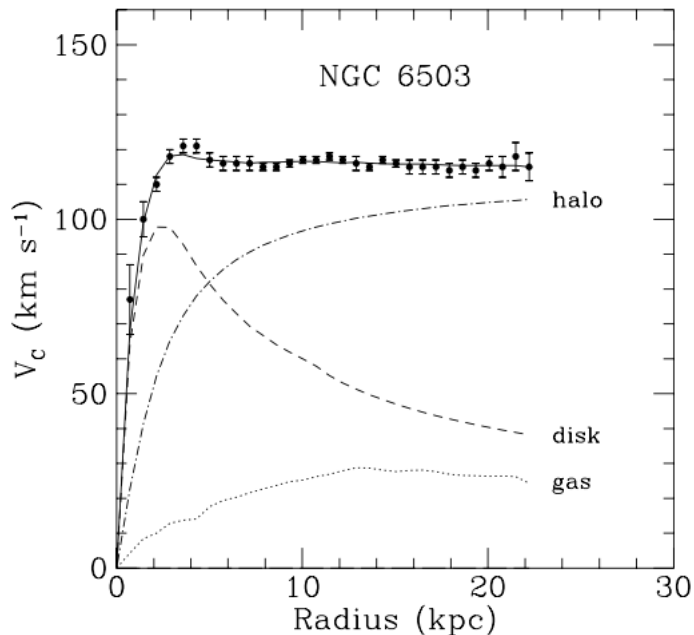


**Figure 2.1:** Rotation curve of the galaxy NGC 6503 (solid line), and the contributions from the galaxy’s different mass components; gas (dotted) and disk (dashed). The rotation curve cannot consist of only the gas and disk components. The dotted-dashed line is theoretical, but is estimated to be the missing mass contribution to explain the shape of the rotation curve. This is the thought contribution of a DM halo. Graph from [14].

Evidence for DM has also been gathered through the observations of stars in galaxies and galaxies in galaxy clusters. For example, measurements of the *line of sight* (l.o.s.) *velocity dispersion* of stars and galaxies have been found to be much larger than expected. Since the velocity of an astronomical object can be determined using red- and blue shifts, the velocity dispersion makes for a natural observable. The l.o.s. velocity dispersion is related to the mass of the corresponding object, and similar to the case of gravitational lensing, the measured values of the l.o.s. velocity dispersion have been significantly higher than what the corresponding visible mass of the object could account for [16]. L.o.s. velocity dispersion is discussed more thoroughly in chapter 7.

Measurements of the Cosmic Microwave Background (CMB) implies that the preponderance of the mass in the universe consists of an unknown DM component. The CMB is the remnant radiation from the hot early days of the universe, when photons first decoupled from matter very shortly after the Big Bang. Anisotropies in the CMB carry information about the total energy content in the universe. The constituents of the total energy content can also be measured, and have estimated baryonic matter to contribute with 5%, and DM with 23%, to the total energy content of the universe [17]. Predictions of the quantity of helium, deuterium and lithium produced in an early era of the universe, called the primordial nucleosynthesis, exactly match contemporary data of the measured elements under the assumption that baryonic matter constitutes 5% of the total energy content [18].

Although the particle nature of DM has not yet been confirmed, intriguing hints have been detected by different experiments. Discussed more thoroughly in the next section 2.2, annihilation between two DM particles are thought to produce especially gamma rays and positron-electron pairs. Surprisingly, experiments such as the Energetic Gamma-Ray Experiment Tele-

scope (EGRET) have reported detections of excesses of gamma rays in the energy range of 10-50 GeV from the galactic centre [19, 20]. However, such gamma rays might be a result of inverse Compton scattering. In 2009 excess photons in the range of a few GeV was also detected by the Fermi LAT instrument [21, 22]. The energy range is what is expected of photons from DM annihilations, although in 2016 it was argued that DM annihilations could not have been the origin of the Fermi measurements, since the photons were not smoothly distributed as would also be expected [23, 24].

Other experiments, such as the Alpha Magnetic Spectrometer 02 (AMS-02), has detected a large positron fraction  $e^+/(e^- + e^+)$  up to energies of 350 GeV [25]. The result confirms positron excesses in previous experiments, such as AMS-01 [26] and HEAT [27, 28]. However, as in the case of the gamma-rays, the origin of these excesses have been debated. DM annihilations into  $e^+$  and  $e^-$  could explain this, although the interaction would require a large annihilation cross section [29]. The Wilkinson Microwave Anisotropy Probe (WMAP) reported microwave emission from the galactic core that are not spatially correlated with any known galactic emission mechanism [30, 31]. A possible explanation would be synchrotron radiation from positrons and electrons produced in the galactic centre.

The detected excess gamma-rays, positrons and electrons are at the time of writing not considered authentic proof for DM annihilation. The excesses may have individual astrophysical explanations, such as pulsar wind and supernovae. This means that the nature of DM remains unknown. The existence of DM itself, however, is established. The main reason for this is that DM solves many problems on *all physical scales*, and alternative explanations does not. For example, attempts to modify gravity does successfully explain rotation curves, but fail on larger physical scales [32]. In conclusion, the evidence for DM is that it alone solves many problems arising from some seemingly missing mass on every physical scale in the universe.

## 2.1 Weakly interacting massive particles

There is an enormous amount of possible DM candidates. The basic fact that the extra matter is unknown, or "dark", does not supply much information. A common categorization is baryonic and non-baryonic DM candidates. Massive Compact Halo Objects (MACHOs) is the most common example of baryonic DM. They might take the form of dark stars, stellar remnants, or primordial black holes. However, it has been suggested that there cannot be enough of them to resolve the question as a result of observational constraints [33, 34]. It is generally concluded that MACHOs can only contribute with a fraction of the mass in DM halos. WIMPs and axions<sup>1</sup> are the most popular non-baryonic candidates. Ordinary massive neutrinos are too light and thus have too high velocities to be affected by gravitational wells, which makes them inappropriate as DM candidates from the perspective of large-scale structure formation. On the other hand, *sterile neutrinos* remain a possibility.

WIMPs are favoured primarily because of what is called the "WIMP miracle". As mentioned previously, data on the CMB have been used to derive the present cosmological density of both baryonic matter and the unknown DM component. The Planck telescope has found the present cosmological density of DM to be  $\Omega_\chi h^2 = 0.1120 \pm 0.0056$  [18]. For comparison, in the case of WIMPs, the cosmological density has been derived [36, 37] to be

$$\Omega_\chi h^2 \approx \frac{3 \cdot 10^{-27} \text{ cm}^3/\text{s}}{\sigma_0 v_{\text{rel}}}, \quad (2.2)$$

<sup>1</sup>Axions are hypothetical scalar particles with neutral charge and mass between  $10^{-5} - 10^{-3} \text{ eV}/c^2$ . They are postulated in the Peccei-Quinn solution [35] to the *strong CP problem* in quantum chromodynamics.

where  $h$  is related to the Hubble constant via  $H_0 = 100h \text{ kms}^{-1}\text{Mpc}^{-1}$ , and  $\overline{\sigma_0 v_{\text{rel}}}$  is the velocity averaged value of the annihilation cross section  $\sigma_0$  times the particle relative velocity  $v_{\text{rel}}$ . Combining eq. (2.2) and the Planck inferred value yield a DM annihilation cross section of  $\overline{\sigma_0 v_{\text{rel}}} \approx 3 \cdot 10^{-26} \text{ cm}^3/\text{s}$ . This cross section is close to that of *weak* interaction strength (WIMP miracle), which makes WIMPs suitable candidates for DM.

However, studies of a galaxy cluster known as the Bullet cluster puts new restrains on the annihilation cross section. Results from X-rays, gravitational lensing and optical observations estimates the cross section per unit mass as  $\sigma/m_\chi = 2.23 \cdot 10^{-33} \text{ cm}^2 \text{ c}^2/\text{eV}$  [38, 39].

## 2.2 Self-interacting dark matter

Before the suggestion of self-interacting DM, the so-called collisionless cold DM model (CCDM) was the most used one. No collisions between DM particles means that the cross-section of DM-DM scattering is zero. The term 'cold' is referring to that the DM particles moves slowly compared to the speed of light  $c$ , which is still mostly assumed today as well. Cosmological models with a mixture of roughly 35% CCDM and 65% vacuum energy match observations of the cosmic microwave background and large-scale structures on extra-galactic scales with very high accuracy [40, 41]. However, several discrepancies between observations and numerical simulations on subgalactic scales led to scepticism of the CCDM model, and there after the suggested solution of self-interaction.

One of these discrepancies is the one between simulated and observed DM halo density profiles. Remarkably, simulations of CCDM halos of all sizes consistently show cuspy halos similar to the generalised Navarro-Frenk-White (NFW) profile [42, 43]

$$\rho(r) = \frac{\rho_0}{(r/r_s)^\alpha (1 + r/r_s)^{3-\alpha}}, \quad (2.3)$$

where  $\rho_0$  is the central halo density,  $r_s$  is a scale radius, and  $\alpha$  is a free parameter. The scale radius is the characteristic radius at which the density profile is equivalent to the isothermal profile  $\rho(r) \propto r^{-2}$ . The density profile diverges as  $r^{-\alpha}$  as  $r \rightarrow 0$ . The exact value of  $\alpha$  from numerical simulations has been a subject of debate. Originally NFW suggested  $\alpha \simeq 1$  [42], but later, more high resolution findings found steeper divergences as  $\alpha \simeq 1.4$  [44].

Observations of gravitational lensing in clusters and the presence of disks in galactic halos make it possible to determine their density profiles. By observing low surface brightness galaxies (LSBG) and dwarf galaxies, chosen for their small light-to-mass ratio, their density profiles has been found to indicate cores of galactic halos with shallow density profiles [44]. Rotation curves of LSBs indicate almost flat density profiles  $\rho \propto r^0$  in the  $r \rightarrow 0$  limit, with parameter values as low as  $\alpha = 0.2$  [45], which is not as divergent as the NFW profiles of CCDM [41]. The existence of stable galactic bars in high surface brightness galaxies (HSBG), such as the one in the centre of the Milky Way, also implies low-density cores [46]. This discrepancy between the density profiles of CCDM and the observed ones are referred to as the *Cuspy halo problem*, or core-cusp problem, where the simulations indicate a cusp density profile in the galactic centre and the observations show a flat core.

Another important puzzle is the excess of galactic *substructures* in simulated DM halos compared to the number of observed satellite galaxies in Milky Way-like systems. The excess of substructures, or small matter clumps in galactic halos, is one of the most clear differences between CCDM simulations and observations. This second simulation-observation discrepancy is referred to as the *missing satellite problem*.

Naturally these discrepancies may be caused by problems with the current simulations, or the quality of observational data. However, since they persist, they might be an indication that

the DM is not collisionless. Furthermore, arguments have been put forth that self-interaction of DM particles console the discrepancies mentioned above [47, 48].

### 2.2.1 The physical impact of self-interaction

In a CCDM halo, the substructures sink into the larger halo, and their outer, hotter parts are left behind due to the tidal forces. If the cold centres of the substructures survive their journey, they join the cold gravitational cusp centre. The lack of two-particle interactions means there is no heat transport into the cusp. This implies that gravitationally stable systems with CCDM is not in *thermal* equilibrium. However, when the particles interact, the second law of thermodynamics requires that the heat must be transported to the cold cusp core in order to reach thermal equilibrium. The interactions increase the mean particle velocity and reshape the cusp halo to a smoother core. As the cooler material from the outer parts mix with the warmer inner parts the halo eventually becomes isothermal. Accretion to substructures will provide heat to the halo, but at the same time two-particle interactions will eject particles, leading to heat loss. As mentioned previously, the close to isothermal density profile is what is required to explain the flat behaviour of the rotation curves at large distances from the galactic core.

### 2.2.2 Possible interactions

Indirect detection of DM refers to the detection of end products from DM annihilation, unlike direct detection, which search for signals from DM scattering on SM nuclei. Dark matter annihilation models predicts three different types of end products; gamma rays, particle- anti-particle pairs, or neutrinos. That is, the most common annihilation channels are [49]

$$\chi\bar{\chi} \rightarrow \gamma\gamma, \gamma Z, \gamma H, \quad \text{and} \quad \chi\bar{\chi} \rightarrow q\bar{q}, W^-W^+, ZZ.$$

which in turn, generate gamma rays, particle- anti-particle pairs, or neutrinos through decay. For example the products of the second annihilation channel might decay into differently charged pions [50], which in turn decays through

$$\pi^0 \rightarrow \gamma\gamma, \quad \pi^+ \rightarrow \nu_\mu\mu^+ \rightarrow \nu_\mu e^+ \nu_e \bar{\nu}_\mu, \quad \pi^- \rightarrow \nu_\mu\mu^- \rightarrow \nu_\mu e^- \nu_\mu \bar{\nu}_e.$$

In this paper the end-products are assumed to be gamma photons by the simple reason that they are the easiest to detect. Produced charged particles are deflected in interstellar magnetic fields, thus loosing the information about their origin. The charge neutrality of gamma rays and neutrinos instead points to the source where they were produced. Since neutrinos interacts extremely weakly with other matter, they practically travel unaffected from the source of production. This does not apply to gamma rays, which can be absorbed in the interstellar medium. The reason for not considering neutrinos instead lies in the fact that, because of their extremely weak interactions, they are difficult enough to detect as to make gamma rays the favourable option for detection. A simple diagram of the gamma ray producing annihilation process is shown in fig. 2.2b.

As have been seen from the previous subsection, self-interactions might resolve several simulation observation discrepancies. In the early days of modelling and simulating self-interacting DM in galaxies, the interaction cross section was assumed to be constant. Although simulations with a constant interaction cross section did create the wanted core-like density profiles, the model fell out of favour because of several discrepancies;

- i) Gravitational lensing and X-ray data indicated that the cores of clusters are dense and ellipsoidal, where the 'constant cross section' simulations predicted them to be shallow and spherical [51, 52].

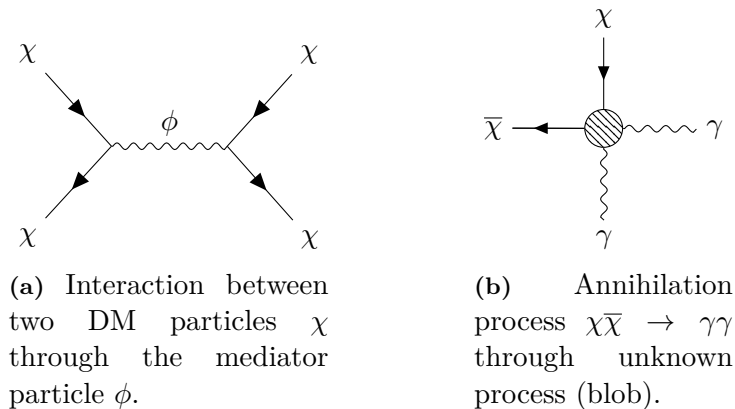


**Figure 2.2:** Two different interactions between DM particles. Fig. 2.2a illustrates self-interaction through the force carrier  $\phi$ . In fig. 2.2b a DM particle- anti-particle pair is annihilated through some unknown process into two gamma photons.

- ii) Dwarf galaxies close to a larger host galaxy would be expected to evaporate when interacting with the higher velocity DM particles in the host halo [53].
- iii) The required constant cross section was suggested to be incompatible with popular WIMP models.

In fact, results from simulations show that only a small window opens for a constant cross section model to work as a distinct alternative to the CCDM model [54]. Therefore, a velocity dependent cross section was introduced to solve the problem. The possibility that the WIMPs might interact through *dark forces*, or forces unknown to the SM, arose as a means to address other anomalies [55]. If one assumes DM annihilations to be the source of the observed gamma ray and electronic excesses, some requirements for the dark forces may be extracted. One of them is a large annihilation cross section. Studies of the AMS-02 signals seem to support a cross section much larger than what is allowed by the estimated thermal relic abundance of DM. The expected cross section for a thermal WIMP would need boost factors of order 100 to explain the positron excesses [56].

Another requirement is that the cross section must be large for leptons, but small for hadrons. Hadrons consists of baryons and mesons, which in their turn consists of three quarks, and a quark- anti-quark pair, respectively. The detected electronic excesses are an example of hard, or high energetic, leptons. Leptons are often created by a hadronic shower, that is, when hard leptons interact with other matter and produces a cascade of soft (i.e. low energy) leptons. However, observations suggest large cross sections for leptons, and small cross sections for hadrons, which is opposite of the common SM annihilation and decay sequences. Typical annihilations via Z-bosons produce very few hard leptons. The W boson produce hard leptons, but many more soft leptons trough the hadronic shower. Heavy quarks and Higgs bosons produce a even softer spectrum of leptons, all of which seem to fit the data poorly.

With the DM interpretation of the AMS-02 observed positron fraction, it is a challenge to construct ways in which DM annihilations produce leptons directly with the known SM bosons. This suggest that either the leptons are being produced from another annihilation channel, or that the DM annihilation interpretation is invalid.

However, a new interaction between DM particles can arise naturally in a variety of physics beyond the SM theories, and is considered well motivated from a theoretical point of view [55]. Even though there are strict constraint of the self-interaction cross section to form the observed

cluster- and substructures, the presence of some new force carrier  $\phi$  should be expected. See fig. 2.2a. The mediator of the force  $\phi$  could be either a scalar or a vector, since magnetic-like interactions are negligible. The force could couple to SM fields through kinetic mixing with the photon, or through mass mixing with the Higgs boson [57].

An important modification that can arise with a DM force carrier of mass  $m_\phi \simeq$  a few  $\text{GeV}/c^2$  is an enhancement of the annihilation cross section via a mechanism called the Sommerfeld enhancement [55]. This mechanism is discussed in section 4. The enhancement of the annihilation cross section could give rise to the needed large boost factors required to explain the positron excesses. However, a *massless* force carrier is disfavoured by the agreement between Big Bang nucleosynthesis and measurements of the primordial light, i.e. the CMB radiation. This leaves the conclusion that the force carrier  $\phi$  must have mass, and scattering through a massive mediator is equivalent to having a Yukawa potential. It was proposed [57] that a Yukawa potential would not only produce core density profiles in dSphs, it would also avoid all the constraints of the constant cross section model.

## Chapter 3

# Photon flux from annihilating dark matter

Having motivated our focus on photons as DM annihilation end products in the previous section, we now turn our attention to the photon flux. We start the discussion on photon flux by considering the DM annihilation rate for general product particles. The probability per unit time that a pair of DM particles  $\chi$  annihilate into a final state of SM particles, can be expressed as [58]

$$d^2\Gamma = d\sigma \cdot \Phi_\chi. \quad (3.1)$$

Here  $d\sigma$  is the differential annihilation cross-section, and  $\Phi_\chi$  is the flux from either initial particle at the position of the other one. It is defined as the product of the number density  $n_\chi$  and the relative velocity  $v_{\text{rel}}$  of the DM particles, that is

$$\Phi_\chi = v_{\text{rel}} n_\chi = v_{\text{rel}} \frac{\rho_\chi}{m_\chi}, \quad (3.2)$$

where  $\rho_\chi$  is the DM density and  $m_\chi$  the mass of the initial particle.

The velocity  $v_{\text{rel}}$  can be rewritten in a frame where the annihilating DM particles have four momenta  $P_i = (E_i, \mathbf{p}_i)$ , where  $i = 1, 2$  denotes each particle, so that

$$v_{\text{rel}} = \frac{\sqrt{(p_1 p_2)^2 - m_\chi^2}}{E_1 E_2}. \quad (3.3)$$

In the center of mass (CM) frame,  $\mathbf{p}_1 = -\mathbf{p}_2 = \mathbf{p}$  and eq. (3.3) reduces to  $v_{\text{rel}} = \left| \frac{\mathbf{p}}{E_1} - \frac{-\mathbf{p}}{E_2} \right| = |\mathbf{v}_1 - \mathbf{v}_2|$ . If the two initial particles are identical, then  $E_1 = E_2$  and  $v_{\text{rel}}$  reduces to  $v_{\text{rel}} = 2|\mathbf{v}|$ .

In a galaxy, the number density  $n_\chi$  will depend on the position in the halo. The differential cross-section  $d\sigma$  depends on the momenta of the initial and final particles, and on the particle physics model but not on spatial coordinates, if we neglect screening effects<sup>1</sup>. Then the rate of particles of type  $j$  that are generated in a volume element  $dV$  at a position  $\mathbf{r}$  in the system, containing  $n_\chi(\mathbf{r}) dV$  DM particles, can be written as

$$\frac{d^2\Gamma}{dE dV} = n_\chi(\mathbf{r}) \sum_i B_i \frac{dN_{j,i}}{dE} \overline{(\sigma_i \cdot \Phi_\chi)}_{\mathbf{r}}, \quad (3.4)$$

where  $B_i$  is the so-called branching ratio for the reaction  $i$  that produces an average of  $dN_{j,i}$  type  $j$  particles with energies  $E$  within the range  $E + dE$ . The notation  $\overline{(\cdot)}_{\mathbf{r}}$  denotes the average over all possible initial kinematics configurations of the DM particles. The branching ratio is defined as the ratio of the number of particles decaying by a specific decay mode  $k_i$  to the total number of decaying particles  $k = k_1 + k_2 + k_3 + \dots$ , that is,  $B_i = k_i/k$ .

Now, let  $P_{\mathbf{r},\text{rel}}(\mathbf{v}_{\text{rel}})$  be a probabilistic density function for the relative velocity of two DM particles colliding at a position  $\mathbf{r}$  in the dSph, such that  $P_{\mathbf{r},\text{rel}}(\mathbf{v}_{\text{rel}}) d^3\mathbf{v}_{\text{rel}}$  is the probability that

<sup>1</sup>Screening effects refers to effects effectively reducing the force attraction between two particles. For example, many electrons between a positively charged nucleus and the valence electrons are said to *shield*, or *screen* the nucleus from the perspective of the valence electrons, thus slightly reducing the electromagnetic attraction between the two.

the two particles have a velocity in the range  $[\mathbf{v}_{\text{rel}}, \mathbf{v}_{\text{rel}} + d^3\mathbf{v}_{\text{rel}}]$ . Using this, the average of initial kinematic configurations can be written as  $\frac{d^3\mathbf{v}_{\text{rel}}}{(\sigma\mathbf{v}_{\text{rel}})_r} = \int P_{r,\text{rel}}(\mathbf{v}_{\text{rel}})\sigma(\mathbf{v}_{\text{rel}})\mathbf{v}_{\text{rel}} d^3\mathbf{v}_{\text{rel}}$ , giving

$$\frac{d^2\Gamma}{dE dV} = n_\chi^2(\mathbf{r}) \sum_i B_i \frac{dN_{j,i}}{dE} \int d^3\mathbf{v}_{\text{rel}} P_{r,\text{rel}}(\mathbf{v}_{\text{rel}}) \sigma_i v_{\text{rel}}. \quad (3.5)$$

Because of Lorentz invariance, the annihilation does not depend on the orientation of the relative velocity. Thus only the magnitude of the relative velocity is needed, so that  $\Phi_\chi = n_\chi v_{\text{rel}}$  as in eq. (3.5) above.

We are now ready to consider the DM induced photon flux. For simplicity we assume that photons of all energies are of interest, and that the cross-section does not depend on the energy of the photon end products. With particle type  $j$  being a photon, we set  $j = \gamma$ , so that

$$\begin{aligned} \frac{d\Gamma}{dV} &= n_\chi^2(\mathbf{r}) N_\gamma \int d^3\mathbf{v}_{\text{rel}} P_{r,\text{rel}}(\mathbf{v}_{\text{rel}}) \sigma v_{\text{rel}} = n_\chi^2(\mathbf{r}) N_\gamma \cdot \overline{\sigma v_{\text{rel}}} \\ &= \frac{N_\gamma}{m_\chi^2} \cdot \overline{\sigma v_{\text{rel}}} \rho_\chi^2. \end{aligned} \quad (3.6)$$

Where  $N_\gamma$  is the number of photons resulting from each annihilation, and  $B_i$  has been set equal to 1.

The differential flux along a direction specified by the spherical angles  $\theta$  and  $\phi$  is [58]

$$d\Phi_\gamma = ds \frac{N_\gamma}{4\pi m_\chi^2} \cdot \overline{\sigma v_{\text{rel}}} \rho_\chi^2. \quad (3.7)$$

To evaluate the total flux, one must integrate along the line of sight  $s$  over a solid angle  $\Delta\Omega$ , so that the total flux from a galaxy is

$$\Phi_\gamma = \frac{N_\gamma}{4\pi m_\chi^2} \int_{\Delta\Omega} \int_{\text{l.o.s.}} d\Omega ds \overline{\sigma v_{\text{rel}}} \rho_\chi^2. \quad (3.8)$$

The so-called J-factor, central to our study, is the integral expression in eq. (3.8) above;

$$J = \int_{\Delta\Omega} \int_{\text{l.o.s.}} d\Omega ds \overline{\sigma v_{\text{rel}}} \rho_\chi^2 = \int_{\Delta\Omega} d\Omega \int_{\text{l.o.s.}} ds \int d^3\mathbf{v}_{\text{rel}} P_{r,\text{rel}}(\mathbf{v}_{\text{rel}}) \sigma v_{\text{rel}} \rho_\chi^2. \quad (3.9)$$

The 'classical' J-factor in eq. (1.1) usually does not include the annihilation cross section times the relative velocity, i.e. the term  $\sigma v_{\text{rel}}$ . Generally, the annihilation cross section is velocity dependent. Since the particles are moving at non-relativistic speeds, the annihilation rate factor  $\sigma v_{\text{rel}}$  can be written [37]

$$\sigma v_{\text{rel}} = a + b v_{\text{rel}}^2 + \dots, \quad (3.10)$$

where  $a$  and  $b$  are constants. Thus for low velocities, the term  $\sigma v_{\text{rel}}$  is approximately constant  $\approx a$ . Therefore, it is possible to take the term  $\sigma v_{\text{rel}}$  outside the integral. Excluding the term  $\sigma v_{\text{rel}}$ , the J-factor is defined as in section 1, by

$$J = \int_{\Delta\Omega} d\Omega \int_{\text{l.o.s.}} ds \int d^3\mathbf{v}_{\text{rel}} P_{r,\text{rel}}(\mathbf{v}_{\text{rel}}) \rho_\chi^2(s, \Omega) = \int_{\Delta\Omega} d\Omega \int_{\text{l.o.s.}} ds \rho_\chi^2(s, \Omega),$$

since the velocity distribution is normalized according to  $\int d^3\mathbf{v}_{\text{rel}} P_r = 1$ . Assuming the DM particles self-interact through an attractive Yukawa potential, their cross section will be enhanced via a mechanism called Sommerfeld enhancement, which will be discussed in the next section. The enhancement adds to the unenhanced annihilation cross section as a factor  $S$ , which unlike the annihilation rate factor, is velocity dependent. Thus, we redefine the annihilation cross

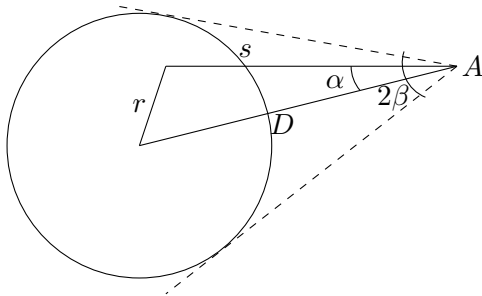


**Figure 3.1:** An observer located at  $A$  studies some properties of the galaxy at the galactic radius  $r$ . The point being studied lies at a distance  $s$  and the centre of galaxy at a distance  $D$  from  $A$ . The angle  $\beta$  represents the angle of cone tangent the locus of points a distance from the centre of the galaxy.

section as  $\sigma = \sigma_0 S(v_{\text{rel}})$ , where  $\sigma_0 v_{\text{rel}} \approx a$  denotes the unenhanced cross section and fulfills eq. (3.10). As a result,  $\sigma_0 v_{\text{rel}}$  can be taken outside the integral and the Sommerfeld enhanced J-factor  $J_S$  can be defined as

$$J_S = \int_{\Delta\Omega} d\Omega \int_{\text{l.o.s.}} ds \int d^3\mathbf{v}_{\text{rel}} P_{r,\text{rel}}(\mathbf{v}_{\text{rel}}) S(v_{\text{rel}}) \rho_\chi^2(s, \Omega), \quad (3.11)$$

where we have introduced a subscript  $S$  for Sommerfeld.

It is the evaluation of this  $J_S$  for 20 different dSphs that is the purpose of this thesis. In order to get closer to achieving this we now turn our attention to the constituents of the equation, starting with a closer examination of the geometry of the integral itself.

An approximate picture of the geometry of the problem is given in figure 3.1, where an observer studies a dSph located at a distance  $D$  from earth. The J-factor consists of an integration over the dSph's solid angle as seen from earth and over the line of sight, while we assume the dSph to be isotropic. Looking at figure 3.1 it is apparent that the distance  $r$  from the centre of the dSph to a point  $p$  can be expressed in terms of  $D$ , the distance  $s$  from earth and the angle  $\alpha$  between the centre of the dSph and  $p$  through the cosine formula as

$$r(s, \alpha, D) = \sqrt{D^2 + s^2 - 2Ds \cos \alpha}. \quad (3.12)$$

Using this and noting that the integrand is symmetric around the cone with equal  $\alpha$ , allows us to express the  $J_s$ -factor as

$$J_s = 2\pi \int_{\cos \beta}^1 d \cos \alpha \int_0^\infty ds \int d^3\mathbf{v}_{\text{rel}} P_{r(s,\alpha,D),\text{rel}}(\mathbf{v}_{\text{rel}}) S(v_{\text{rel}}) \rho_\chi^2(r(s, \alpha, D)), \quad (3.13)$$

where  $\beta$  is the maximum angle from the centre of the dSph from which DM annihilations are considered. A common practice [59, 60] is to set  $\beta = 0.5^\circ$  for all dSph satellites of the Milky Way, and that is also what will be used in this thesis.

## Chapter 4

# Annihilation cross section

The first term evaluated in eq. (3.11) will be the annihilation cross-section  $\sigma(v_{\text{rel}})$ . Since we assume self-interaction and that the majority of DM particles travels at non-relativistic velocities, one must consider the important effect of *Sommerfeld enhancement*. It will be clear later on that the enhancement plays a very important role for two slowly moving interacting particles close to each other, and will thus be highly relevant for the annihilation cross-section.

The Sommerfeld enhancement is an elementary effect in non-relativistic quantum mechanics proposed by Arnold Sommerfeld in 1931. The enhancement accounts for the effect of an interaction potential on the cross section of colliding DM particles. A simple example is an asteroid on collision course with a star. There is a probability of the asteroid colliding with the star, and the likelihood can be quantified with a cross section. If one ignores the stars gravitational pull on the asteroid, this cross section is equal to the area of the star facing the asteroid. Of course the gravitation cannot be neglected, its effect largely enhances the probability, and thus effectively the cross-section, of the asteroid colliding with the star. This enhancing effect is what is called Sommerfeld enhancement.

Another similar example is that of electron-positron annihilation. The cross-section of annihilation between a positron and an electron enhances if one accounts for the electromagnetic attraction between the particles. In the same way the cross-section is reduced by the repulsive Coulomb force between two particles of the same charge.

To generalise this, the effective cross-section of an interaction can be written

$$\sigma = \sigma_0 S, \tag{4.1}$$

where  $\sigma_0$  is the cross section neglecting any interaction potentials, and  $S$  the Sommerfeld enhancement factor accounting for potentials. Assuming that the annihilation is localised at the origin, the corresponding interaction Hamiltonian takes the form  $H = V_{\text{ann}}\delta^3(r)$ , where  $V_{\text{ann}}$  is assumed to be constant. It follows that the probability of annihilation is proportional the probability of the particle being located at the origin  $|\psi_k(0)|^2$ . Hence, our enhancement factor can be written simply as

$$S = \frac{|\psi(0)|^2}{|\psi^{(0)}(0)|^2} = |\psi(0)|^2, \tag{4.2}$$

where  $\psi^{(0)}(0)$  is the unit-normalised wave function with  $V_{\text{ann}} = 0$ . In this chapter we will develop the framework to evaluate  $|\psi(0)|$ .

Although  $\sigma v_{\text{rel}}$  does not appear in our definition of the J-factor, eq. (3.11), for completeness we will review its denotation in Appendix A.

## 4.1 Brief introduction to non-relativistic scattering theory

In order to evaluate the expression in eq. (4.2), some knowledge of general scattering theory is required.

We start by consider an incident particle travelling along the  $z$ -axis. Let its wave function represent a plane wave, such that

$$\psi(\mathbf{r}) = e^{i\mathbf{k}\cdot\mathbf{r}}. \quad (4.3)$$

where  $\mathbf{k}$  is the wave vector at distance  $\mathbf{r}$  from the origin. In our case the origin represent the site of collision, followed by annihilation, between two incident DM particles. Assuming time-independent, energy conserving scattering, in which the Hamiltonian of the system is written  $H = H_0 + V(\mathbf{r}) = -\frac{\hbar^2}{2m}\nabla^2 + V(\mathbf{r})$ , the Schrödinger equation (SE) of the scattering problem can be written

$$\left(-\frac{\hbar^2}{2m}\nabla^2 + V\right)\psi = E\psi. \quad (4.4)$$

The  $V$  is the scattering potential. The wave function is subject to the boundary condition  $\psi \rightarrow \psi_0$  as  $V \rightarrow 0$ . This equation can be rewritten as

$$(\nabla^2 + k^2)\psi = \frac{2m}{\hbar^2}V\psi. \quad (4.5)$$

In order to solve it, it is useful to note its striking resemblance to the Helmholtz equation;

$$(\nabla^2 + k^2)u(\mathbf{r}) = \rho(\mathbf{r}), \quad (4.6)$$

whose solution is well-known and can be written as

$$u(\mathbf{r}) = u_0(\mathbf{r}) - \int \frac{e^{ik|\mathbf{r}-\mathbf{r}'|}}{4\pi|\mathbf{r}-\mathbf{r}'|}\rho(\mathbf{r}')d^3\mathbf{r}'. \quad (4.7)$$

Here the function  $u_0(\mathbf{r})$  is the solution to the homogeneous equation  $(\nabla^2 + k^2)u_0(\mathbf{r}) = 0$ . With this information, eq. (4.5) can be solved, and gives together with the boundary condition  $\psi \rightarrow \psi_0$  as  $V \rightarrow 0$ , the solution

$$\psi(\mathbf{r}) = \psi_0(\mathbf{r}) - \frac{2m}{\hbar^2} \int \frac{e^{ik|\mathbf{r}-\mathbf{r}'|}}{4\pi|\mathbf{r}-\mathbf{r}'|} V(\mathbf{r}')\psi(\mathbf{r}')d^3\mathbf{r}'. \quad (4.8)$$

If we turn to areas at long distances from the scattering region  $r \gg r'$ , then  $|\mathbf{r}-\mathbf{r}'|$  can be approximated by  $r - \hat{\mathbf{r}}\cdot\mathbf{r}'$  to first order in  $r'/r$ . The unit vector  $\hat{\mathbf{r}}/r$  points from the scattering region to the observation point. It can be helpful to define  $\mathbf{k}' = k\hat{\mathbf{r}}$ , which is the wave vector for the outgoing particles from the collision with the same energy as the incoming particles ( $k' = k$ ), and propagates from the scattering region to the observation point. Then  $u(\mathbf{r})$  can be approximated as

$$\psi(\mathbf{r}) \approx e^{i\mathbf{k}\cdot\mathbf{r}} + f(\mathbf{k}, \mathbf{k}')\frac{e^{ikr}}{r}, \quad \text{where} \quad f(\mathbf{k}, \mathbf{k}') = -\frac{m}{2\pi\hbar^2} \int e^{i\mathbf{k}'\cdot\mathbf{r}'} V(\mathbf{r}')\psi(\mathbf{r}')d^3\mathbf{r}'. \quad (4.9)$$

The term  $e^{i\mathbf{k}\cdot\mathbf{r}}$  represent the incident plane wave, and the second term  $e^{ikr}/r$  an outgoing spherical wave with amplitude  $f(\mathbf{k}, \mathbf{k}')$ .

One can assume without loss of generality that the wave function of an incident particle is characterised by a wave vector  $\mathbf{k}$  which is aligned parallel to the  $z$ -axis. The scattered wave function is characterised by a wave vector  $\mathbf{k}'$  which has the same magnitude as  $\mathbf{k}$ , but generally points in a different direction. The wave vector  $\mathbf{k}'$  is specified by the polar and azimuthal angles

$\theta$  and  $\varphi$  respectively. For a spherically symmetric potential, that is  $V(\mathbf{r}) = V(r)$ , the amplitude  $f$  can be written simply as a function of  $\theta$ . It follows that neither the incident wave function  $\psi_0(\mathbf{r})$  nor the long range total wave function  $\psi(\mathbf{r})$  depends on the azimuthal angle  $\varphi$ . This enables us to simplify their expressions, so that

$$\psi_0(\mathbf{r}) = e^{ikz} = e^{ikr \cos \theta}, \quad \text{and} \quad \psi(\mathbf{r}) = e^{ikr \cos \theta} + \frac{e^{ikr} f(\theta)}{r}. \quad (4.10)$$

Without a scattering potential, or outside the range of one, both  $\psi_0$  and  $\psi$  satisfy the free SE

$$\left(\nabla^2 + k^2\right) \psi = 0. \quad (4.11)$$

A general solution in spherical coordinates, which does not depend on  $\varphi$ , is

$$\psi(r, \theta) = \sum_{l=0}^{\infty} R_l(r) P_l(\cos \theta), \quad (4.12)$$

where the  $P_l$  are the Legendre polynomials dependent on the azimuthal quantum number  $l$  associated with the angular momentum. Since the Legendre polynomials are related to the spherical harmonics by

$$P_l(\cos \theta) = \sqrt{\frac{4\pi}{2l+1}} Y_{l,m=0}(\theta, \phi),$$

combining eq. (4.11) and eq. (4.12) gives the homogeneous radial SE

$$\frac{d^2}{dr^2} R_l + \frac{2}{r} \frac{d}{dr} R_l + \left(k^2 - \frac{l(l+1)}{r^2}\right) R_l = 0. \quad (4.13)$$

The two independent solutions to this equation are the spherical Bessel functions,  $j_l(kr)$  and  $y_l(kr)$ , where

$$\begin{cases} j_l(kr) = (kr)^l \left(-\frac{1}{kr} \frac{d}{dr}\right)^l \frac{\sin(kr)}{kr}, \\ y_l(kr) = -(kr)^l \left(-\frac{1}{kr} \frac{d}{dr}\right)^l \frac{\cos(kr)}{kr}. \end{cases} \quad (4.14)$$

Note that  $y_l(kr)$  is not well-behaved when  $r \rightarrow 0$ , that is, they become singular. In contrast  $j_l(kr)$  are well-behaved because they will approach zero regularly as  $r^l$ . More precisely, in the  $r \rightarrow 0$  limit, they behave as

$$j_l(kr) \xrightarrow{r \rightarrow 0} \frac{2^l l!}{(2l+1)!} (kr)^l, \quad \text{and} \quad y_l(kr) \xrightarrow{r \rightarrow 0} -\frac{(2l)!}{2^l l!} (kr)^{-(l+1)}. \quad (4.15)$$

This is also the reason why only  $j_l(kr)$  is included in a partial wave expansion of  $e^{ikr \cos \theta}$ , which can be written [61]

$$e^{ikr \cos \theta} = \sum_{l=0}^{\infty} a_l i^l j_l(kr) P_l(\cos \theta), \quad (4.16)$$

where  $a_l$  is a constant. The factor  $i^l$  ensures that  $j_l(kr)$  is real. This can be seen by taking the complex conjugate of eq. (4.16) and at the same time let  $\cos \theta \rightarrow -\cos \theta$ , which leaves  $e^{ikr \cos \theta}$  intact. The term  $i^l P(\cos \theta)$  changes into

$$(-i)^l P_l(-\cos \theta) = i^l P(\cos \theta), \quad \text{since} \quad P_l(\cos \theta) = \frac{1}{2^l l!} \left(\frac{d}{d \cos \theta}\right)^l (\cos^2 \theta - 1)^l,$$

so that  $j_l(kr)$  must be real. By recalling the orthogonality relation for Legendre polynomials,

$$\frac{1}{2} \int_{-1}^1 dx P_l(x) P_{l'}(x) = \frac{\delta_{ll'}}{2l+1}, \quad (4.17)$$

we note that  $j_l(kr)$  is given explicitly by the integral

$$a_l i^l j_l(kr) = \frac{2l+1}{2} \int_{-1}^1 d\zeta P_l(\zeta) e^{ikr\zeta}, \quad (4.18)$$

where  $\zeta = \cos \theta$ . In order for the expression of  $j_l(kr)$  in eq. (4.18) to equal that of eq. (4.14), the constant  $a_l$  is determined to  $a_l = 2l+1$ .

In the following section, waves at long distances will be of interest. In order to expand eq. (4.16) for waves at long distances, it is practical to study the asymptotic behaviour of  $i^l j_l(x)$  for  $x = kr \gg 1$ . We do that by performing the integration of the defined expression of  $i^l j_l(x)$  followed by a large  $x$  approximation. That is,

$$\begin{aligned} i^l j_l(x) &= \frac{1}{2} \int_{-1}^1 d\zeta P_l(\zeta) \frac{d}{d\zeta} \frac{e^{ix\zeta}}{ix} \\ &= \frac{1}{2} \left[ P_l(1) \frac{e^{ix}}{ix} - P_l(-1) \frac{e^{-ix}}{ix} \right] - \frac{1}{2} \int_{-1}^1 d\zeta \frac{e^{ix\zeta}}{ix} \frac{d}{d\zeta} P_l(\zeta) \\ &\simeq \frac{1}{2ix} \left[ e^{ix} - (-1)^l e^{-ix} \right] \\ &= i^l \frac{1}{2ix} \left( i^{-l} - i^l e^{-ix} \right), \end{aligned}$$

or more simply

$$j_l(x) \simeq \frac{\sin(x - \frac{\pi l}{2})}{x}. \quad (4.19)$$

By the same method, the asymptotic behaviour of  $y_l(kr)$  is given by  $y_l(x) \simeq -\frac{\cos(x - \frac{\pi l}{2})}{x}$ . In conclusion, the asymptotic expansion of the plane wave  $e^{ikz} = e^{ikr \cos \theta}$  in terms of Legendre's polynomials is

$$\psi_0(r) = e^{ikr \cos \theta} \simeq \sum_l (2l+1) i^l \frac{\sin(kr - \frac{\pi l}{2})}{kr} P_l(\cos \theta), \quad \text{for large } r\text{'s}. \quad (4.20)$$

The most general expression for the total wave function outside the scattering region is

$$\psi(r) = \sum_l [A_l j_l(kr) - B_l y_l(kr)] P_l(\cos \theta), \quad (4.21)$$

where  $A_l$  and  $B_l$  are constants, and the  $y_l(kr)$ 's are allowed to appear if the region of validity is changed to not include the origin. As shown previously the total wave function for large  $r$ 's is reduced to

$$\psi(r) \simeq \sum_l \left[ A_l \frac{\sin(kr - \frac{\pi l}{2})}{kr} - B_l \frac{\cos(kr - \frac{\pi l}{2})}{kr} \right] P_l(\cos \theta). \quad (4.22)$$

By combining the sine and cosine expressions, one can form a resulting phase shifted sine function, so an equivalent expression to eq. (4.22) is given by

$$\psi(r) \simeq \sum_l C_l \frac{\sin(kr - \frac{\pi l}{2} + \delta_l)}{kr} P_l(\cos \theta). \quad (4.23)$$

The phase-shift is given by  $\delta_l$ , which is also called the scattering phase, and the constants  $A_l$  and  $B_l$  can be written as  $A_l = C_l \cos \delta_l$  and  $B_l = -C_l \sin \delta_l$ . Eq. (4.23) contains both the incoming and outgoing waves. By considering eq. (4.10), the *outgoing* wave is

$$\psi - \psi_0 = \frac{e^{ikr}}{r} f(\theta), \quad (4.24)$$

which implies that the coefficients for the *incoming* spherical waves at the large  $r$ -expansions must be the same. Evaluating (4.24) with the expressions of  $\psi$  and  $\psi_0$  in eq. (4.23) and eq. (4.20) respectively yields the coefficient  $C_l$ , as

$$C_l = (2l + 1) i^l e^{\delta_l}. \quad (4.25)$$

Thus, the total wave function at large  $r$ 's is given by

$$\psi(r) \simeq \sum_l (2l + 1) i^l e^{\delta_l} \frac{\sin(kr - \frac{\pi l}{2} + \delta_l)}{kr} P_l(\cos \theta). \quad (4.26)$$

In the next subsection the behaviour of scattered particles at long distances from the collision site will be used as boundary conditions, which in turn will be used in the determination of a general Sommerfeld enhancement factor for arbitrary potentials.

## 4.2 General Sommerfeld enhancement factor

In order to evaluate the enhancement in eq. (4.2) analytically, an explicit expression for the wave function  $\psi(\mathbf{r})$  at the annihilation point must be determined. Consider a central potential  $V(r)$ , either attracting or repelling an initial particle to another one, causing the interacting cross-section to increase or decrease, respectively. The potential  $V(r)$  might be treated perturbatively, but at small velocities the potential may not be a small perturbation, and could therefore distort the wave function significantly. Because of this reason we choose not to use perturbation in our derivation.

The sought for wave function with an arbitrary potential  $V$  is determined in the traditional sense by the solution of the SE

$$\left( -\frac{1}{2m} \nabla^2 + V(r) \right) \psi = \frac{k^2}{2m} \psi, \quad (4.27)$$

with the boundary condition that the annihilation can only produce spherically symmetric outgoing waves,

$$\psi \rightarrow e^{ikz} + f(\theta) \frac{e^{ikr}}{r}, \quad r \rightarrow \infty. \quad (4.28)$$

in the large  $r$  limit as discussed in the previous section. Here  $m$  denotes the reduced mass of the two body system of DM particles, and  $k$  its relative momentum. It is known that any solution of the SE with rotational invariance around an axis can be expanded as

$$\psi = \sum_l A_l P_l(\cos \theta) R_{kl}(r), \quad (4.29)$$

where the  $A_l$ 's are normalizing coefficients,  $R_{kl}$  are radial functions and  $P_l$  are Legendre polynomials. The radial SE is rewritten for later convenience, as

$$-\frac{1}{2m} \left( \frac{d^2}{dr^2} R_{kl} + \frac{2}{r} \frac{d}{dr} R_{kl} \right) + \left( \frac{l(l+1)}{r^2} + V(r) \right) R_{kl} = \frac{k^2}{2m} R_{kl}. \quad (4.30)$$

As seen in the previous section, when  $r \rightarrow \infty$  the radial Bessel functions  $j_l$  and  $y_l$  look like plane waves. Even though the radial functions  $R_{kl}$  does not solve the homogeneous SE like the Bessel functions, the asymptotic behaviour at the large  $r$  limit is the same. We choose a normalized version of  $R_{kl}$  for large  $r$ 's as

$$R_{kl}(r) \xrightarrow{r \rightarrow \infty} \frac{1}{r} \sin \left( kr - \frac{1}{2}\pi l + \delta_l \right), \quad (4.31)$$

where the scattering phase-shift  $\delta_l \geq kr$ , as  $r \rightarrow \infty$ . Using the asymptotic expansion of  $e^{ikz}$ , that is

$$e^{ikz} \rightarrow \frac{1}{2ikr} \sum_l (2l+1) P_l(\cos\theta) \left( e^{ikr} - (-1)^l e^{-ikr} \right), \quad (4.32)$$

as shown previously, the coefficients  $A_l$  can be chosen to ensure the boundary condition of eq. (4.28), and thus the partial wave expansion of  $\psi$  can be determined to

$$\psi = \frac{1}{k} \sum_l i^l (2l+1) e^{i\delta_l} P_l(\cos\theta) R_{kl}(r). \quad (4.33)$$

Note that this result is equivalent to eq. (4.26) in the large  $r$  limit as upon a slightly different choice of normalization of  $R_{kl}$ . In order to obtain a sensible physical result, we have to require that the radial function  $R_{kl}$  have a so-called regularly varying behaviour for  $r \rightarrow 0$ . That is, if the potential does not vary faster than  $r^{-1}$  at the origin,  $R_{kl}$  must scale regularly as  $\sim r^l$  as  $r \rightarrow 0$ . At the origin  $r = 0$ , which we will set as the site of annihilation, it applies that  $R_{kl} = 0$  for all  $l \neq 0$ . As we are not interested in the solution  $R_{kl} = 0$ , we must have a s-wave ( $l = 0$ ) annihilation cross-section with the enhancement factor

$$S = |\psi(r=0)|_{l=0}^2 = \left| \frac{R_{k,l=0}(r=0)}{k} \right|^2. \quad (4.34)$$

By making the standard substitution  $R_{k,l=0} = \chi/r$ , the SE in eq. (4.30) turns into the one-dimensional problem

$$\left( -\frac{1}{2m} \frac{d^2}{dr^2} + V(r) \right) \chi = \frac{k^2}{2m} \chi, \quad (4.35)$$

with the transformed boundary conditions

$$\chi(r) \rightarrow \sin(kr + \delta), \quad \text{as } r \rightarrow \infty. \quad (4.36)$$

Note that the phase-shift  $\delta$  is equal to the previously defined  $\delta_l$  with  $l = 0$ . Since  $R_{k,l=0}$  goes to a constant as  $r \rightarrow 0$ , we must have that  $\chi = rR_{kl}(r) \rightarrow 0$  as  $r \rightarrow 0$ . This regular behaviour can also be written [55]

$$\chi(r) \rightarrow r \frac{d\chi}{dr}(0), \quad \text{for } r \rightarrow 0, \quad (4.37)$$

where the correct value of  $\chi'(0) = d\chi(0)/dr$  is determined with the requirement that  $\chi$  must have unit amplitude, as in the BC of eq. (4.36).

To sum up, the enhancement can now be written as

$$S = \left| \frac{d\chi(0)}{dr} \right|^2, \quad (4.38)$$

where  $\chi$  is the solution to the 1D SE in eq. (4.35), satisfying the boundary conditions in eq. (4.36) and (4.37). We can verify that this expression is correct with a vanishing potential. With

$V(r) = 0$ , the solution to eq. (4.35) is  $\chi(r) = c \sin(kr)$ , with the complex constant  $c$ . Matching this with eq. (4.36) forces the constant to  $c = 1$ . Then the derivative  $\chi'(0) = k$  and we get  $S = 1$ , that is, no enhancement, as it should be.

With the boundary condition  $\chi \propto e^{ikr}$  as  $r \rightarrow \infty$  instead of the ones in eq. (4.36) and (4.37), the Sommerfeld factor can be equally written as

$$S_k = \left| \frac{\chi(\infty)}{\chi(0)} \right|^2. \quad (4.39)$$

In order to see the equivalence, we note that since eq. (4.35) is a second order differential equation, it must have two independent solutions. The first one, let us call it  $\chi_1$ , solves (4.35) with the boundary conditions  $\chi_1(r \rightarrow \infty) \rightarrow \sin(kr + \delta)$  and  $\chi_1'(0) = 0$ . Let  $\chi_2$  denote the second, so far unknown, linearly independent solution with boundary condition  $\chi_2(r \rightarrow \infty) \rightarrow \cos(kr + \delta)$  and define  $C = \chi_2'(0)$ . The two solutions can be compared with the two different Bessel function solutions  $j_l$  and  $y_l$  in the previous section. In general, for a  $n^{\text{th}}$  order linear differential equation, if  $n - 1$  solutions are known, the last one can be determined using the so-called *Wronskian*. Generally, for  $n$  real or complex functions  $f_1, f_2, \dots, f_n$ , which are  $n - 1$  times differentiable, the Wronskian is defined as

$$W(f_1, \dots, f_n)(x) = \begin{vmatrix} f_1(x) & f_2(x) & \cdots & f_n(x) \\ f_1'(x) & f_2'(x) & \cdots & f_n'(x) \\ \vdots & \vdots & \ddots & \vdots \\ f_1^{(n-1)}(x) & f_2^{(n-1)}(x) & \cdots & f_n^{(n-1)}(x) \end{vmatrix} \quad (4.40)$$

for  $x \in I$ . That is, a determinant of a matrix constructed by setting the functions on the first row, followed by the derivatives of those functions in increasing order.

Now returning to our problem. Using the Wronskian to find our second solution  $\chi_2$ , we have that

$$W = \chi_1(r)\chi_2'(r) - \chi_1'(r)\chi_2(r). \quad (4.41)$$

One verifies easily that  $W' = 0$  because there are no  $\chi'$  terms in the SE (4.35) above. But by comparing the boundary values of  $\chi_1$  and  $\chi_2$  at  $r \rightarrow \infty$  and  $r \rightarrow 0$ , the conserved Wronskian is

$$W(\infty) = -k(\sin^2(kr + \delta) + \cos^2(kr + \delta)) = -k = W(0) = -C\chi_1'(0), \quad (4.42)$$

since  $\chi_1(0) = 0$ . It becomes clear that  $|\chi_1'(0)| = k/|C|$  and the new expression for the Sommerfeld enhancement, using  $\chi_1$ , is simply

$$S_k = \left| \frac{\chi_1'(0)}{k} \right|^2 = \frac{1}{|C|^2}. \quad (4.43)$$

We evaluate eq. (4.39) by first noting the boundary conditions  $\chi'(r) \rightarrow ik\chi(r)$  in the large  $r$  limit since  $\chi(r) \propto e^{ikr}$  as  $r \rightarrow \infty$ , and  $\chi(0) = 1$ . Now we are ready to form  $\chi$  by the linear combination  $\chi = A(\chi_2 + i\chi_1)$  as a consequence of the asymptotic behaviour at large  $r$ . Then it must apply that  $\chi(0) = AC = 1$  and thus  $S = |A|^2 = 1/|C|^2$  as derived previously. Thereby eq. (4.38) and eq. (4.39) are equivalent general expressions for the Sommerfeld enhancement factor.

### 4.3 Case of attractive Yukawa potential

As mentioned in section 2, it has been shown [57] that DM particles interacting through a Yukawa potential could naturally explain the core structures in dSphs. The Yukawa potential can be written

$$V_Y(r) = \pm \frac{\alpha}{r} e^{-m_\phi r}, \quad (4.44)$$

where  $\alpha$  is the coupling strength and  $m_\phi$  is the mass of the force mediator particle  $\phi$  between the interacting DM particles. As the DM particles, the mediator particles  $\phi$  are not known members of the SM. Note that the Coulomb potential of electromagnetism is a special case of the Yukawa potential, with the photon  $\gamma$  as mediator particle, and  $m_\gamma = 0$ .

In order to evaluate the expression in eq. 4.43, we evaluate the SE for  $\chi$  eq. 4.35 with a Yukawa potential, that is, with  $l = 0$  as before

$$-\frac{1}{2m}\chi'' + \left(\frac{\alpha}{r}e^{-m_\phi r} - \frac{k^2}{2m}\right)\chi = 0. \quad (4.45)$$

The boundary conditions for  $\chi$  are equivalent to those of  $R_{kl}$  discussed previously, gathered below as

$$\begin{cases} \chi(r) \rightarrow (kr)^{l+1} \underset{l=0}{=} kr & \text{as } r \rightarrow 0, \\ \chi(r) \rightarrow C\sin(kr + \delta), & \text{as } r \rightarrow \infty. \end{cases} \quad (4.46)$$

To make it easier to evaluate the first boundary condition above, we can put  $x = kr$ , and  $R_{kl} = k\Phi$ . Thus the redefined radial SE is written

$$-\frac{1}{2m}\frac{1}{r^2}\frac{d}{dr}\left(r^2\frac{d}{dr}k\Phi\right) + \left(\frac{\alpha}{r}e^{-m_\phi r} - \frac{k^2}{2m}\right)k\Phi = 0. \quad (4.47)$$

In order to write the SE in terms of DM particle mass  $m_\chi$ , the reduced mass  $m = m_\chi^2/2m_\chi = m_\chi/2$  is used to define the relative velocity by  $v_{\text{rel}} = k/m_\chi$ ,  $a = \alpha/2v_{\text{rel}}$  and  $b = m_\phi/m_\chi v_{\text{rel}}$ . This gives us

$$\Phi'' + \frac{2}{x}\Phi' + \left(1 + \frac{2a}{x}e^{-bx}\right)\Phi = 0. \quad (4.48)$$

Note that with the defined  $x = kr$ , we have that  $R_{kl} = \chi/r = k\chi/x = \Phi/x$ . Using  $\Phi$  instead of  $\chi$  provides us with the easier boundary conditions [62]

$$\Phi(0) = 1, \quad \text{and} \quad \Phi'(0) = -a. \quad (4.49)$$

Together with the usual asymptotic behaviour

$$x\Phi(x) \rightarrow C\sin(x + \delta), \quad \text{as } x \rightarrow \infty, \quad (4.50)$$

the amplitude  $C$  can be determined by

$$C^2 = \lim_{x \rightarrow \infty} \left[ x^2\Phi(x)^2 + (x - \pi/2)^2\Phi(x - \pi/2)^2 \right]. \quad (4.51)$$

Thus, the Sommerfeld enhancement for a Yukawa potential is given by

$$S = \frac{1}{C^2} = \frac{1}{\lim_{x \rightarrow \infty} \left[ x^2\Phi(x)^2 + (x - \pi/2)^2\Phi(x - \pi/2)^2 \right]}. \quad (4.52)$$

Concrete values of this factor are obtained by solving the SE (4.48) numerically, since it cannot be done analytically, using the boundary conditions in eq. (4.49). In the  $x \rightarrow \infty$  limit, the constant  $C^2$  will stabilize at a value, which naturally depends on the parameter choice of  $a$  and  $b$ . This is shown in section 8.1, where the solution  $\Phi(x)$  to eq. (4.49) and the corresponding Sommerfeld enhancement are computed numerically.

## Chapter 5

# Velocity distribution

Having evaluated the Sommerfeld enhanced cross section term in (3.11), we now turn our attention to the relative velocity distribution term,  $P_{\mathbf{r},\text{rel}}(\mathbf{v}_{\text{rel}})$ . The relative velocity distribution is a probability distribution for the relative velocity  $\mathbf{v}_{\text{rel}} \equiv \mathbf{v}_1 - \mathbf{v}_2$  of two DM particles with velocities  $\mathbf{v}_1$  and  $\mathbf{v}_2$  at a position  $\mathbf{r}$ . To find an expression for this, we must first consider the motion of individual DM particles.

Considering dark matter in systems in weak gravitational fields, for example dSphs, most of DM particles will move at non-relativistic speeds  $v$  around  $10^{-5}c$  to  $10^{-4}c$  [63], the exception being the region close to a black hole. Because of this, the annihilating DM particles can be described by a Newtonian distribution function (DF)  $f$  in the so called *phase space*, which is a 6-dimensional space  $\mathbf{w} = (\mathbf{r}, \mathbf{v})$ , representing a particles 3-dimensional position  $\mathbf{r}$  and 3-dimensional momentum  $\mathbf{v}$ . The DF  $f(\mathbf{r}, \mathbf{v}, t) d^3\mathbf{r} d^3\mathbf{v}$  is the probability that a particle has phase-space coordinates in the range  $[(\mathbf{r}, \mathbf{v}), (\mathbf{r} + d^3\mathbf{r}, \mathbf{v} + d^3\mathbf{v})]$  at time  $t$ . Note that we use the velocity  $\mathbf{v}$  instead of momentum  $\mathbf{p}$  as standard notation, thus redefining the DF so that it corresponds to the *mass density* in phase-space. Using the concept of phase-space, the mass density of DM particles  $\rho_\chi$  can be defined as

$$\rho_\chi \equiv \int d^3\mathbf{v} f(\mathbf{r}, \mathbf{v}). \quad (5.1)$$

This way the DM particles at position  $\mathbf{r}$  follow a normalised velocity distribution of the form

$$P_{\mathbf{r}}(\mathbf{v}) = \frac{f(\mathbf{r}, \mathbf{v})}{\rho_\chi(\mathbf{r})}. \quad (5.2)$$

In the CM frame, this expression can be further simplified. In this frame, the pair of DM particles travels with the centre of mass velocity  $\mathbf{v}_{\text{cm}} = \frac{\mathbf{v}_1 + \mathbf{v}_2}{2}$  and relative velocity  $\mathbf{v}_{\text{rel}} = \mathbf{v}_1 - \mathbf{v}_2$ . That is

$$\begin{aligned} P_{\mathbf{r}}(\mathbf{v}_1)P_{\mathbf{r}}(\mathbf{v}_2) d^3\mathbf{v}_1 d^3\mathbf{v}_2 &= P_{\mathbf{r}}(\mathbf{v}_{\text{cm}} + \mathbf{v}_{\text{rel}}/2)P_{\mathbf{r}}(\mathbf{v}_{\text{cm}} - \mathbf{v}_{\text{rel}}/2) d^3\mathbf{v}_{\text{cm}} d^3\mathbf{v}_{\text{rel}} \\ &\equiv P_{\mathbf{r},\text{pair}}(\mathbf{v}_{\text{cm}}, \mathbf{v}_{\text{rel}}) d^3\mathbf{v}_{\text{cm}} d^3\mathbf{v}_{\text{rel}}. \end{aligned} \quad (5.3)$$

From this it is possible to construct the sought-after *relative* velocity distribution through integration over  $\mathbf{v}_{\text{cm}}$ , as

$$P_{\mathbf{r},\text{rel}}(\mathbf{v}_{\text{rel}}) = \int P_{\mathbf{r},\text{pair}}(\mathbf{v}_{\text{cm}}, \mathbf{v}_{\text{rel}}) d^3\mathbf{v}_{\text{cm}}. \quad (5.4)$$

This gives a feasible way of evaluating  $P_{\mathbf{r},\text{rel}}(\mathbf{v}_{\text{rel}})$  once the DF is determined. In general this can in itself be a very difficult task, but the complexity is greatly reduced by assuming that the system is spherically symmetric in both  $\mathbf{r}$ - and  $\mathbf{v}$ -space. Luckily, this is a rather good approximation for a dSph [64].

In order to determine the DF, we begin this chapter by deriving the so-called Eddington's formula, which is a generic expression for the DF of an isotropic system. After that, an evaluation of  $P_{\mathbf{r},\text{rel}}$  in an isotropic system will be made. These will, when put together, give an expression for  $P_{\mathbf{r},\text{rel}}(\mathbf{v}_{\text{rel}})$  that can be directly calculated once the DM mass density  $\rho(r)$  and the gravitational potential  $\Phi(r)$  have been determined.

## 5.1 Eddington's formula

Eddington's formula is a commonly used formula that expresses the DF of a spherical, isotropic system as a function of the gravitational potential  $\Phi(r)$  and mass density distribution  $\rho(r)$  of the system. To derive it, we begin by restating that the density of matter in a system can be expressed as

$$\rho(\mathbf{r}) \equiv \int d^3\mathbf{v} f(\mathbf{r}, \mathbf{v}),$$

where  $f(\mathbf{r}, \mathbf{v})$  is the DF of the system. In a spherical, isotropic system this DF is dependent only on the magnitude of the  $\mathbf{r}$  and  $\mathbf{v}$  vectors, making the integral spherically symmetric in both  $\mathbf{r}$  and  $\mathbf{v}$  space, yielding

$$\rho(r) = 4\pi \int dv v^2 f(r, v). \quad (5.5)$$

In an isotropic system with a known gravitational potential  $\Phi(r)$  it is possible to derive a unique DF that only depends on the phase-space coordinates through the Hamiltonian [65]

$$H(r, v) = \Phi(r) - \frac{v^2}{2}. \quad (5.6)$$

It is now convenient to define the relative potential and the relative energy of a particle to be

$$\Psi(r) \equiv -\Phi(r) + \Phi_0, \quad \text{and} \quad \mathcal{E} \equiv -H + \Phi_0 = \Psi(r) - \frac{v^2}{2}, \quad (5.7)$$

for some constant  $\Phi_0$ . For an isolated system extending to infinity  $\Phi_0$  is typically set to 0 so that  $\Psi(r) = -\Phi(r)$  and  $f = 0$  for  $\mathcal{E} \leq 0$ . If the DF can be described as a function of  $H$ , then it can also be described as a function of  $\mathcal{E}$ , since they differ only by a constant. This means that (5.5) can be expressed as

$$\rho = 4\pi \int dv v^2 f\left(\Psi - \frac{v^2}{2}\right) = 4\pi \int_0^\Psi d\mathcal{E} f(\mathcal{E}) \sqrt{2(\Psi - \mathcal{E})}. \quad (5.8)$$

Derivation of both sides with respect to  $\Psi$  yields

$$\frac{d\rho}{d\Psi} = \frac{4\pi}{\sqrt{2}} \int_0^\Psi \frac{f(\mathcal{E})}{\sqrt{\Psi - \mathcal{E}}} d\mathcal{E}. \quad (5.9)$$

This expression can be recognised as a so-called Abel integral equation, and by using the *Abel transform* [66]

$$p(x) = \int_0^x \frac{g(t)}{\sqrt{x-t}} dt \quad \Leftrightarrow \quad g(t) = \frac{1}{\pi} \frac{d}{dt} \int_0^t \frac{p(x)}{\sqrt{t-x}} dx, \quad (5.10)$$

one can write the DF as a function of the relative energy  $\mathcal{E}$  that relates to the density profile. Thus yielding Eddington's formula that relates the velocity distribution function  $f(\mathcal{E})$  to the density profile  $\rho(r)$  by

$$f(\mathcal{E}) = \frac{1}{\sqrt{8\pi^2}} \frac{d}{d\mathcal{E}} \int_0^\mathcal{E} \frac{d\rho}{d\Psi} \frac{d\Psi}{\sqrt{\mathcal{E} - \Psi}} = \frac{1}{\sqrt{8\pi^2}} \left[ \int_0^\mathcal{E} \frac{d^2\rho}{d\Psi^2} \frac{d\Psi}{\sqrt{\mathcal{E} - \Psi}} + \frac{1}{\sqrt{\mathcal{E}}} \left( \frac{d\rho}{d\Psi} \right)_{\Psi=0} \right]. \quad (5.11)$$

This expression can be rather difficult to evaluate, however, since  $\rho$  is rarely given as a function of  $\Psi$ . Noting that the integrand can be rewritten by the chain rule

$$\frac{d^2\rho}{d\Psi^2} = \left( \frac{d\Psi}{dr} \right)^{-2} \frac{d^2\rho}{dr^2} + \frac{d^2r}{d\Psi^2} \frac{d\rho}{dr}, \quad (5.12)$$

and the differentiation rule for inverse functions

$$\frac{d^2 r}{d\Psi^2} = -\frac{d\Psi^2}{dr^2} \left( \frac{d\Psi}{dr} \right)^{-3}, \quad (5.13)$$

which combines into

$$\frac{d^2 \rho}{d\Psi^2} = \left( \frac{d\Psi}{dr} \right)^{-2} \left( \frac{d^2 \rho}{dr^2} - \left( \frac{d\Psi}{dr} \right)^{-1} \frac{d^2 \Psi}{dr^2} \frac{d\rho}{dr} \right), \quad (5.14)$$

it is desirable to perform a change of integration variable according to  $d\Psi = \frac{d\Psi}{dr} dr$ . This gives a more readily calculable version of the Eddington formula as

$$f(\mathcal{E}) = \frac{1}{\sqrt{8\pi^2}} \int_{\Psi^{-1}(\mathcal{E})}^{\infty} \frac{dr}{\sqrt{\mathcal{E} - \Psi(r)}} \left[ \frac{d\rho}{dr} \frac{d^2 \Psi}{dr^2} \left( \frac{d\Psi}{dr} \right)^{-2} - \frac{d^2 \rho}{dr^2} \left( \frac{d\Psi}{dr} \right)^{-1} \right]. \quad (5.15)$$

From this, the DF  $f(r, v)$  can be calculated for a given  $r$  and  $v$  by

$$f(r, v) = f\left(\Psi(r) - \frac{v^2}{2}\right) = f(\mathcal{E}). \quad (5.16)$$

## 5.2 Relative velocity distribution of an isotropic system

Before attacking the relative velocity distribution, which is our main interest, we take a look at the absolute velocity distribution given by (5.2). In a system that is isotropic in  $\mathbf{r}$  and  $\mathbf{v}$ ,  $f(\mathbf{r}, \mathbf{v})$  and  $\rho(\mathbf{r})$  are only dependent on the magnitudes  $r$  and  $v$  of  $\mathbf{r}$  and  $\mathbf{v}$ . It is thus possible to integrate over angles in both  $\mathbf{r}$ - and  $\mathbf{v}$ -space, giving an absolute velocity distribution

$$P_r(v) = \frac{(4\pi)^2 r^2 v^2 f(r, v)}{4\pi r^2 \rho(r)} = 4\pi v^2 \frac{f(r, v)}{\rho(r)}. \quad (5.17)$$

Turning our attention to the distribution  $P_{r,\text{pair}}$  defined by (5.3), we note that this is a function of  $P_r(\mathbf{v})$ , with  $\mathbf{v} = \mathbf{v}_{\text{cm}} \pm \mathbf{v}_{\text{rel}}/2$ . The spherical symmetry means that we are free to define the z-axis in  $\mathbf{v}$ -space to be along the direction of  $\mathbf{v}_{\text{rel}}$ , giving in spherical coordinates with  $z = \cos \theta$

$$\left| \mathbf{v}_{\text{cm}} \pm \frac{\mathbf{v}_{\text{rel}}}{2} \right|^2 = v_{\text{cm}}^2 + \frac{v_{\text{rel}}^2}{4} \pm \mathbf{v}_{\text{cm}} \cdot \mathbf{v}_{\text{rel}} = v_{\text{cm}}^2 + \frac{v_{\text{rel}}^2}{4} \pm v_{\text{cm}} v_{\text{rel}} z. \quad (5.18)$$

This turns (5.3) into

$$\begin{aligned} P_{r,\text{pair}}(\mathbf{v}_{\text{rel}}, \mathbf{v}_{\text{cm}}) d^3 \mathbf{v}_{\text{cm}} d^3 \mathbf{v}_{\text{rel}} &= P_r \left( v_{\text{cm}}^2 + \frac{v_{\text{rel}}^2}{4} - v_{\text{cm}} v_{\text{rel}} z \right) \\ &\times P_r \left( v_{\text{cm}}^2 + \frac{v_{\text{rel}}^2}{4} + v_{\text{cm}} v_{\text{rel}} z \right) v_{\text{cm}}^2 dv_{\text{cm}} dz d\phi_{\text{cm}} d^3 \mathbf{v}_{\text{rel}}, \end{aligned} \quad (5.19)$$

where we have expanded  $d^3 \mathbf{v}_{\text{cm}}$  into  $d^3 \mathbf{v}_{\text{cm}} = v_{\text{cm}}^2 \sin \theta dv_{\text{cm}} d\phi d\theta = v_{\text{cm}}^2 dv_{\text{cm}} d\phi dz$ . Inserting this in (5.4) and integrating over  $\phi_{\text{cm}}$  and  $\theta_{\text{cm}}$ , results in

$$\begin{aligned} P_{r,\text{rel}}(\mathbf{v}_{\text{rel}}) &= 2\pi \int_0^\infty dv_{\text{cm}} v_{\text{cm}}^2 \int_{-1}^1 dz P_r \left( v_{\text{cm}}^2 + \frac{v_{\text{rel}}^2}{4} - v_{\text{cm}} v_{\text{rel}} z \right) \\ &\times P_r \left( v_{\text{cm}}^2 + \frac{v_{\text{rel}}^2}{4} + v_{\text{cm}} v_{\text{rel}} z \right). \end{aligned} \quad (5.20)$$

Noting that the integrand is by construction independent on the direction of  $\mathbf{v}_{\text{rel}}$ , an integration can be performed over angles in  $\mathbf{v}_{\text{rel}}$ -space, giving a factor of  $4\pi v_{\text{rel}}^2$ . It is also evident that the integrand is symmetric in  $z$ , meaning that the integral over  $z$  from  $-1$  to  $1$  can be taken as two times the integral over  $z$  from  $0$  to  $1$ , giving

$$P_{r,\text{rel}}(v_{\text{rel}}) = 16\pi^2 v_{\text{rel}}^2 \int_0^\infty dv_{\text{cm}} v_{\text{cm}}^2 \int_0^1 dz P_r \left( v_{\text{cm}}^2 + \frac{v_{\text{rel}}^2}{4} - v_{\text{cm}} v_{\text{rel}} z \right) \times P_r \left( v_{\text{cm}}^2 + \frac{v_{\text{rel}}^2}{4} + v_{\text{cm}} v_{\text{rel}} z \right). \quad (5.21)$$

Finally, using the relation  $P_r = f(r, v)/\rho(r)$ , gives

$$P_{r,\text{rel}}(v_{\text{rel}}) = \frac{16\pi^2 v_{\text{rel}}^2}{\rho^2(r)} \int_0^\infty dv_{\text{cm}} v_{\text{cm}}^2 \int_0^1 dz f \left( r, v_{\text{cm}}^2 + \frac{v_{\text{rel}}^2}{4} - v_{\text{cm}} v_{\text{rel}} z \right) \times f \left( r, v_{\text{cm}}^2 + \frac{v_{\text{rel}}^2}{4} + v_{\text{cm}} v_{\text{rel}} z \right). \quad (5.22)$$

Now, assuming that this  $f(r, v)$  correspond to the Eddington formula (5.15), the limits of integration can be further shortened by looking at the behaviour of  $f(\mathcal{E})$ . Since we assume the system to be bound,  $f(\mathcal{E}) = 0$  for  $\mathcal{E} < 0$ , which is the same as stating that  $f(\mathcal{E}) = 0$  for  $v > \sqrt{2\Psi(r)}$ . This means that the integral is only non-zero when one of the conditions

$$\begin{aligned} (1) \quad & v_{\text{cm}}^2 + \frac{v_{\text{rel}}^2}{4} + v_{\text{cm}} v_{\text{rel}} z \leq 2\Psi(r) \Rightarrow z \leq \frac{2\Psi - v_{\text{cm}}^2 - v_{\text{rel}}^2/4}{v_{\text{cm}} v_{\text{rel}}}, \\ (2) \quad & \Psi \geq \left( v_{\text{cm}} + \frac{v_{\text{rel}} z}{2} \right)^2 + \frac{v_{\text{rel}}^2}{4} (1 - z) \geq \left( v_{\text{cm}} + \frac{v_{\text{rel}}}{2} \right)^2 \Rightarrow v_{\text{cm}} \leq \sqrt{2\Psi} - \frac{v_{\text{rel}}}{2}, \end{aligned} \quad (5.23)$$

is satisfied. Further noting the integral is zero for

$$0 > 2\Psi + v_{\text{cm}}^2 + \frac{v_{\text{rel}}}{4} \Rightarrow v_{\text{cm}} > \frac{\sqrt{8\Psi - v_{\text{rel}}}}{2}, \quad (5.24)$$

the full region of integration for  $v_{\text{cm}}$  and  $z$  can be rewritten, avoiding overlap, as

$$\left\{ \begin{array}{l} 0 \leq v_{\text{cm}} \leq \sqrt{2\Psi} - \frac{v_{\text{rel}}}{2}, \\ 0 \leq z \leq 1 \end{array} \right\} \cup \left\{ \begin{array}{l} \sqrt{2\Psi} - \frac{v_{\text{rel}}}{2} \leq v_{\text{cm}} \leq \frac{\sqrt{8\Psi - v_{\text{rel}}^2}}{2}, \\ 0 \leq z \leq \frac{8\Psi - v_{\text{rel}}^2 - 4v_{\text{cm}}^2}{4v_{\text{cm}} v_{\text{rel}}} \end{array} \right\}. \quad (5.25)$$

In conclusion, in order to evaluate the relative velocity distribution  $P_{r,\text{rel}}(v_{\text{rel}})$ , the expression in eq. (5.22) is integrated over the range given in eq. (5.25) above. The one thing missing from obtaining numbers, is an expression for the DM gravitational potential  $\Phi(r) = -\Psi(r)$  in a dSph. The gravitational potential can be obtained from specific DM density distributions, which is the subject of the next chapter.

# Chapter 6

## Density profiles

As mentioned in section 2, galaxies and clusters are thought to have a DM halo that encloses galactic discs and extends well beyond the edge of visible matter. In this chapter the DM halo distribution is discussed. The density profiles are needed directly in the expression for the J-factor in eq. (3.11) as well as to find an expression for the DM gravitational potential, which is included in the expression for the relative velocity distribution.

The shapes of DM halos need to be simulated or fitted by empirical formulae. For simplicity the shape of the system is assumed to be spherically symmetric, as in previous chapters. Mentioned in section 2, the general flat behaviour of rotation curves indicates a close to isothermal DM density profile. A non-singular isothermal density profile can be written  $\rho(r) = \rho_0(1 + (r/r_0)^2)^{-1}$ , where  $\rho_0$  is the density of the central region in the system and  $r_0$  is a scale radius. However, this model is not a very accurate for most galaxies. A more realistic and very general density profile is given by the so-called  $\alpha\beta\gamma$ -profile, or sometimes *generalised Hernquist profile*

$$\rho_\chi(r) = \frac{\rho_0}{\left(\frac{r}{r_0}\right)^\gamma \left(1 + \left(\frac{r}{r_0}\right)^\alpha\right)^{\frac{\beta-\gamma}{\alpha}}}. \quad (6.1)$$

Here  $r$  is the distance from the centre of the galaxy, and the parameters  $\rho_0$  and  $r_0$  will be galaxy specific. The density of stars,  $\nu$ , in a galaxy also follow a  $\alpha\beta\gamma$ -profile, but with other scale parameters  $\rho_\star$  and  $r_\star$ , as well as different values of  $(\alpha, \beta, \gamma)$ .

The density function as a function of  $r$  can generally be divided into an inner and outer slope. This is because matter density tends to be higher, especially for stellar distributions, in the centre of a galaxy, thus giving rise to a distinct central slope. This inner slope is parametrised by  $\gamma$  where  $\rho \propto r^{-\gamma}$ , the outer slope by  $\beta$  where  $\rho \propto r^{-\beta}$ . The parameter  $\alpha$  determines the sharpness of the transition between the two slopes.

For the DM density profile it is common to use the parameter choice of  $(\alpha, \beta, \gamma) = (1, 3, 1)$  or  $(1, 3, 0)$ , which is known as a *cusped* and *cored* Zhao profile [67], respectively. A cusped profile refers to a density distribution with a higher bulge around the central regions  $r = 0$ , which corresponds to  $\gamma = 1$ . The cored ( $\gamma = 0$ ) profile, which from now on will be referred as cored Zhao, has a flat behaviour in the same region. The cusped  $(1, 3, 1)$  profile is also known as the NFW-profile mentioned in section 2, which were derived from the CCDM simulations. Even though a CCDM density profile is known for *not* matching too well with observations, it is still somewhat traditional to use it in newer research for comparisons with previous results. This will, at least partly, also be the case in this report in order to compare our outcome with that of [59].

The star profiles are usually taken to be  $(\alpha, \beta, \gamma) = (2, 5, 0)$ ,  $(2, 5, 0.1)$  or  $(2, 5, 1)$ . The obtained profiles are called Plummer [68] (P), Plummer-like (PL), or non-Plummer (NP), re-

spectively;

$$\nu_{*,\text{P}}(r) = \frac{\rho_*$$

$$\nu_{*,\text{PL}}(r) = \frac{\rho_*}{\left(\frac{r}{r_*}\right)^{0.1} \left(1 + \left(\frac{r}{r_*}\right)^2\right)^{\frac{4.9}{2}}}, \quad (6.3)$$

$$\nu_{*,\text{NP}}(r) = \frac{\rho_*}{\left(\frac{r}{r_*}\right) \left(1 + \left(\frac{r}{r_*}\right)^2\right)^2}. \quad (6.4)$$

As in the case of the NFW-profile of DM, the Plummer profile is the most frequently used one in literature. In order to compare our results with other published sources, the Plummer star density profile will be used in this thesis as well. With the density profiles defined, the gravitational potential is now ready to be approached.

## 6.1 Gravitational potential in a spherical system

Adopting a general discussion, the gravitational potential  $\Phi(r)$  can be derived for a given  $\rho(\mathbf{r})$  using Gauss' gravitational law [4]

$$\int_{\partial V} d\mathbf{S} \cdot \nabla \Phi(\mathbf{r}) = 4\pi G \int_V dV \rho(\mathbf{r}), \quad (6.5)$$

where  $\partial V$  is the surface of a volume  $V$  and  $G$  is the gravitational constant. For a system with spherical symmetry it applies that  $\nabla \Phi(r) = \partial_r \Phi(r) \hat{\mathbf{r}}$ . Taking  $V$  to be a sphere of radius  $r$  centred at  $r' = 0$  then results in  $d\mathbf{S} = r^2 \sin \theta d\theta d\phi \hat{\mathbf{r}}$  and  $dV = r'^2 \sin \theta dr d\theta d\phi$ , giving

$$r^2 \partial_r \Phi(r) \int_0^{2\pi} d\phi \int_0^\pi d\theta \sin \theta = 4\pi G \int_0^{2\pi} d\phi \int_0^\pi d\theta \sin \theta \int_0^r dr' r'^2 \rho(r'). \quad (6.6)$$

Integration over the angles then gives us

$$r^2 \partial_r \Phi(r) = 4\pi G \int_0^r dr' r'^2 \rho(r'). \quad (6.7)$$

The mass  $M$  enclosed by the sphere is given by

$$M = 4\pi \int_0^r dr' r'^2 \rho(r'), \quad (6.8)$$

which results in that

$$\partial_r \Phi(r) = \frac{GM}{r^2}. \quad (6.9)$$

Since the gravitational force acting on an object in this potential is proportional to the gravitational field  $\mathbf{g} = -\nabla \Phi = -\partial_r \Phi \hat{\mathbf{r}}$ , then a particle travelling in a spherically symmetric field only feels gravitational attraction from the particles at smaller distances from the centre than itself. From this, it is also evident that the force experienced for such a particle is exactly the same as it would have been if all of the mass at smaller distances from the centre had been concentrated in a single point at the origin.

Now consider the gravitational potential of a spherical shell of radius  $a$ . According to the discussion above the potential from the shell needs to be the same as that of a point mass. Assuming  $M$  to be independent of  $r$  and integrating (6.9) gives

$$\Phi(r) = -\frac{GM}{r}, \quad r > a. \quad (6.10)$$

Accordingly, inside the shell the particle can feel no net force, giving  $\partial_r \Phi(r) = 0$ . Thus the potential inside the shell must be equal to the potential at the border, giving

$$\Phi(r) = -\frac{GM}{a}, \quad r < a. \quad (6.11)$$

The gravitational potential of a generic spherically symmetric system can now be calculated by summing up the contributions of an infinite series of shells at radii  $r'$  and with masses  $dM(r')$  giving

$$\Phi(r) = -G \left[ \frac{1}{r} \int_0^r dM(r') + \int_r^\infty \frac{dM(r')}{r'} \right]. \quad (6.12)$$

The mass of a shell at radius  $r'$  can be given in terms of  $\rho(r')$  as  $M(r') = 4\pi r'^2 \rho(r')$ , giving a final expression for the gravitational potential of a spherical system as

$$\Phi(r) = -4\pi G \left[ \frac{1}{r} \int_0^r dr' r'^2 \rho(r') + \int_r^\infty dr' r' \rho(r') \right]. \quad (6.13)$$

## 6.2 Dark matter gravitational potential of a dwarf spheroidal galaxy

Having derived an equation for the gravitational potential  $\Phi(r)$  of a general non-relativistic spherical system, all that is needed in order to determine  $\Phi(r)$  for a dSph is to decide upon a density profile that can be fitted to model the dSph. Since the dSphs are thought to be largely dominated by DM, one can assume that the DM density distribution is a good model of the density distribution as a whole. As previously noted, the cored Zhao profile

$$\rho_{\text{core}}(r) = \frac{\rho_0}{\left(1 + \frac{r}{r_0}\right)^3}, \quad (6.14)$$

is a cored density profile which has, as previously noted, proven a good fit for the observed density of dark matter in dSphs. Substituting this  $\rho(r)$  in (6.13) gives an expression for the gravitational potential that can be evaluated analytically with the help of partial fraction expansion, yielding

$$\Phi_{\text{core}}(r) = -4\pi G \rho_0 r_0^2 \left( \frac{\log\left(1 + \frac{r}{r_0}\right)}{r/r_0} - \frac{1}{2\left(1 + \frac{r}{r_0}\right)} \right), \quad (6.15)$$

for the gravitational potential from a core dSph.

Since many previous calculations have been done using the cuspy NFW DM density profile, the gravitational potential from an NFW dSph will need to be evaluated as well, in order to allow for comparison with previous results. The NFW profile, corresponding to an cusped Zhao profile, is given by

$$\rho_{\text{cusp}}(r) = \frac{\rho_0}{\frac{r}{r_0} \left(1 + \frac{r}{r_0}\right)^2}. \quad (6.16)$$

This profile is also spherical, meaning that the gravitational potential can be calculated in the same manner as the cored Zhao profile by inserting (6.16) in (6.13). The resulting expression can then be evaluated analytically, giving

$$\Phi_{\text{cusp}}(r) = -4\pi G \rho_0 r_0^2 \frac{\log\left(\frac{r}{r_0} + 1\right)}{r/r_0}. \quad (6.17)$$

Thus, the relative velocity distribution for DM can be evaluated by either using a cusped or cored gravitational potential.

# Chapter 7

## Statistical methods

In chapters 3–5 a method of evaluating the J-factor for an isotropic dSph, based on a known DM density distribution has been developed. In chapter 6 the density profiles used for the analysis were introduced. Still lacking however, is a way to determine the scale factors in the density profiles, with corresponding uncertainties, from observational data of the selected dSph.

In this chapter we will take a look at, in order, the observational data used, what our model predicts for this data, and a statistical model in the form of a likelihood function that can be used to determine the scale parameters for each galaxy and density profile.

### 7.1 Astronomical observations

When performing astronomical observations there exists a major constraint on the data that can be retrieved; namely that we are confined to a comparatively minuscule region of space to perform the observations from. When looking at distant objects such as the dSph satellites of the Milky Way we are for all practical purposes confined to a single point in space, meaning that it is difficult to triangulate the distance from the earth to a star in a distant cluster with an accuracy that is sufficient to determine their relative positions in space. The angular distance between stars as seen from earth can, however, be measured to great accuracy. Combining this with a more rough measurement of the distance to the stars then gives a rather good measurement of the distances between stars in a cluster, projected to the plane perpendicular to the line of sight. For our analysis, the distance  $R$  from the centre of the dSph to the line of sight will suffice as observable, since we assume spherical symmetry of the dSph.

The other observable that will be of use is the line of sight velocities  $v_{\text{l.o.s.}}$  of individual stars. This is measured by matching the spectroscopic fingerprints of common elements with the spectra from the stars in order to measure the Doppler shift that results from our relative velocities. Both  $R$  and  $v_{\text{l.o.s.}}$  have been collected for some of the dSph satellites of the Milky Way in [6–8]. Thus, if a connection can be made between the  $R$  and  $v_{\text{l.o.s.}}$  of the stars in a dSph and the DM density distribution, a statistical fit of the DM density parameters can be made. From this, it is rather straightforward to calculate both  $J$  and  $J_s$ .

### 7.2 Line of sight velocity dispersion

Having noted that the line of sight velocity of individual stars in a dSph makes for a good observable, we now seek a relation between that and our DM density distribution. To simplify our analysis we want to assume spherical symmetry and that there is no net rotation of the system. These assumptions make it impossible to predict the motions of individual stars relative to the motion of the galaxy centre of mass. What can be predicted, though, is the deviations from the mean l.o.s. velocity, or the *line of sight velocity dispersion*  $\sigma_{\text{l.o.s.}}^2 = \overline{v_{\text{l.o.s.}}^2} - \overline{v_{\text{l.o.s.}}}^2$  for a population of stars, based on the density distribution  $\rho(r)$  and the luminosity distribution  $\nu(r)$  of the dSph.

We will further assume that the mass content of a dSph is DM dominated enough that the baryonic matter can be safely ignored in the density distribution, such that  $\rho(r) = \rho_\chi(r)$ , where

$\rho_\chi(r)$  is the DM density. Finally, all stars are taken to have equal luminosity so that  $\nu(r)$  is equivalent to a star number density.

The radius  $r$  in above expressions is the distance from centre of the dSph. As previously noted, this is not an entity that is easily observed. Accurate measurements can however be made of the *projected distance*  $R$  on the plane perpendicular to the l.o.s. from the centre of the dSph. The relation between these entities, assuming that the observer is positioned at infinite distance, can be seen in figure 7.1.

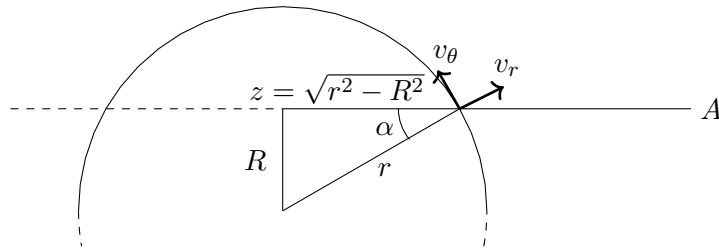


**Figure 7.1:** An observer located at  $A$  studies some properties of the galaxy at the galactic radius  $r$ . The observables are along the line of sight distance  $R$  from the centre.  $v_\theta$  and  $v_r$  are the velocity components at radius  $r$  of the galaxy. In the figure only the positive  $z$  is shown.

As will be clear in a moment, one can derive an expression for the l.o.s. star velocity dispersion  $\sigma_{\text{l.o.s.}}^2(\mathbf{r})$  at a given point  $\mathbf{r}$  in the dSph from the DM density distribution  $\rho_\chi(\mathbf{r})$ . However, when doing observations one must also take into account that the position of an observed star along the line of sight is unknown, meaning that a relation between the l.o.s. star velocity dispersion at a single point  $\sigma_{\text{l.o.s.}}^2(\mathbf{r})$  and the velocity dispersion along the l.o.s.,  $\sigma_{\text{l.o.s.}}^2(R)$  is needed. This can readily be constructed by integrating along the l.o.s. at a given  $R$ ,  $\sigma^2(\mathbf{r})$  multiplied by the probability that a star found along the l.o.s. is at a distance  $r$  from the centre of the dSph. This probability is easily found from the luminosity density to be

$$P_{*,R}(r) = \nu(r) / \int_{-\infty}^{\infty} ds \nu(r(z, R)) = \frac{\nu(r)}{I(R)}, \quad (7.1)$$

where  $s$  is the distance along the line of sight as seen in figure 7.1, and we have introduced  $I(R)$  as the *intensity* at a projected point  $R$ . This immediately gives the l.o.s. velocity dispersion as

$$\sigma_{\text{l.o.s.}}^2(R) = \int_{-\infty}^{\infty} P_{*,R}(r) \sigma_{\text{l.o.s.}}^2(r) ds = \frac{1}{I(R)} \int_{-\infty}^{\infty} dz \nu(r) \sigma_{\text{l.o.s.}}^2(r). \quad (7.2)$$

There are now two integrals over  $z$  of a function of  $r$  in the expression. From the relation  $z = \pm\sqrt{r^2 - R^2}$  one can derive the identity

$$dz = \pm \frac{r dr}{\sqrt{r^2 - R^2}}, \quad (7.3)$$

which allows for a change of integration variable to  $r$ . Because of the spherical symmetry both integrals are symmetric around  $z = 0$ , meaning that they can be taken as twice their value on  $z \in [0, \infty)$ . This gives

$$I(R) = 2 \int_R^{\infty} \frac{dr r \nu(r)}{\sqrt{r^2 - R^2}} \quad (7.4)$$

for the intensity and

$$\sigma_{\text{l.o.s.}}^2(R) = \frac{2}{I(R)} \int_R^{\infty} \frac{dr r \nu(r) \sigma_{\text{l.o.s.}}^2(r)}{\sqrt{r^2 - R^2}} \quad (7.5)$$

for the l.o.s. velocity dispersion.

Remaining is now to evaluate  $\sigma_{\text{l.o.s.}}^2(r)$  itself. Assuming no net rotation of the dSph gives that the mean l.o.s. velocity of stars at a given  $R$  is everywhere equal to the mean l.o.s. velocity of the dSph itself. Thus, the analysis can be simplified by setting  $\overline{v_{\text{l.o.s.}}} = 0$ , giving  $\sigma_{\text{l.o.s.}}^2(r) = \overline{v_{\text{l.o.s.}}^2}(r)$ . Again, noting from figure 7.1 that  $v_{\text{l.o.s.}} = v_r \cos \alpha - v_\theta \sin \alpha$  gives us

$$\begin{aligned} \sigma_{\text{l.o.s.}}^2(r) &= \overline{v_{\text{l.o.s.}}^2}(r) = \overline{(v_r \cos \alpha - v_\theta \sin \alpha)^2} \\ &= \overline{v_r^2} \cos^2 \alpha + \overline{v_\theta^2} \sin^2 \alpha = \left(1 - \beta \frac{R^2}{r^2}\right) \overline{v_r^2}, \end{aligned} \quad (7.6)$$

where the third step follows from  $\overline{v_r v_\theta} = 0$ , which is a result of spherical symmetry. In the last step, the anisotropy parameter

$$\beta \equiv 1 - \frac{\overline{v_\theta^2}}{\overline{v_r^2}} \quad (7.7)$$

has been introduced. Insertion in (7.8) then yields

$$\sigma_{\text{l.o.s.}}^2(R) = \frac{2}{I(R)} \int_R^\infty \left(1 - \beta \frac{R^2}{r^2}\right) \frac{r \overline{v_r^2} \nu(r)}{\sqrt{r^2 - R^2}} dr. \quad (7.8)$$

The final piece is now the evaluation of  $\overline{v_r^2}$ . An expression for  $\overline{v_r^2} \nu$  can be derived through modelling the motion of stars in the dSph as a collisionless Newtonian system. This model is studied in detail in appendix C and leads to a series of equations of motion called the *Jeans equations*. The equation for motion in the radial direction of a spherical system is given in (C.24), and becomes with  $\rho = \nu$ ,

$$\frac{1}{\nu} \frac{d(\nu \overline{v_r^2})}{dr} + 2 \frac{\beta \overline{v_r^2}}{r} = - \frac{GM(r)}{r^2}, \quad (7.9)$$

where  $G$  is the gravitational constant and  $M(r) = 4\pi \int_0^r dr' r'^2 \rho_\chi(r')$  is the total mass enclosed within a radius  $r$ .

Since we are only interested in isotropic systems, we now set the anisotropy parameter  $\beta$  to 0 and integrate, giving

$$\nu \overline{v_r^2} = - \int dr \frac{\nu GM(r)}{r^2}. \quad (7.10)$$

Using the fundamental theorem of calculus this can be turned into a definite integral by

$$\int_r^\infty ds \frac{\nu GM(s)}{s^2} = \int \frac{\nu GM(s)}{s^2} ds \Big|_{s=\infty} - \int \frac{\nu GM(s)}{s^2} ds \Big|_{s=r} = - \int \frac{\nu GM(r)}{r^2} dr. \quad (7.11)$$

From this, (7.8) with  $\beta = 0$  can be written as

$$\sigma_{\text{l.o.s.}}^2(R) = \frac{2}{I(R)} \int_R^\infty dr \frac{r}{\sqrt{r^2 - R^2}} \int_r^\infty ds \frac{\nu(s) GM(s)}{s^2}. \quad (7.12)$$

This is an equation where, once the density profiles  $\rho_\chi(r)$  and  $\nu(r)$  have been chosen, all constituent parts are known and a calculation can be readily performed. As discussed in chapter 6, we will in this thesis assume a Plummer density profile for  $\nu(r)$  and will consider both an NFW and a cored (1, 3, 0) profile separately for  $\rho_\chi(r)$ . The Plummer profile is given by  $\nu(r) = \rho_\star [1 + (r/r_\star)^2]^{-5/2}$ , and looking at (7.12) it is apparent that the  $\rho_\star$  can be taken outside the integral of both the main integral and of  $I(R)$ , rendering  $\sigma_{\text{l.o.s.}}^2(R)$  independent of  $\rho_\star$ . The  $r_\star$

of the Plummer profile and the  $r_0$  and  $\rho_0$  that are part of both DM profiles are still contributing to the velocity dispersion, however. In the case of the DM parameters this is a good thing, since it is necessary in order to be able to determine the DM density profile from velocity data in this manner, but the  $r_*$  is not of interest more than as a reality check and will thus be treated as a so-called *nuisance parameter* in the likelihood analysis.

### 7.3 Maximum likelihood estimation of parameters

A likelihood-based analysis is used to determine the parameters of the DM and luminosity distributions that give the best correspondence between theory and observation. Until this point, when discussing the DM density distribution, it has been in terms of the parameters  $\rho_0$  and  $r_0$ . This choice of parameters space proves to be unwieldy when performing a likelihood fitting; the physical constraints of  $\rho_0$  in particular are largely unknown and there is almost a degeneracy between  $\rho_0$  and  $r_0$  where an increase in one can be counteracted by a decrease in the other, giving almost no net change to the system. Instead,  $\rho_0$  can be replaced by the parameter  $v_0 = r_0\sqrt{G\rho_0}$ , which is just the escape velocity from the centre of a dSph divided by a constant. This  $v_0$  is much more constrained and removes the degeneracy to a large extent. Thus, the likelihood fitting will be made in terms of parameters  $r_0, v_0$  and  $r_*$ .

Although the reality is more complex, for this purpose we are going to assume the probability density for star velocities along a line of sight to be normally distributed, giving the line of sight velocity of each of the  $N$  stars of a dSph a probability density of the form

$$f_i(v_i, R_i) = \frac{1}{\sqrt{2\pi\sigma_i^2(R_i)}} \exp\left[-\frac{(v_i - u_i)^2}{2\sigma_i^2}\right], \quad (7.13)$$

where  $v_i$  is the l.o.s. velocity,  $R_i$  the perpendicular distance from the l.o.s. of the star to the centre of the dSph,  $u_i$  is the expected velocity and  $\sigma_i^2$  is the velocity variance for star  $i$ . The variance  $\sigma_i^2$  can be assumed to be the squared sum of a measurement error  $\epsilon_i$  and the velocity dispersion  $\sigma_{1.o.s.}^2(R_i)$  calculated in the previous section;  $\sigma_i^2(R_i) = \epsilon_i^2 + \sigma_{1.o.s.}^2(R_i)$ . The assumed ergodicity also makes all  $u_i$  approximately equal to the mean velocity of the stars,  $u$ . We can now construct a joint distribution function for all  $N$  stars through multiplication of the individual distributions yielding, with  $\mathbf{x}_i = (v_i, R_i, \epsilon_i)$ ,

$$f(\mathbf{x}_1, \mathbf{x}_2, \dots, \mathbf{x}_N) = \prod_{i=1}^N f_i(\mathbf{x}_i) = \prod_{i=1}^N \frac{1}{\sqrt{2\pi\sigma_i^2(R_i, \epsilon_i)}} \exp\left[-\frac{(v_i - u)^2}{2\sigma_i^2(R_i, \epsilon_i)}\right]. \quad (7.14)$$

Having determined a set of  $\mathbf{x}_i$  for stars in the dSph this distribution can be regarded as a function of  $\sigma_{1.o.s.}^2$ , or rather, the parameters  $v_0, r_0, r_*$ , in which case we have constructed a likelihood function

$$L(v_0, r_0, r_* | X) \equiv f(\mathbf{x}_1, \mathbf{x}_2, \dots, \mathbf{x}_N | v_0, r_0, r_*), \quad (7.15)$$

where  $X = (\mathbf{x}_1, \mathbf{x}_2, \dots, \mathbf{x}_N)$  is a matrix of velocity and position data for a dSph. Since the  $X$  here correspond to measured values of stars in a dSph, the true joint density function will have a maximum near these values, given that the sample is large enough. We can thus retrieve the most probable values of the parameters by maximising  $L$ . Because this  $L$  involves a product of many individual distributions, it is convenient to instead maximise the value of  $\mathcal{L} = \log L$ , which becomes

$$\mathcal{L}(v_0, r_0, r_* | X) = \frac{1}{2} \sum_{i=1}^N \left[ -\log 2\pi\sigma_i^2 - \frac{(v_i - u)^2}{\sigma_i^2} \right]. \quad (7.16)$$

The only parameters of interest for the calculation of the J-factor is the DM-related  $v_0$  and  $r_0$ , leaving  $r_\star$  as a so-called *nuisance parameter*. When performing the fit, a grid of possible values for  $v_0$  and  $r_0$  will be made. For each point in this grid,  $\mathcal{L}(v_0, r_0 | r_\star, X)$  is maximised over the nuisance parameter  $r_\star$ . The values where  $\mathcal{L}$  is at its peak will then be taken as the maximum likelihood estimate (MLE) for the parameters  $v_0, r_0$ .

In order to retrieve the uncertainty in the MLE the so-called test statistic  $TS$  can be used, which is defined as

$$TS = -\frac{1}{2}(\mathcal{L} - \mathcal{L}_{\text{MLE}}), \quad (7.17)$$

where  $\mathcal{L}_{\text{MLE}}$  is the value of  $\mathcal{L}$  at the MLE, follows [69] a  $\chi_n^2$  distribution for a likelihood function with  $n$  parameters. This means that, to get a  $100\alpha$  % confidence region of the parameters of  $L$  one must first solve the equation

$$\alpha = \int_0^{\Delta\chi} \chi_n^2(x) dx \quad (7.18)$$

for  $\Delta\chi$ . The  $TS$  then follows

$$P(TS < \Delta\chi) = \alpha. \quad (7.19)$$

From this it is simple to construct confidence regions for the parameters  $v_0, r_0$  for each dSph, in which case  $n = 2$ . In order to obtain confidence intervals for the  $J$  factors themselves, these will be calculated for each point in  $(r_0, v_0)$ -space, along with the corresponding likelihood. The resulting points will then be binned according to their  $J$  value, or rather, according to their  $\mathcal{J} = \log_{10} J$ . For each bin, the point with maximum  $L$  is selected. The resulting points then form a *binned likelihood function*  $\mathcal{L}(\mathcal{J})$ , whose  $TS$ , defined as above, then follow a  $\chi_1^2$  distribution.

## Chapter 8

# Validation of numerical implementation

Preparatory to the numerical results, the validity of some included parts in the J-factor expression are checked separately with reference literature. The parts are the Sommerfeld enhancement factor, the relative velocity distribution, and some 'classical' J-factors without Sommerfeld enhancement. Established results of these evaluated components are found in literature, and provides good verification for our final results presented in the next chapter. The code corresponding to each part of the calculations can be found in appendix E.

### 8.1 Sommerfeld enhancement

The wave function and the Sommerfeld enhancement factor for the Yukawa potential are computed by solving (4.48), with the boundary conditions in (4.49), numerically. As to avoid the singularity at  $x = 0$  in the differential equation, the boundary condition is shifted a small amount from zero for the numerical calculation. For the Sommerfeld enhancement calculation we use the Arkani-Hamed et. al. parameter profile with coupling constant  $\alpha = 0.01$  and exchange particle mass  $m_\phi = 1 \text{ GeV}/c^2$  [55]. However, another popular parameter profile is that of Lattanzi-Silk [70], with  $\alpha = 1/30$  and  $m_\phi = 90 \text{ GeV}/c^2$ . As to provide additional validation both of these profiles are used in this section. The solution of the Schrödinger equation for the Yukawa potential using the Arkani-Hamed parameters with  $m_\chi = 650 \text{ GeV}/c^2$  (also suggested by [55]) and velocity  $v = 10^{-4}c$  can be seen in fig. 8.1 as well as the  $C^2$  factor computed over the same range.

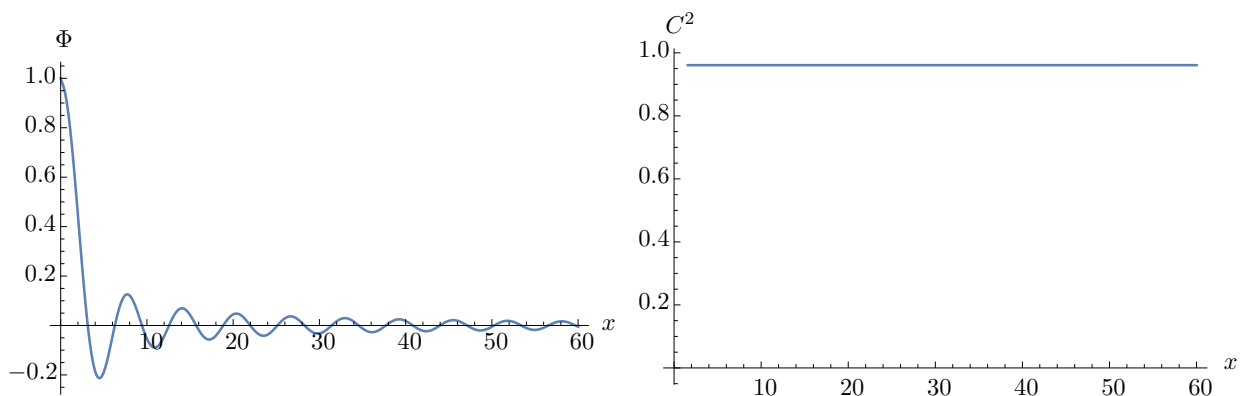


**Figure 8.1:** Numerical computation of the wave function for the Yukawa potential using the Arkani-Hamed parameters  $\alpha = 0.01$ ,  $m_\phi = 1 \text{ GeV}/c^2$ , with a DM particle mass of  $m_\chi = 650 \text{ GeV}/c^2$  and a relative velocity of  $v_{\text{rel}} = 10^{-4}c$ . The left graph shows the radial wave function while the right one the  $C^2$  value. It can be seen that  $C^2$  is about constant with a value of  $C^2 = 0.9683 \pm 0.00004$  in the entire range.

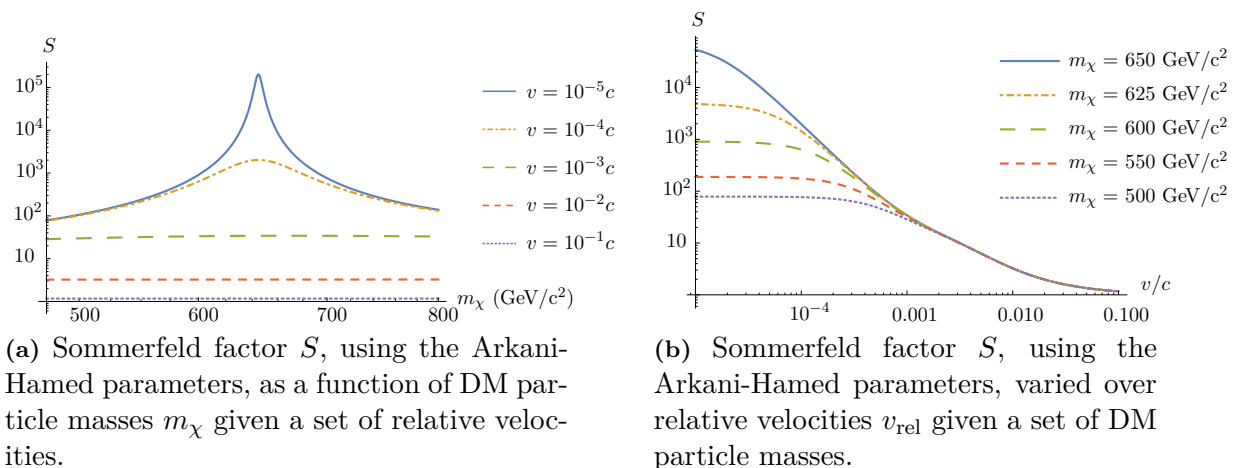


**Figure 8.2:** Sommerfeld enhancement factor varied over DM particle masses  $m_\chi$  and their relative velocities  $v_{\text{rel}}$  with Arkani-Hamed parameters  $\alpha = 0.01$ ,  $m_\phi = 1 \text{ GeV}/c^2$ . In (a) the enhancement factor for  $m_\chi = 650 \text{ GeV}/c^2$  is close to a resonance peak and hence is significantly higher than the other three displayed masses at low relative velocities. In (b) it is clear that the enhancement factor gets larger with lower relative velocities of the DM particles.

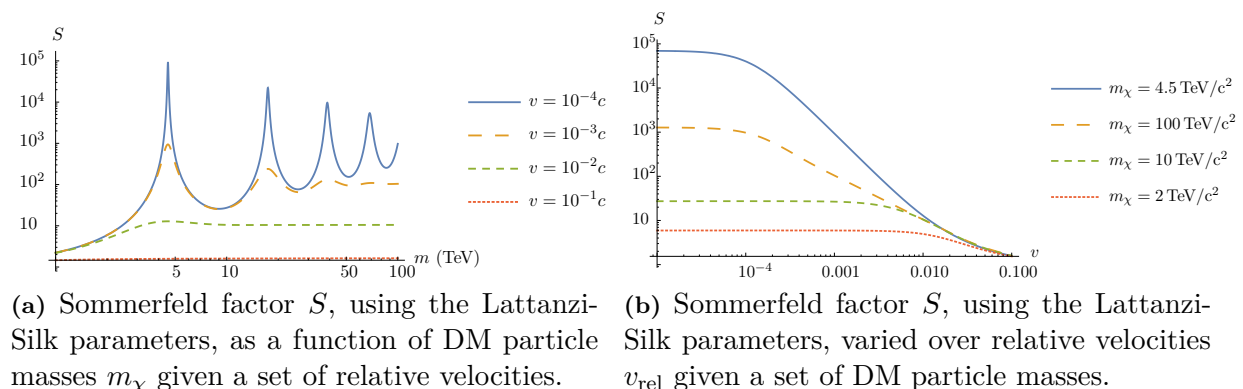


**Figure 8.3:** Sommerfeld enhancement factor varied over DM particle masses  $m_\chi$  and their relative velocities  $v_{\text{rel}}$  with Lattanzi-Silk parameters  $\alpha = 0.03$ ,  $m_\phi = 90 \text{ GeV}/c^2$ . In (a) the enhancement factor is shown to have clear resonance behaviour depending on DM mass  $m_\chi$ . In (b) it is clear that the enhancement factor gets larger with lower relative velocities of the DM particles, although with a different dependence than with Arkani-Hamed parameters. Note that  $S$  with  $m_\chi = 4.5 \text{ TeV}/c^2$  is large because of a resonance peak at that mass.

Regarding the BC at long distances, since the  $C^2$  factor is about constant as seen in the figure, it is not necessary to let  $x \rightarrow \infty$  to compute the Sommerfeld enhancement factor. Instead  $r = 30$  is determined to be large enough, as to compute the Sommerfeld enhancement factor with a large margin, and is hence chosen in future computations.

The enhancement factor as a function of the mass of the DM particle, using the Arkani-Hamed parameters, can be seen in fig. 8.2a for four different relative velocities. From the figure it can be seen that enhancement factor have clear resonance peak at a specific mass regardless of the relative velocity. The enhancement factor, using the Arkani-Hamed parameters, is also plotted as a function of the relative velocity of the colliding DM particles, which is illustrated in fig. 8.2b for four different  $m_\chi$ . As seen in the figure the enhancement factor is larger for small

relative velocities. Both fig. 8.2a and fig. 8.2b are identical to those found in literature [63], thus validating the implementation.

Instead using the Lattanzi-Silk parameters, fig. 8.3a shows the Sommerfeld enhancement as a function of mass of the DM particle for four different relative velocities. From the figure it can be seen that enhancement factor have clear resonance peaks at certain masses regardless of the relative velocity. In fig. 8.3b the Sommerfeld enhancement is shown as a function of relative velocity for four different masses of the DM particle. As seen in the figure the enhancement factor is larger for small relative velocities. Both fig. 8.3a and fig. 8.3b agree with results found in literature [63, 71] further validating the implementation.

## 8.2 Relative velocity distribution

The calculations of the relative velocity distribution in can be significantly simplified using the dimensionless quantities  $x = r/r_0$ ,  $\tilde{v} = v/v_0$  for lengths and velocities respectively. Here,  $r_0$  is the length scale parameter of the density profile and  $v_0 = r_0\sqrt{\rho_0 G}$ , where  $\rho_0$  is the density scale parameter of the density profile and  $G$  is the gravitational constant. A detailed derivation of the results of applying these length and velocity scales is found in appendix B and gives

$$P_{r,\text{rel}}(v_{\text{rel}}) = \frac{2 v_{\text{rel}}^2}{\pi^2 v_0^3 \tilde{\rho}^2(x)} \int_0^\infty d\tilde{v}_{\text{cm}} \tilde{v}_{\text{cm}}^2 \int_0^1 dz \tilde{f} \left( x, \tilde{v}_{\text{cm}}^2 + \frac{\tilde{v}_{\text{rel}}^2}{4} - \tilde{v}_{\text{cm}} \tilde{v}_{\text{rel}} z \right) \\ \times \tilde{f} \left( x, \tilde{v}_{\text{cm}}^2 + \frac{\tilde{v}_{\text{rel}}^2}{4} + \tilde{v}_{\text{cm}} \tilde{v}_{\text{rel}} z \right),$$

where  $\tilde{\rho}(x)$  and  $\tilde{f}(\tilde{\mathcal{E}})$  denotes the dimensionless counterparts of  $\rho(r)$  and  $f(\mathcal{E})$ . The phase-space density  $f(\mathcal{E})$  is calculated through Eddington's formula eq. (5.15), which in its dimensionless form becomes

$$\tilde{f}(\tilde{\mathcal{E}}) = \int_{\tilde{\Psi}^{-1}(\tilde{\mathcal{E}})}^\infty \frac{dx}{\sqrt{\tilde{\mathcal{E}} - \tilde{\Psi}(x)}} \left[ \frac{d\tilde{\rho}}{dx} \frac{d^2\tilde{\Psi}}{dx^2} \left( \frac{d\tilde{\Psi}}{dx} \right)^{-2} - \frac{d^2\tilde{\rho}}{dx^2} \left( \frac{d\tilde{\Psi}}{dx} \right)^{-1} \right],$$

and is shown in figure 8.4a for a cuspy NFW and a cored (1, 3, 0) Zhao density profile respectively. This result corresponds well to the results in [58] where a variation of the same function was calculated.

The relative velocity dispersion  $P_{r,\text{rel}}(v_{\text{rel}})$  for a generic NFW dSph and its cored equivalent  $(\alpha, \beta, \gamma) = (1, 3, 0)$  dSph, with  $\rho_0 = 1.3 \times 10^8 \text{ M}_\odot \text{ kpc}^{-3}$  is shown at three different radii in fig. 8.4b and 8.4c. The calculated distributions agree with the results of similar calculations in [58].

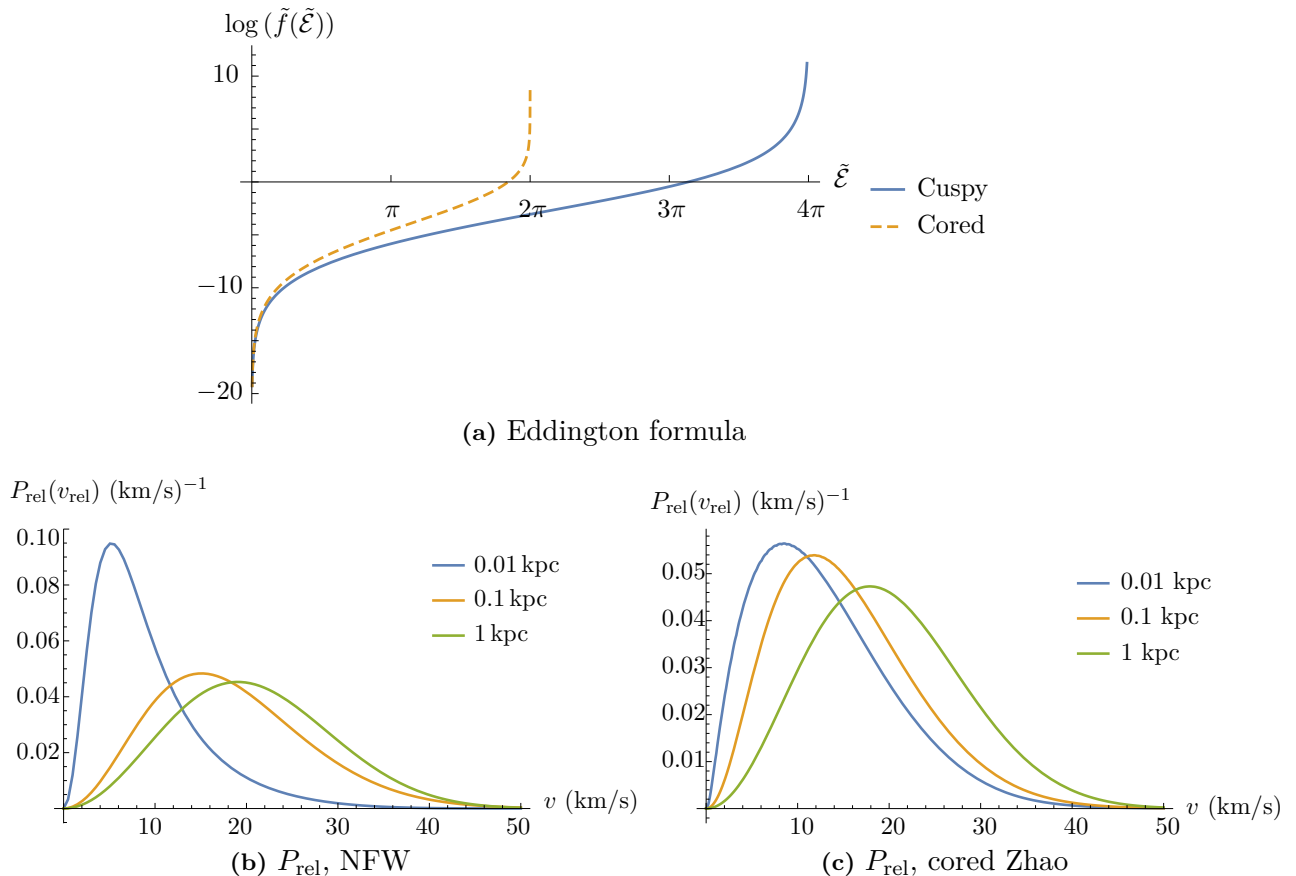


**Figure 8.4:** Shown in the (a) is a numerical calculation of the dimensionless phase-space density  $\tilde{f}(\tilde{\mathcal{E}})$  from the dimensionless Eddington formula, assuming a cuspy NFW (solid line) and a cored Zhao (1, 3, 0) density profile (dashed line) respectively. Note the divergence for both profiles at the maximum value, corresponding to  $\tilde{\mathcal{E}} = \tilde{\Psi}(0)$ . The relative velocity distribution  $P_{\text{rel}}(v_{\text{rel}})$  is shown in (b) and (c) at different radii for a generic dSph with an NFW and a cored Zhao DM density profile respectively, with parameters  $\rho_0 = 1.3 \times 10^8 \text{ M}_{\odot} \text{ kpc}^{-3}$  and  $r_0 = 0.62$ .

### 8.3 Maximisation of likelihood function and calculation of J-factors

The likelihood function was calculated for 20 dSphs according to eq. (7.15) over a large range of parameters  $r_0, v_0$ . In order to compare with literature, the mass  $M_{300}$  enclosed within 300 pc of the dSph centre and the classical J-factor without Sommerfeld enhancement have been calculated for the MLE point. These values are shown for an NFW and a cored Zhao DM density profile respectively, together with data from previous studies in table 8.1. Both evaluations use the Plummer profile for the luminosity density  $\nu(r)$ . Evident from the table is that our MLE:s have a good correspondence to previous results in  $M_{300}$  and largely agrees with previous calculations of  $J$ , although maybe less so than expected.

The  $1\sigma, 2\sigma, 3\sigma$  confidence regions of the likelihood function in the  $r_0, v_0$  parameter space are shown for three dSphs in fig. 9.2, together with contour lines of the unenhanced J-factor and the MLE point. The shapes of the contours largely agrees with what was found by [60], indicating that the likelihood function is largely credible despite the disagreements mentioned above.

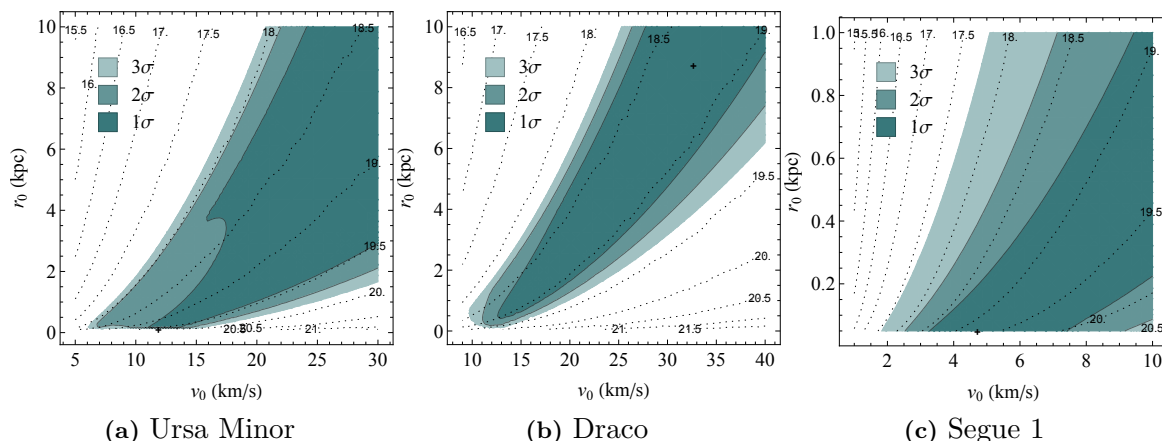


**Figure 8.5:** The likelihood function for different dSphs using the NFW DM density profile and a Plummer profile for the surface brightness. The minimum is marked by a dot and the coloured regions corresponds to deviations  $1\sigma$ ,  $2\sigma$  and  $3\sigma$  respectively. The dashed lines corresponds to constant J factors.

**Table 8.1:** Shown are central masses  $\mathcal{M} = \log_{10} M_{300}$  in  $\log_{10} M_{\odot}$  and J-factors  $\mathcal{J} = \log_{10} J$  without Sommerfeld enhancement in  $\log_{10}(\text{GeV}^2\text{cm}^{-5})$  for 20 dSphs. The central masses in column one are obtained from previous studies [6–8] of dSph kinematics while the second column contain J-factors with  $1\sigma$  error levels as calculated by [59] using an NFW profile. The middle two columns contain  $\mathcal{M}$  as calculated from the MLE obtained in this study using an NFW profile and the connected J-factor with  $1\sigma$  error levels. The last two columns show the same for a cored Zhao profile. Note that the MLE central masses all come within the expected range. Notable is also that 15 of the NFW MLE J-factors of this study have  $1\sigma$  confidence regions that overlap the  $1\sigma$  region given by [59]. Five of them have not, but only Fornax and Sextans differ by an order of magnitude or more.

Dwarf	Previous results		NFW MLE		Cored Zhao MLE	
	$\mathcal{M}$	$\mathcal{J}^{\text{NFW}}$	$\mathcal{M}$	$\mathcal{J}^{\text{NFW}}$	$\mathcal{M}$	$\mathcal{J}^{\text{core}}$
Bootes I	6.0–8.0	$16.82^{+0.55}_{-0.74}$	6.76	$17.92^{+0.62}_{-0.75}$	7.09	$19.34^{+0.44}_{-2.07}$
Leo IV	6.0–8.0	$16.73^{+1.15}_{-0.60}$	6.43	$16.90^{+0.89}_{-0.94}$	6.52	$16.58^{+1.64}_{-0.73}$
Leo T	6.0–8.0	$16.93^{+1.34}_{-0.76}$	7.23	$17.44^{+0.49}_{-0.90}$	7.23	$17.45^{+0.48}_{-0.96}$
Bootes II	6.0–8.0	$18.64^{+0.75}_{-0.47}$	6.74	$18.81^{+1.39}_{-1.03}$	6.63	$18.82^{+1.44}_{-1.10}$
Ursa Major II	6.0–8.0	$19.26^{+0.41}_{-0.38}$	7.52	$19.84^{+0.33}_{-0.35}$	7.73	$20.29^{+0.52}_{-0.81}$
Canes Venatici II	6.0–8.0	$17.83^{+0.36}_{-0.63}$	7.26	$18.47^{+0.34}_{-0.68}$	7.24	$18.53^{+0.38}_{-0.79}$
Hercules	6.0–8.0	$17.33^{+0.35}_{-0.66}$	7.08	$18.12^{+0.28}_{-0.35}$	7.08	$18.00^{+0.34}_{-0.29}$
Ursa Major I	6.0–8.0	$18.03^{+0.34}_{-0.24}$	6.89	$18.24^{+0.97}_{-0.67}$	6.93	$17.84^{+0.75}_{-0.35}$
Willman 1	6.0–8.0	$19.86^{+0.36}_{-0.74}$	7.47	$19.64^{+0.45}_{-0.58}$	7.32	$19.40^{+1.23}_{-0.45}$
Coma Berenices	6.0–8.0	$19.05^{+0.28}_{-0.49}$	7.39	$19.39^{+0.36}_{-0.45}$	7.64	$19.89^{+0.82}_{-0.87}$
Segue 1	6.0–8.0	$19.42^{+0.26}_{-0.39}$	6.55	$19.26^{+0.57}_{-0.46}$	6.83	$19.10^{+0.47}_{-0.30}$
Ursa Minor	6.0–8.0	$18.64^{+0.08}_{-0.22}$	7.42	$19.62^{+0.04}_{-0.25}$	7.41	$19.47^{+0.22}_{-1.07}$
Canes Venatici I	6.0–8.0	$17.33^{+0.16}_{-0.32}$	7.31	$18.01^{+0.25}_{-0.29}$	7.31	$17.87^{+0.22}_{-0.99}$
Leo I	6.0–8.0	$17.73^{+0.17}_{-0.08}$	7.03	$17.66^{+0.27}_{-0.13}$	7.03	$17.53^{+0.22}_{-0.10}$
Draco	6.7–7.5	$18.79^{+0.09}_{-0.16}$	7.19	$18.74^{+0.26}_{-0.28}$	7.01	$18.58^{+0.24}_{-0.15}$
Sextans	6.0–8.0	$17.76^{+0.08}_{-0.06}$	7.25	$18.74^{+0.20}_{-0.20}$	7.23	$18.52^{+0.20}_{-0.30}$
Carina	6.5–7.5	$17.91^{+0.08}_{-0.05}$	6.69	$17.68^{+0.87}_{-0.06}$	6.69	$17.68^{+0.44}_{-0.07}$
Sculptor	6.5–7.4	$18.70^{+0.03}_{-0.04}$	7.40	$18.91^{+0.12}_{-0.13}$	7.33	$18.68^{+0.15}_{-0.21}$
Sagittarius	6.0–8.0	$19.77^{+0.08}_{-0.07}$	7.64	$20.22^{+0.14}_{-0.12}$	7.47	$19.78^{+0.16}_{-0.17}$
Fornax	6.6–7.4	$18.04^{+0.03}_{-0.04}$	7.60	$18.96^{+0.10}_{-0.14}$	7.56	$18.69^{+0.14}_{-0.22}$

## Chapter 9

# Numerical results

The calculated Sommerfeld enhanced  $J_S$ -factors and unenhanced  $J$ -factors of 20 different dSphs are presented in table 9.1, with the notation  $\mathcal{J}_S = \log_{10}(J_S)$  and  $J_S$  in units of  $\text{GeV}^2\text{cm}^{-5}$ . In all calculations the used particle physics parameters are the ones of Arkani-Hamed et al., i.e.  $\alpha = 0.01$  and  $m_\phi = 1 \text{ GeV}/c^2$ , with the DM particle mass set to the suggested value of  $m_\chi = 650 \text{ GeV}/c^2$ . The evaluations make use of the NFW and cored Zhao DM density profiles. Notably, the Sommerfeld enhanced  $J_S$ -factors are often four orders of magnitude larger than their unenhanced counterparts while the  $J_{S(v^*)}$ -factors are about one to two orders of magnitude greater than the  $J_{S(v^*)}$ -factors.

Earlier research [72] have approximated the  $J_S$  factors by simply multiplying  $J$  with the Sommerfeld enhancement factor at typical speeds. In order to evaluate the impact of including the Sommerfeld enhancement factor explicitly, as opposed to using a constant reference value, we present results with this approximation denoted  $\mathcal{J}_{S(v^*)} = \log_{10}(S(v^*)J)$  as well. The values of  $\mathcal{J}_{S(v^*)}$  are found in table 9.1. For this calculation the typical relative velocity of  $v^* = 10^{-5}c$  is used. As seen in the table there is a clear difference in magnitude of the  $J_S$  and  $J_{S(v^*)}$  values for both the NFW and cored Zhao profiles, although this may be an artifact of the specific chosen DM mass. In the table it is also clear that the uncertainty in the  $\mathcal{J}_S$  and  $\mathcal{J}_{S(v^*)}$  values tend to decrease for galaxies with a larger number of stars in the data set, for both the NFW and cored Zhao profile, as expected of a statistical method.

Focusing on one of the larger dSphs, the Sculptor galaxy, the modified mass ratio  $\epsilon_\phi = m_\phi/(\alpha m_\chi)$ 's impact on  $\mathcal{J}_S$  and  $\mathcal{J}_{S(v^*)}$  are studied in more detail. Fig. 9.1 displays a comparison between the  $\mathcal{J}_S$ - and  $\mathcal{J}_{S(v^*)}$ -factors over a range of  $\epsilon_\phi$  from  $10^{-3}$  to 100. As seen in the figure, the main difference between the values of  $\mathcal{J}_S$  and  $\mathcal{J}_{S(v^*)}$  for both NFW and cored Zhao, is an increase in the amplitude of the oscillations for the  $\mathcal{J}_S$ -factor. However, the main difference between the NFW and cored Zhao profiles is a vertical shift while the overall shape and the behaviour of the oscillations are close to identical. It should be noted that the oscillations found in  $\mathcal{J}_S$  and  $\mathcal{J}_{S(v^*)}$  imply that a different choice of DM mass in the calculations presented in table 9.1 may significantly change the presented  $\mathcal{J}_S$  and  $\mathcal{J}_{S(v^*)}$ .

The likelihood function with confidence levels around the minimum in the  $r_0, v_0$  parameter space for the dwarf Sculptor, using cuspy and cored density profiles, can be seen in fig. 9.2. The figure also show the binned likelihood  $-\log(L/L_{\max})$  over  $\mathcal{J}$  and  $\mathcal{J}_S$  with confidence intervals. From the figure it can be seen that Sculptor have a closed  $1\sigma$  curve, in the  $r_0, v_0$  plane, which is a desirable property for the analysis. The likelihood over the  $\mathcal{J}$ - and  $\mathcal{J}_S$ -factors have, as seen in the figure, a closed  $1\sigma$  levels over a small interval. The Sculptor dwarf is a pleasant example of our likelihood analysis for all 20 dSphs. Plots of the other 19 dSphs can be found in appendix D.

**Table 9.1:** Computed  $\mathcal{J}$ ,  $\mathcal{J}_S$ , and  $\mathcal{J}_{S(v^*)}$  factors for each of the considered dSph for both the NFW and the cored Zhao profiles. The calculations of the Sommerfeld enhanced  $J$ -factors make use of the Arkani-Hamed parameters  $\alpha = 0.01$  and  $m_\phi = 1 \text{ GeV}/c^2$  with  $m_\chi = 650 \text{ GeV}/c^2$ . A typical relative velocity of  $v^* = 10^{-5}c$  is used for the  $\mathcal{J}_{S(v^*)}$  factor calculations.  $N$  is the number of stars in the data set. As seen the uncertainty the computed factors tend to decrease with increasing  $N$  as is expected with a statistical method. There is also a clear difference in magnitude between the different flavours of  $J$ -factors for both the NFW and the cored Zhao profile. Specifically,  $\mathcal{J}_S$  is often four orders of magnitude larger than the original  $J$ , while  $\mathcal{J}_{S(v^*)}$  seem to give an overestimation compared to  $J_S$  of one to two orders of magnitude for most galaxies. As shown here,  $\mathcal{J}_S$  and  $\mathcal{J}_{S(v^*)}$  are in units of  $\log_{10} \text{ GeV}^2 \text{ cm}^{-5}$ .

Dwarf	$N$	NFW			Cored Zhao		
		$\mathcal{J}$	$\mathcal{J}_{S(v^*)}$	$\mathcal{J}_S$	$\mathcal{J}$	$\mathcal{J}_{S(v^*)}$	$\mathcal{J}_S$
Bootes I	14	$17.92^{+0.62}_{-0.75}$	22.65	$21.79^{+0.49}_{-0.36}$	$19.34^{+0.44}_{-2.07}$	24.07	$21.86^{+0.42}_{-0.48}$
Leo IV	17	$16.90^{+0.89}_{-0.94}$	21.63	$21.31^{+0.65}_{-0.85}$	$16.58^{+1.64}_{-0.73}$	21.31	$20.87^{+0.55}_{-0.56}$
Leo T	19	$17.44^{+0.49}_{-0.90}$	22.17	$21.37^{+0.34}_{-0.85}$	$17.45^{+0.48}_{-0.96}$	22.18	$21.27^{+0.29}_{-0.82}$
Bootes II	20	$18.81^{+1.39}_{-1.03}$	23.54	$23.05^{+1.16}_{-1.07}$	$18.82^{+1.44}_{-1.10}$	23.55	$23.01^{+0.90}_{-0.89}$
Ursa Major II	20	$19.84^{+0.33}_{-0.35}$	24.57	$23.22^{+0.61}_{-0.31}$	$20.29^{+0.52}_{-0.81}$	25.02	$23.10^{+0.47}_{-0.47}$
Canes Venatici II	25	$18.47^{+0.34}_{-0.68}$	23.20	$21.74^{+0.28}_{-0.30}$	$18.53^{+0.38}_{-0.79}$	23.26	$21.73^{+0.38}_{-0.42}$
Hercules	30	$18.12^{+0.28}_{-0.35}$	22.85	$22.16^{+0.30}_{-0.32}$	$18.00^{+0.34}_{-0.29}$	22.73	$21.94^{+0.27}_{-0.24}$
Ursa Major I	39	$18.24^{+0.97}_{-0.67}$	22.97	$22.40^{+0.63}_{-0.84}$	$17.84^{+0.75}_{-0.35}$	22.57	$21.88^{+0.47}_{-0.41}$
Willman 1	45	$19.64^{+0.45}_{-0.58}$	24.37	$22.95^{+0.60}_{-0.22}$	$19.40^{+1.23}_{-0.45}$	24.13	$23.14^{+0.34}_{-0.16}$
Coma Berenices	59	$19.39^{+0.36}_{-0.45}$	24.12	$22.89^{+0.27}_{-0.35}$	$19.89^{+0.82}_{-0.87}$	24.62	$23.00^{+0.17}_{-0.30}$
Segue 1	66	$19.26^{+0.57}_{-0.46}$	23.99	$23.58^{+0.40}_{-0.46}$	$19.10^{+0.47}_{-0.30}$	23.83	$23.22^{+0.29}_{-0.20}$
Ursa Minor	196	$19.62^{+0.04}_{-0.25}$	24.35	$23.41^{+0.00}_{-0.31}$	$19.47^{+0.22}_{-1.07}$	24.20	$23.14^{+0.19}_{-1.48}$
Canes Venatici I	214	$18.01^{+0.25}_{-0.29}$	22.74	$21.86^{+0.29}_{-0.33}$	$17.87^{+0.22}_{-0.99}$	22.60	$21.61^{+0.19}_{-1.09}$
Leo I	328	$17.66^{+0.27}_{-0.13}$	22.39	$21.11^{+0.45}_{-0.17}$	$17.53^{+0.22}_{-0.10}$	22.26	$21.06^{+0.29}_{-0.04}$
Draco	353	$18.74^{+0.26}_{-0.28}$	23.47	$22.10^{+0.51}_{-0.19}$	$18.58^{+0.24}_{-0.15}$	23.31	$21.92^{+0.38}_{-0.12}$
Sextans	424	$18.74^{+0.20}_{-0.20}$	23.47	$22.64^{+0.20}_{-0.20}$	$18.52^{+0.20}_{-0.30}$	23.24	$22.31^{+0.19}_{-0.30}$
Carina	758	$17.68^{+0.87}_{-0.06}$	22.41	$21.46^{+1.03}_{-0.08}$	$17.68^{+0.44}_{-0.07}$	22.41	$21.47^{+0.49}_{-0.05}$
Sculptor	1352	$18.91^{+0.12}_{-0.13}$	23.64	$22.63^{+0.12}_{-0.15}$	$18.68^{+0.15}_{-0.21}$	23.41	$22.28^{+0.16}_{-0.24}$
Sagittarius	1373	$20.22^{+0.14}_{-0.12}$	24.95	$23.68^{+0.11}_{-0.08}$	$19.78^{+0.16}_{-0.17}$	24.51	$23.04^{+0.16}_{-0.17}$
Fornax	2409	$18.96^{+0.10}_{-0.14}$	23.69	$22.59^{+0.09}_{-0.13}$	$18.69^{+0.14}_{-0.22}$	23.42	$22.19^{+0.12}_{-0.19}$

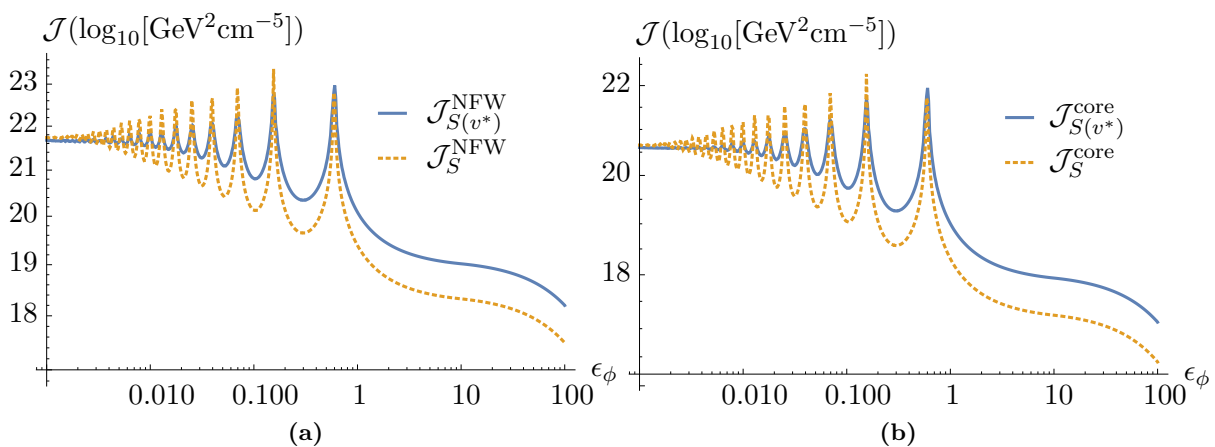


**Figure 9.1:**  $\mathcal{J}_S$ -factors for the Sculptor galaxy over a range of  $\epsilon_\phi$  from  $10^{-3}$  to 100. The  $\mathcal{J}_S$  factors are compared against  $\mathcal{J}_{S(v^*)} = \log_{10}(S(v^*)J)$  for the typical relative velocity of  $v^* = 10^{-5}c$ . Fig. (a) uses the NFW density profile while fig. (b) uses the cored Zhao profile. A clear difference between the calculated  $\mathcal{J}_S$  value and that of  $\mathcal{J}_{S(v^*)}$ , for both the NFW and cored Zhao density profiles, is the amplitude of the oscillations are greater for  $\mathcal{J}_S$ . Meanwhile the main difference between the NFW and the cored Zhao profile are in a constant vertical shift while the overall shape and the behaviour of the oscillations remain largely the same. The calculations uses  $\alpha = 0.01$  and  $m_\phi = 1 \text{ GeV}/c^2$  as in the Arkani-Hamed et al. parameter profile [55].

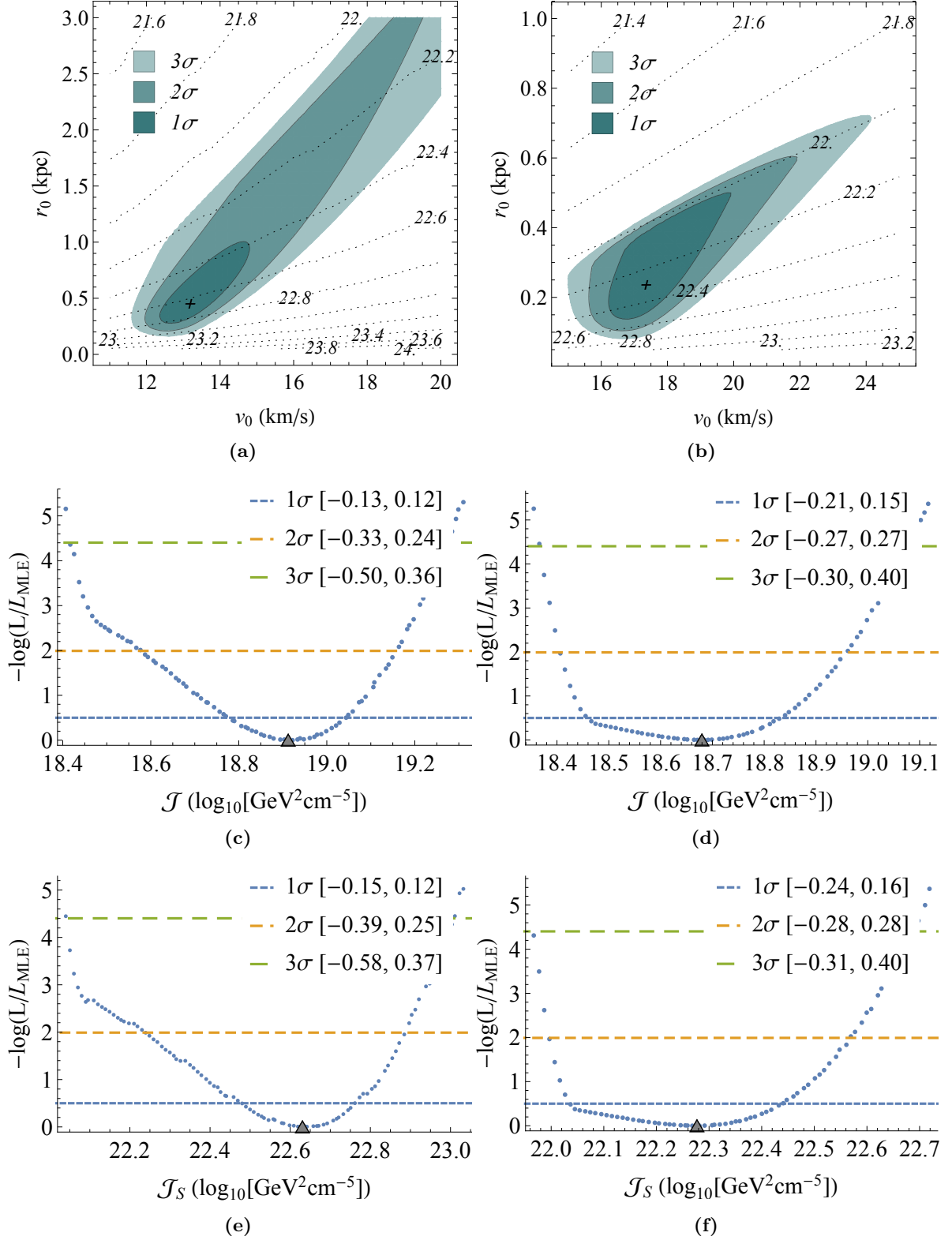


**Figure 9.2:** All figures show calculated likelihood functions for the Sculptor dSph. In the left column a cuspy NFW DM distribution have been used to model the dSph, while in the right column a cored Zhao profile have been used. Shown in (a) and (b) is the likelihood function in the  $r_0, v_0$  parameter space, with the MLE marked with a plus sign. The coloured regions correspond to evaluated 1 $\sigma$ , 2 $\sigma$  and 3 $\sigma$  confidence levels respectively and the dotted lines correspond to contours of constant  $\mathcal{J}_S$ . The binned likelihood  $-\log(L/L_{\text{MLE}})$  with corresponding standard deviations is plotted in (c) and (d) for  $\mathcal{J}$  and in (e) and (f) for  $\mathcal{J}_S$ .

# Chapter 10

## Conclusion

In this thesis we have constructed a model for and successfully extracted Sommerfeld enhanced  $J$ -factors for 20 dSphs using theoretical concepts from Newtonian galactic dynamics and non-relativistic quantum mechanics as well as a frequentist analysis of star velocity data. The  $J$ -factor has been evaluated with a model of DM phase space distributions and gravitational potentials assuming spherically symmetric systems with isotropic velocity distributions. The input particle physics parameters in the Sommerfeld enhancement is taken to be that of the commonly used Arkani-Hamed et al. profile. The likelihood estimation has been performed assuming a gaussian, radially dependent, velocity dispersion of the dSphs.

The main difference compared to previous research is the inclusion of a velocity-dependent Sommerfeld enhancement with a suitable velocity distribution. This provides us with higher precision  $J$ -factors in relation to self-interactions than previously calculated, and may have important implications to indirect DM searches. Previous research has also tended to focus mostly on the cuspy NFW profile, even though it has generally been proven a bad fit for real DM distributions in dSphs. However, in order to allow for comparison with previous results, we chose to perform  $J$ -factor calculations with an NFW profile in addition to the more realistic cored Zhao profile.

In order to enable the inclusion of the Sommerfeld enhancement in the  $J$ -factor, a modification to the statistical method used in [59] was needed. A consequence of including Sommerfeld enhancement was that it was no longer possible to express the likelihood function directly in terms of  $J$ , since doing so would create a circular dependence. Instead a binned likelihood function was constructed by first calculating  $J$  over a grid in the  $r_0, v_0$  parameter space. The points were then divided into bins of equal size over the range of the calculated  $J$ -factors, for each bin selecting only the point with maximum likelihood. The application of the binned likelihood method was largely successful, although it induced a difficult compromise between grid density and computing power. This can be seen in some of the binned likelihood plots in appendix D.2, where the grid has clearly been too sparse to give a continuous likelihood function.

As noted in the results chapter we have shown that the inclusion of the Sommerfeld enhancement into the  $J$ -factor boosts the value of the dSph  $J$ -factors with up to four orders of magnitude for the selected DM particle parameters. Our results also indicate a difference of about an order of magnitude between using a constant reference value of the Sommerfeld enhancement  $S$  as opposed to including  $S$  explicitly by letting  $S$  depend on the relative velocity. This stresses the importance of including the Sommerfeld enhancement explicitly.

The Sommerfeld enhancement has been observed to oscillate heavily with the DM mass. These oscillations make the values of the  $J$ -factors very specific to the chosen DM mass. The overall shape of the  $\mathcal{J}_S$ -factors over the range of the modified mass ratio  $\epsilon_\phi$  agrees with that of [60], providing verification of the results.

As noted in chapter 8, our  $J$ -factors had a  $1\sigma$  overlap with earlier research [59] for 75% of the galaxies, indicating that our statistical method is valid. Our confidence intervals are, however, slightly larger than the ones of [59], which might be a consequence of the modification in the statistical method required to incorporate Sommerfeld enhancement.

In February this year, a report covering similar topics to the ones discussed in this thesis appeared on arXiv [60]. This article proved a valuable resource to compare our results with.

However, while the article calculates Sommerfeld enhanced  $J$ -factors, there are several important differences. The primary difference is that an exact Sommerfeld enhancement factor is used in this thesis, while they use an analytic approximation. Furthermore, a different statistical method is used, as well as a different set of galaxies, and we use a cored profile in addition to the NFW one.

Topics for future study would include investigating the larger confidence intervals found with our modified statistical method in more detail. Another important improvement could result from a more careful consideration of the used  $r_0$ ,  $v_0$  and  $r_*$  parameter limits, since these has proven to significantly impact the constructed likelihood and resulting confidence regions in  $J$  considerably. In addition, there is a plethora of directions to explore in relation to the determination of  $J$ -factors. Including, for example, opening up the parameters of the density profiles as nuisance parameters for the likelihood function, assuming non-spherical or anisotropic systems, or investigating other DM particle parameters.

Hopefully, this thesis has provided an interesting insight into several aspects of the ongoing search for DM. This project brought us to the edge of current indirect detection DM research over the course of a semester, and has been a truly rewarding journey.

# Bibliography

- [1] European Southern Observatory, *Sculptor dwarf galaxy*, (2015) <http://www.eso.org/public/images/eso1536a/>.
- [2] D. N. Spergel, *Dark matter*, (Mar. 2017) <http://accessscience.com/content/dark-matter/800520>.
- [3] M. S. Seigar, *Dark Matter in the Universe*, 2053-2571 (Morgan & Claypool Publishers, 2015).
- [4] J. Binney and S. Tremaine, *Galactic dynamics, 2nd edition*, 2nd ed. (Princeton University Press, 2008).
- [5] B. H. B. Opitz, “Searches for dark matter self-annihilation signals from dwarf spheroidal galaxies and the Fornax galaxy cluster with imaging air Cherenkov telescopes”, PhD thesis (U. Hamburg, Dept. Phys., 2014).
- [6] S. E. Koposov et al., “Accurate stellar kinematics at faint magnitudes: application to the boötes i dwarf spheroidal galaxy”, *The Astrophysical Journal* **736**, 146 (2011).
- [7] M. G. Walker et al., “A universal mass profile for dwarf spheroidal galaxies?”, *The Astrophysical Journal* **704**, 1274 (2009).
- [8] J. D. Simon and M. Geha, “The kinematics of the ultra-faint milky way satellites: solving the missing satellite problem”, *The Astrophysical Journal* **670**, 313 (2007).
- [9] M. Roos, “Dark Matter: The evidence from astronomy, astrophysics and cosmology”, *arXiv*, 25 (2010).
- [10] G. Bertone, D. Hooper, and J. Silk, “Particle dark matter: Evidence, candidates and constraints”, *Physics Reports* **405**, 279 (2005).
- [11] K. Freese, “Review of Observational Evidence for Dark Matter in the Universe and in upcoming searches for Dark Stars”, *arXiv.org astro-ph*, 1 (2008).
- [12] J. M. Gaskins, “A review of indirect searches for particle dark matter”, *Contemp. Phys.* **57**, 496 (2016).
- [13] V. C. Rubin, W. K. Ford, Jr., and N. Thonnard, “Rotational properties of 21 SC galaxies with a large range of luminosities and radii, from NGC 4605 /R = 4kpc/ to UGC 2885 /R = 122 kpc/”, **238**, 471 (1980).
- [14] K. G. Begeman, A. H. Broeils, and R. H. Sanders, “Extended rotation curves of spiral galaxies: Dark haloes and modified dynamics”, *Mon. Not. Roy. Astron. Soc.* **249**, 523 (1991).
- [15] R. Massey, T. Kitching, and J. Richard, “The dark matter of gravitational lensing”, *Reports on Progress in Physics* **73**, 086901 (2010).
- [16] G. Battaglia et al., “The radial velocity dispersion profile of the Galactic halo: Constraining the density profile of the dark halo of the Milky Way”, *Monthly Notices of the Royal Astronomical Society* **364**, 433 (2005).
- [17] D. Larson et al., “Seven-Year Wilkinson Microwave Anisotropy Probe (WMAP) Observations: Power Spectra and WMAP-Derived Parameters”, *eprint arXiv* **1001**, 4635 (2010).
- [18] E. Komatsu et al., “Seven-Year Wilkinson Microwave Anisotropy Probe (Wmap1) Observations: Cosmological Interpretation”, *arXiv astro-ph.C*, 330 (2010).
- [19] D. J. Thompson, D. L. Bertsch, and R. H. O ’neal, “The Highest-Energy Photons Seen by the Energetic Gamma Ray Experiment Telescope (EGRET) on the Compton Gamma Ray Observatory”, (2004).
- [20] A. W. Strong et al., “Gamma-ray continuum emission from the inner Galactic region as observed with INTEGRAL/SPI”, *Astronomy and Astrophysics* **444**, 495 (2005).

- 
- [21] L. Goodenough and D. Hooper, “Possible Evidence For Dark Matter Annihilation In The Inner Milky Way From The Fermi Gamma Ray Space Telescope”, (2009).
- [22] V. Vitale, A. Morselli, and for the Fermi/LAT Collaboration, “Indirect Search for Dark Matter from the center of the Milky Way with the Fermi-Large Area Telescope”, ArXiv e-prints (2009).
- [23] R. Bartels, S. Krishnamurthy, and C. Weniger, “Strong Support for the Millisecond Pulsar Origin of the Galactic Center GeV Excess”, *Physical Review Letters* **116**, 1 (2016).
- [24] E. Charles et al., “Sensitivity projections for dark matter searches with the Fermi large area telescope”, *Physics Reports* **636**, 1 (2016).
- [25] M. Aguilar et al., “First result from the alpha magnetic spectrometer on the international space station: precision measurement of the positron fraction in primary cosmic rays of 0.5350 gev”, *Phys. Rev. Lett.* **110**, 141102 (2013).
- [26] A.-0. Collaboration, “Cosmic-ray positron fraction measurement from 1 to 30 {GeV} with {AMS-01}”, *Physics Letters B* **646**, 145 (2007).
- [27] S. W. Barwick et al., “Measurements of the Cosmic-Ray Positron Fraction from 1 to 50 GeV”, *The Astrophysical Journal* **482**, L191 (1997).
- [28] J. J. Beatty et al., “New measurement of the cosmic-ray positron fraction from 5 to 15 GeV”, *Physical Review Letters* **93**, 1 (2004).
- [29] E. A. Baltz, J. Edsjo, K. Freese, and P. Gondolo, “The Cosmic ray positron excess and neutralino dark matter”, *Phys. Rev.* **D65**, 063511 (2002).
- [30] D. P. Finkbeiner, “Microwave ISM Emission Observed by WMAP”, *Astrophys. J.* **614**, 186 (2004).
- [31] G. Dobler and D. P. Finkbeiner, “Extended Anomalous Foreground Emission in the WMAP 3-Year Data”, 1 (2007).
- [32] M. Dworknik, Z. Keresztes, and L. Á. Gergely, “Modified gravity theories and dark matter models tested by galactic rotation curves”, *Springer Proc. Phys.* **157**, 427 (2014).
- [33] T. D. Brandt, “Constraints on macho dark matter from compact stellar systems in ultra-faint dwarf galaxies”, *The Astrophysical Journal Letters* **824**, L31 (2016).
- [34] C. Alcock et al., “The MACHO project: Microlensing results from 5.7 years of LMC observations”, *Astrophys. J.* **542**, 281 (2000).
- [35] R. D. Peccei, “The Strong CP problem and axions”, *Lect. Notes Phys.* **741**, [3(2006)], 3 (2008).
- [36] M. S. Turner, “Dark matter in the universe”, *Physica Scripta* **1991**, 167 (1991).
- [37] G. Jungman, M. Kamionkowski, and K. Griest, “Supersymmetric dark matter”, *Physics Reports* **267**, 195 (1996).
- [38] S. W. Randall et al., “Constraints on the Self-Interaction Cross-Section of Dark Matter from Numerical Simulations of the Merging Galaxy Cluster 1E 0657-56”, *Astrophys. J.* **679**, 1173 (2008).
- [39] D. Harvey et al., “The non-gravitational interactions of dark matter in colliding galaxy clusters”, *Science* **347**, 1462 (2015).
- [40] L. Wang, R. R. Caldwell, J. P. Ostriker, and P. J. Steinhardt, “Cosmic Concordance and Quintessence”, *The Astrophysical Journal* **530**, 17 (2000).
- [41] B. D. Wandelt et al., “Self-Interacting Dark Matter”, 1 (2000).
- [42] J. F. Navarro, C. S. Frenk, and S. D. M. White, “The Structure of Cold Dark Matter Halos”, *The Astrophysical Journal* **462**, 563 (1996).
- [43] Y. Jing, “The density profile of equilibrium and nonequilibrium dark matter halos”, *The Astrophysical Journal* **535**, 30 (2000).
- [44] B. Moore et al., “Resolving the structure of cold dark matter halos”, *Astrophys. J.* **499**, L5 (1998).

- [45] W. J. G. de Blok, S. S. McGaugh, A. Bosma, and V. C. Rubin, “Mass density profiles of LSB galaxies”, *Astrophys. J.* **552**, L23 (2001).
- [46] V. P. Debattista and J. A. Sellwood, “Dynamical friction and the distribution of dark matter in barred galaxies”, *Astrophys. J.* **493**, L5 (1998).
- [47] D. N. Spergel and P. J. Steinhardt, “Observational evidence for selfinteracting cold dark matter”, *Phys. Rev. Lett.* **84**, 3760 (2000).
- [48] A. Kamada, M. Kaplinghat, A. B. Pace, and H.-B. Yu, “How the Self-Interacting Dark Matter Model Explains the Diverse Galactic Rotation Curves”, (2016).
- [49] T. M. Undagoitia and L. Rauch, “Dark matter direct-detection experiments”, *Journal of Physics G: Nuclear and Particle Physics* **43**, 013001 (2016).
- [50] E. A. Baltz et al., “Pre-launch estimates for GLAST sensitivity to Dark Matter annihilation signals”, *Journal of Cosmology and Astroparticle Physics* **2008**, 013 (2008).
- [51] J. Miralda-Escudé, “A test of the collisional dark matter hypothesis from cluster lensing”, *The Astrophysical Journal* **564**, 60 (2002).
- [52] N. Yoshida, V. Springel, S. D. M. White, and G. Tormen, “Collisional dark matter and the structure of dark halos”, *Astrophys. J.* **535**, L103 (2000).
- [53] G. A. Dooley et al., “Enhanced tidal stripping of satellites in the galactic halo from dark matter self-interactions”, **461**, 710 (2016).
- [54] J. Zavala, M. Vogelsberger, and M. G. Walker, “Constraining Self-Interacting Dark Matter with the Milky Way’s dwarf spheroidals”, **6**, 1 (2012).
- [55] Arkani-Hamed, N. et al, “A Theory of Dark Matter”, 1 (2008).
- [56] I. Cholis et al., “High Energy Positrons From Annihilating Dark Matter”, *Phys. Rev.* **D80**, 123511 (2009).
- [57] A. Loeb and N. Weiner, “Cores in Dwarf Galaxies from Dark Matter with a Yukawa Potential”, (2010) [10.1103/PhysRevLett.106.171302](https://arxiv.org/abs/10.1103/PhysRevLett.106.171302).
- [58] F. Ferrer and D. R. Hunter, “The impact of the phase-space density on the indirect detection of dark matter”, (2013) [10.1088/1475-7516/2013/09/005](https://arxiv.org/abs/10.1088/1475-7516/2013/09/005).
- [59] A. Chiappo et al., “Dwarf spheroidal J-factors without priors: A likelihood-based analysis for indirect dark matter searches”, *Monthly Notices of the Royal Astronomical Society* **466**, 669 (2017).
- [60] K. K. Boddy, J. Kumar, L. E. Strigari, and M.-Y. Wang, “Sommerfeld-Enhanced  $J$ -Factors For Dwarf Spheroidal Galaxies”, 1 (2017).
- [61] J. Schwinger, *Quantum Mechanics - Symbolism of Atomic Measurements*, edited by Berthold-Georg Englert (Springer, 2001).
- [62] R. Iengo, “Sommerfeld enhancement: general results from field theory diagrams”, (2009).
- [63] B. Robertson and A. Zentner, “Dark Matter Annihilation Rates with Velocity-Dependent Annihilation Cross Sections”, 1 (2009).
- [64] A. Burkert, “The Structure and Dark Halo Core Properties of Dwarf Spheroidal Galaxies”, (2015).
- [65] J. Binney and S. Tremaine, *Galactic dynamics* (Princeton University Press, 1987).
- [66] G. B. Arfken, H.-J. Weber, F. E. Harris, and S. (-b. collection), *Mathematical methods for physicists: a comprehensive guide*, English, 7th (Elsevier, Amsterdam;Boston, 2013).
- [67] H. Zhao, “Analytical models for galactic nuclei”, **278**, 488 (1996).
- [68] H. C. Plummer, “On the problem of distribution in globular star clusters”, **71**, 460 (1911).
- [69] Y. Pawitan, *In all likelihood: statistical modelling and inference using likelihood*, English (Oxford University Press, Oxford, 2013).
- [70] M. Lattanzi and J. Silk, “Can the WIMP annihilation boost factor be boosted by the Sommerfeld enhancement?”, *Physical Review D - Particles, Fields, Gravitation and Cosmology* (2009) [10.1103/PhysRevD.79.083523](https://arxiv.org/abs/10.1103/PhysRevD.79.083523).

- [71] L. Pieri, M. Lattanzi, and J. Silk, “Constraining the dark matter annihilation cross-section with Cherenkov telescope observations of dwarf galaxies”, **399**, 2033 (2009).
- [72] M.-H. Chan, “Does the gamma-ray signal from the central milky way indicate sommerfeld enhancement of dark matter annihilation”, *Research in astronomy and astrophysics* **16**, 116 (2016).
- [73] G. Steigman, B. Dasgupta, and J. F. Beacom, “Precise relic WIMP abundance and its impact on searches for dark matter annihilation”, *Physical Review D - Particles, Fields, Gravitation and Cosmology* **86**, 1 (2012).

## Appendix A

# The unenhanced cross section

To complete the analysis on the annihilation cross section  $\sigma = \sigma_0 S(v_{\text{rel}})$ , the unenhanced cross section  $\sigma_0$  is determined by using the derived formula for thermal relic abundance (2.2) in section 1, and matching this with the WMAP-7 inferred result. The 7-year data from WMAP have estimated the thermal relic abundance of DM to a mean value of  $\Omega_\chi h^2 = 0.1120 \pm 0.0056$  [18]. Thus eq. (2.2), repeated here for convenience, is equal to

$$\Omega_\chi h^2 \approx \frac{3 \cdot 10^{-27} \text{ cm}^3/\text{sec}}{\overline{\sigma_0 v_{\text{rel}}}} = 0.1120 \pm 0.0056, \quad (\text{A.1})$$

which gives us the thermally averaged annihilation rate factor  $\overline{\sigma_0 v_{\text{rel}}} \approx 3 \cdot 10^{-26} \text{ cm}^3/\text{sec}$ . The formula of eq. (A.1) can be derived using the Boltzmann equation for the DM number density and some approximations as in [37], which we will review below.

In the thermal equilibrium of the early universe, the number density of DM particles  $\chi$  is

$$n_\chi^{\text{eq}} = \frac{g}{(2\pi)^2} \int f(\epsilon) d\epsilon, \quad (\text{A.2})$$

where  $g$  is the degeneracy, or the number of internal degrees of freedom, of the particle  $\chi$  and  $f(\mathbf{p})$  is the familiar Fermi-Dirac or Bose-Einstein distribution depending of the particle type. At high temperatures  $k_B T \gg mc^2$ , or  $T \gg m$  in natural units  $\hbar = c = k_B = 1$ , then the number density is proportional to  $T$  via  $n_\chi^{\text{eq}} \propto T^3$ . At low temperatures  $k_B T \ll mc^2$  then the number density will be Boltzmann repressed as  $n_\chi^{\text{eq}} \simeq g(m_\chi T/2\pi)^{3/2} e^{-m_\chi/T}$ . As mentioned in section 2, if the expansion of the universe was isothermal, or so slow that thermal equilibrium was always maintained, the number of DM particles would decrease exponentially, leaving them extinct today.

During the early thermal equilibrium at high temperatures, DM particles  $\chi$  annihilated into lighter baryonic ones  $b$  through  $\chi\bar{\chi} \leftrightarrow b\bar{b}$  and vice versa. Shortly after the thermal energy drops below the rest energy of the particle, or  $T \ll m$ , the number density begins to drop exponentially. The rate of annihilation  $\Gamma = \overline{\sigma_0 v_{\text{rel}}} n_\chi$ , same as the one used in section 3, drops below the expansion rate of the universe causing the  $\chi$ 's to cease to annihilate. When the annihilation reaction  $\chi\bar{\chi} \leftrightarrow b\bar{b}$  ceases, the DM particles  $\chi$  are said to fall out of equilibrium, leaving a cosmological relic abundance that can be measured today. This simple picture can be modelled by the Boltzmann equation, to describe the time evolution of the number density  $n_\chi(t)$ ;

$$\frac{dn_\chi}{dt} + 3Hn_\chi = -\overline{\sigma_0 v_{\text{rel}}} [(n_\chi)^2 - (n_\chi^{\text{eq}})^2], \quad (\text{A.3})$$

where  $H$  is the Hubble expansion rate. The term  $3Hn_\chi$  accounts for the expansion of the universe. No closed-form solution analytic solution exist to eq. (A.3), although there exist a fairly simple approximation.

The early universe was very radiation dominated, and the Hubble expansion rate falls with temperature as

$$H(T) = \frac{1.66\sqrt{g_*}T^2}{m_{Pl}}, \quad (\text{A.4})$$

where  $g_*$  is the effective number of relative degrees of freedom, and  $m_{PI} \simeq 10^{19}$  GeV is the Planck mass. At early times when  $T \gg m_\chi$  then  $H \propto T^2$ , since  $n_\chi \propto T^3$ , the expansion rate decreases slower than the annihilation rate. In fact, at very early times, the Hubble expansion term  $3Hn_\chi$  is negligible in eq. (A.3). Although at late times, the right-hand side in eq. (A.3) becomes negligible, and the DM number energy becomes constant. Tending to the entropy changes in the universe at this time, we have that the number density  $n_\chi$  in terms of the entropy density  $s = 0.4g_*T^3$  is constant, that is,  $n_\chi/s$  will remain constant. Since the entropy per comoving volume<sup>1</sup> does not change with time, then  $(n_\chi/s)_0 = (n_\chi/s)_f$  where subscript 0 denotes the present entropy density of the universe and  $f$  the corresponding value at freezeout. The temperature  $T_f$  at freezeout is  $T_f \simeq m_\chi/20$ , which is obtained by solving  $\Gamma(T_f) = H(T_f)$  with typical weak scale interaction numbers.

By using eq. (A.4) and the rate freezeout condition  $\Gamma = n_\chi \overline{\sigma_0 v_{\text{rel}}} = H$ , we have that

$$\left(\frac{n_\chi}{s}\right)_0 = \left(\frac{n_\chi}{s}\right)_f \simeq \frac{100}{m_\chi m_{PI} \sqrt{g_*} \cdot \overline{\sigma_0 v_{\text{rel}}}} \quad (\text{A.5})$$

$$\simeq \frac{10^{-8}}{(m_\chi/\text{GeV})(\overline{\sigma_0 v_{\text{rel}}}/10^{-27} \text{cm}^3 \text{s}^{-1})}. \quad (\text{A.6})$$

Since the current entropy density has a value of  $s_0 = 4000 \text{ cm}^{-3}$  and the critical density  $\rho_c = 3H_0^2/8\pi G \simeq 10^{-5} h^2 \text{ GeV/cm}^3$ , the present mass density in units of the critical density  $\Omega_\chi = \rho_\chi/\rho_c$  is

$$\Omega h^2 \simeq \frac{3 \cdot 10^{-27} \text{ cm}^3 \text{ s}^{-1}}{\overline{\sigma_0 v_{\text{rel}}}}. \quad (\text{A.7})$$

Taken together with the computed value of  $\Omega h^2 = 0.1120 \pm 0.0056$  from WMAP data, the approximate velocity average annihilation rate factor without Sommerfeld enhancement is  $3 \cdot 10^{-26} \text{ cm}^3/\text{s}$ . More precise analyses have been made, resulting in maximum cross sections of  $5.2 \cdot 10^{-26} \text{ cm}^3/\text{s}$  or  $2.2 \cdot 10^{-26} \text{ cm}^3/\text{s}$ , depending on estimated DM particle mass scale [73]. Since the relative velocity distribution  $P_{r,\text{rel}}(v_{\text{rel}})$  is normalized and the annihilation rate factor  $\sigma_0 v_{\text{rel}}$  should be constant as motivated in late section 3, it must apply that  $\overline{\sigma_0 v_{\text{rel}}} = \sigma_0 v_{\text{rel}}$ . Thus, the value of the terms  $\sigma v_{\text{rel}}$  is

$$\sigma v_{\text{rel}} = \sigma_0 v_{\text{rel}} S(v_{\text{rel}}) \approx 3 \cdot 10^{-26} \text{ cm}^3/\text{s} \cdot S(v_{\text{rel}}). \quad (\text{A.8})$$

In section 3 it was also motivated to exclude the constant term of  $\sigma_0 v_{\text{rel}}$  from our defined J-factor expression (eq. (3.11)) in order to make comparisons with other research which did not include Sommerfeld enhancement.

---

<sup>1</sup>Comoving volume (or distance) is volume (distance) that factors out the expansion of the universe, giving a volume (distance) that does not change in time due to the expansion of space.

## Appendix B

# Dimensionless relative velocity distribution

Looking at the expression for the relative velocity distribution in eq. (5.22), as well as its constituent parts – the DF from the Eddington formula (5.15), the density distribution (6.14), and the gravitational potential (6.15), it seems that a numerical evaluation might be made simpler if it is done in terms of dimensionless quantities.

From (6.14) and (6.15) it is evident that a very natural way to do so is by setting the length scale to  $r_0$  and the density scale to  $\rho_0$  giving the dimensionless entities, in the case of a cored Zhao density profile

$$x = \frac{r}{r_0}, \quad \text{and} \quad \tilde{\rho}(x) = \frac{\rho(r_0 x)}{\rho_0} = \frac{1}{(1+x)^3}. \quad (\text{B.1})$$

Inserting this in (6.15) then gives a dimensionless gravitational potential

$$\tilde{\Phi}(x) = \frac{\Phi(r_0 x)}{G\rho_0 r_0^2} = -4\pi \left( \frac{\log(x+1)}{x} - \frac{1}{2(x+1)} \right). \quad (\text{B.2})$$

Eddington's formula eq. (5.15) is, however, stated in terms of the relative gravitational potential  $\Psi(r) = -\Phi(r) + \Phi_0$ . Taking  $\Phi_0 = 0$  gives a dimensionless version of  $\Psi$  as

$$\tilde{\Psi}(x) = -\tilde{\Phi}(x) = 4\pi \left( \frac{\log(x+1)}{x} - \frac{1}{2(x+1)} \right). \quad (\text{B.3})$$

It is easily seen that the  $\rho$  and  $\Phi$  of an NFW DM density profile can be rendered dimensionless in the same manner. For simplicity we now introduce the relative energy scale  $\Psi_0 = G\rho_0 r_0^2$ , giving  $\Psi(r) = \Psi_0 \tilde{\Psi}(x)$ . The relative energy  $\mathcal{E} = \Psi(r) - v^2/2$  can now be made dimensionless through

$$\mathcal{E} = \Psi_0 \tilde{\mathcal{E}} \Leftrightarrow \tilde{\mathcal{E}} = \tilde{\Psi}(x) - \frac{\tilde{v}^2}{2}, \quad (\text{B.4})$$

where we have introduced the dimensionless velocity  $\tilde{v} = v/v_0$ , with  $v_0 = \sqrt{\Psi_0} = r_0 \sqrt{G\rho_0}$ .

The next step is to perform a change of variables from  $r$  to  $x$  in the Eddington formula, for which the relations  $dr = r_0 dx$ , and

$$\frac{d}{dr} = \frac{d}{dx} \frac{dx}{dr} = \frac{1}{r_0} \frac{d}{dx}, \quad (\text{B.5})$$

will be needed. Breaking down eq. (5.15) by parts gives

$$\frac{dr}{\sqrt{\mathcal{E} - \Psi(r)}} = \frac{r_0}{\sqrt{\Psi_0}} \frac{dx}{\sqrt{\tilde{\mathcal{E}} - \tilde{\Psi}(x)}} \quad (\text{B.6})$$

$$\frac{d\rho}{dr} \frac{d^2\Psi}{dr^2} \left( \frac{d\Psi}{dr} \right)^{-2} = \frac{\rho_0 d\tilde{\rho}}{r_0 dx} \frac{\Psi_0 d^2\tilde{\Psi}}{r_0^2 dx^2} \left( \frac{\Psi_0 d\tilde{\Psi}}{r_0 dx} \right)^{-2} = \frac{\rho_0}{r_0 \Psi_0} \frac{d\tilde{\rho}}{dx} \frac{d^2\tilde{\Psi}}{dx^2} \left( \frac{d\tilde{\Psi}}{dx} \right)^{-2} \quad (\text{B.7})$$

and

$$\frac{d^2\rho}{dr^2} \left( \frac{d\Psi}{dr} \right)^{-1} = \frac{\rho_0 d^2\tilde{\rho}}{r_0^2 dx^2} \left( \frac{\Psi_0 d\tilde{\Psi}}{r_0 dx} \right)^{-1} = \frac{\rho_0}{r_0\Psi_0} \frac{d^2\tilde{\rho}}{dx^2} \left( \frac{d\tilde{\Psi}}{dx} \right)^{-1}. \quad (\text{B.8})$$

Noting that

$$r = \Psi^{-1}(\mathcal{E}) \Leftrightarrow x = \tilde{\Psi}^{-1}(\tilde{\mathcal{E}}), \quad \text{and} \quad r \rightarrow \infty \Leftrightarrow x \rightarrow \infty, \quad (\text{B.9})$$

the full Eddington formula turns into

$$f(\mathcal{E}) = \frac{\rho_0}{\sqrt{8\pi^2\Psi_0^{3/2}}} \int_{\tilde{\Psi}^{-1}(\tilde{\mathcal{E}})}^{\infty} \frac{dx}{\sqrt{\tilde{\mathcal{E}} - \tilde{\Psi}(x)}} \left[ \frac{d\tilde{\rho}}{dx} \frac{d^2\tilde{\Psi}}{dx^2} \left( \frac{d\tilde{\Psi}}{dx} \right)^{-2} - \frac{d^2\tilde{\rho}}{dx^2} \left( \frac{d\tilde{\Psi}}{dx} \right)^{-1} \right]. \quad (\text{B.10})$$

Taking the integral as  $\tilde{f}(\tilde{\mathcal{E}})$  and substituting  $v_0 = \sqrt{\Psi_0}$  gives

$$f(\mathcal{E}) = \frac{\rho_0}{\sqrt{8\pi^2 v_0^3}} \tilde{f}(\tilde{\mathcal{E}}) = f_0 \tilde{f}(\tilde{\mathcal{E}}). \quad (\text{B.11})$$

Finally, this expression can be inserted in eq. (5.22), giving, with  $\tilde{v}_{\text{cm}} = v_{\text{cm}}/v_0$ ,  $dv_{\text{cm}} = v_0 d\tilde{v}_{\text{cm}}$  and  $\tilde{v}_{\text{rel}} = v_{\text{rel}}/v_0$

$$P_{r,\text{rel}}(v_{\text{rel}}) = \frac{16\pi^2 v_{\text{rel}}^2 f_0^2}{\rho^2(r)} \int_0^\infty d\tilde{v}_{\text{cm}} v_0^3 \tilde{v}_{\text{cm}}^2 \int_0^1 dz \tilde{f} \left( \frac{r}{r_0}, \tilde{v}_{\text{cm}}^2 + \frac{\tilde{v}_{\text{rel}}^2}{4} - \tilde{v}_{\text{cm}} \tilde{v}_{\text{rel}} z \right) \times \tilde{f} \left( \frac{r}{r_0}, \tilde{v}_{\text{cm}}^2 + \frac{\tilde{v}_{\text{rel}}^2}{4} + \tilde{v}_{\text{cm}} \tilde{v}_{\text{rel}} z \right). \quad (\text{B.12})$$

This simplifies to

$$P_{r,\text{rel}}(v_{\text{rel}}) = \frac{2 v_{\text{rel}}^2}{\pi^2 v_0^3 \tilde{\rho}^2(x)} \int_0^\infty d\tilde{v}_{\text{cm}} \tilde{v}_{\text{cm}}^2 \int_0^1 dz \tilde{f} \left( x, \tilde{v}_{\text{cm}}^2 + \frac{\tilde{v}_{\text{rel}}^2}{4} - \tilde{v}_{\text{cm}} \tilde{v}_{\text{rel}} z \right) \times \tilde{f} \left( x, \tilde{v}_{\text{cm}}^2 + \frac{\tilde{v}_{\text{rel}}^2}{4} + \tilde{v}_{\text{cm}} \tilde{v}_{\text{rel}} z \right), \quad (\text{B.13})$$

giving an expression for the relative velocity distribution in terms of dimensionless entities.

# Appendix C

## The Jeans equations

Galaxies are often viewed as a system of particles in six dimensional *phase space*, where the stars are seen as particles in a gas. The galaxy is then instantaneously described as a distribution function  $f(\mathbf{r}, \mathbf{v}, t)$  over the phase space. We can define a 6-dimensional phase space vector,  $\mathbf{w} = (\mathbf{r}, \mathbf{v})$ , and the velocity of the flow in phase space is then  $\dot{\mathbf{w}} = (\dot{\mathbf{r}}, \dot{\mathbf{v}}) = (\mathbf{v}, -\nabla\Phi)$ . In the absence of collisions between stars, and under the assumption that they are neither created nor destroyed in the system, the flow in phase space must conserve mass.

Consider an ordinary fluid in an arbitrary closed volume  $V$  bounded by a surface  $S$ . The mass of the fluid inside of  $V$  is

$$M(t) = \int_V \rho(\mathbf{r}, t) d^3\mathbf{r}, \quad \text{and} \quad \frac{dM}{dt} = \int_V \frac{d\rho}{dt} d^3\mathbf{r}.$$

The mass flowing out of the volume through an area element  $d^2S$  per unit time is familiarly given by  $\rho\mathbf{v} d^2S$ , where  $d^2S$  is an outward pointing vector normal to the surface  $S$ . Thus, the flow rate can be rewritten as

$$\frac{dM}{dt} = - \int_S \rho\mathbf{v} d^2S, \quad \text{or} \quad \int_V \frac{d\rho}{dt} d^3\mathbf{r} = - \int_S \rho\mathbf{v} d^2S.$$

Using the divergence theorem, we obtain

$$\int_V \left( \frac{\partial\rho}{\partial t} + \nabla \cdot (\rho\mathbf{v}) \right) d^3\mathbf{r} = 0.$$

Since this must be true for all volumes  $V$ , we obtain the continuity equation

$$\frac{\partial\rho}{\partial t} + \nabla \cdot (\rho\mathbf{v}) = 0.$$

Similarly this applies to our six dimensional phase space flow, which is given by

$$\frac{\partial f}{\partial t} + \nabla \cdot (f\dot{\mathbf{w}}) = 0. \tag{C.1}$$

This is called the Liouville equation or the collisionless Boltzmann equation (CBE). This equation can be simplified. Starting with writing out the second term,

$$\nabla \cdot (f\dot{\mathbf{w}}) = \sum_{i=1}^6 \frac{\partial(f\dot{w}_i)}{\partial w_i} = f \sum_{i=1}^3 \left( \frac{\partial v_i}{\partial r_i} + \frac{\partial \dot{v}_i}{\partial v_i} \right) + \sum_{i=1}^3 \left( v_i \frac{\partial f}{\partial r_i} + \dot{v}_i \frac{\partial f}{\partial v_i} \right).$$

Since  $r_i$  and  $v_i$  are independent phase space coordinates, it implies that  $\partial v_i / \partial r_i = 0$ . The gradient of a potential does neither depends on velocities, so that  $\partial \dot{v}_i / \partial v_i = \frac{\partial}{\partial v_i} \left( -\frac{\partial\Phi}{\partial x_i} \right) = 0$ . The CBE can now be rewritten so that

$$\frac{\partial f}{\partial t} + v_i \frac{\partial f}{\partial r_i} - \frac{\partial\Phi}{\partial r_i} \frac{\partial f}{\partial v_i} = 0.$$

Now turning to the left term in eq. C.1, since  $f = f(\mathbf{r}, \mathbf{v}, t)$ , we have by the chain rule that

$$df = \frac{\partial f}{\partial t} dt + \frac{\partial f}{\partial r_i} dr_i + \frac{\partial f}{\partial v_i} dv_i,$$

and thus

$$\frac{df}{dt} = \frac{\partial f}{\partial t} + \frac{\partial f}{\partial r_i} v_i - \frac{\partial \Phi}{\partial r_i} \frac{\partial f}{\partial v_i}.$$

We see that this is the same result as for the right hand side term, and we conclude that the CBE can be written in the more compact form of

$$\frac{df}{dt} = 0. \quad (\text{C.2})$$

The physical interpretation of this equation is that the phase space density  $f$  around the phase point of a given star always remain the same. Although eq. C.2 looks very simple, solving it for  $f$  is effectively impossible, it is more practical to consider moment equations.

We start by considering moment equations related to  $v_i^l v_j^m v_k^n$  where the indices  $(i, j, k)$  refer to generalised coordinates, and  $(l, m, n)$  are integers. By recalling that

$$\rho = \int f d^3 \mathbf{v}, \quad \text{and} \quad \overline{\rho v_i^l v_j^m v_k^n} = \int v_i^l v_j^m v_k^n f d^3 \mathbf{v}, \quad (\text{C.3})$$

the  $(l + m + n)^{\text{th}}$  moment equation of the CBE is

$$\int v_i^l v_j^m v_k^n \frac{\partial f}{\partial t} d^3 \mathbf{v} + \int v_i^l v_j^m v_k^n v_a \frac{\partial f}{\partial x_a} d^3 \mathbf{v} - \int v_i^l v_j^m v_k^n \frac{\partial \Phi}{\partial x_a} \frac{\partial f}{\partial v_a} d^3 \mathbf{v} = 0.$$

Since the integration range does not depend on  $t$  the term  $\partial/\partial t$  can be taken outside the integral. Neither of the terms  $\partial/\partial x_i$  and  $\partial\Phi/\partial x_i$  depend on  $v_i$ , and they can therefore be moved outside their corresponding integrals as well, yielding

$$\frac{\partial}{\partial t} \int v_i^l v_j^m v_k^n f d^3 \mathbf{v} + \frac{\partial}{\partial x_i} \int v_i^l v_j^m v_k^n v_a f d^3 \mathbf{v} - \frac{\partial \Phi}{\partial x_a} \int v_i^l v_j^m v_k^n \frac{\partial f}{\partial v_a} d^3 \mathbf{v} = 0.$$

Using the relations in eq. (C.3) allows us to rewrite the moment equations as

$$\frac{\partial}{\partial t} (\overline{\rho v_i^l v_j^m v_k^n}) + \frac{\partial}{\partial x_i} (\overline{\rho v_i^l v_j^m v_k^n v_a}) - \frac{\partial \Phi}{\partial x_a} \int v_i^l v_j^m v_k^n \frac{\partial f}{\partial v_a} d^3 \mathbf{v} = 0. \quad (\text{C.4})$$

The  $0^{\text{th}}$  moment ( $l = m = n = 0$ ) can now be easily evaluated, we obtain

$$\frac{\partial \rho}{\partial t} + \frac{\partial \rho \bar{v}_i}{\partial x_i} - \frac{\partial \Phi}{\partial x_i} \int \frac{\partial f}{\partial v_i} d^3 \mathbf{v} = 0. \quad (\text{C.5})$$

Using the divergence theorem, one can write

$$\int \frac{\partial f}{\partial v_i} d^3 \mathbf{v} = \int f d^2 \mathbf{S} = 0,$$

where the last equality follows from that  $f \rightarrow 0$  as  $|v| \rightarrow \infty$  which is required from that the phase-space density must go to zero at infinity. Hence, the  $0^{\text{th}}$  moment of the CBE reduces to the continuity equation

$$\frac{\partial \rho}{\partial t} + \frac{\partial(\rho \bar{v}_i)}{\partial x_i} = 0, \quad (\text{C.6})$$

which is identical of that of fluid dynamics.

Next we consider the first-order moment equation where  $(l, m, n) = (1, 0, 0)$  or  $(0, 1, 0)$  or  $(0, 0, 1)$ . In this case eq. (C.4) reduces to

$$\begin{aligned}
 \int v_j \frac{\partial f}{\partial t} d^3\mathbf{v} + \int v_i v_j \frac{\partial f}{\partial x_i} d^3\mathbf{v} - \int v_j \frac{\partial \Phi}{\partial x_i} \frac{\partial f}{\partial v_i} d^3\mathbf{v} &= 0 \\
 \Leftrightarrow \frac{\partial(\rho \bar{v}_j)}{\partial t} + \frac{\partial(\rho \bar{v}_i \bar{v}_j)}{\partial x_i} - \frac{\partial \Phi}{\partial x_i} \int v_j \frac{\partial f}{\partial v_i} d^3\mathbf{v} &= 0.
 \end{aligned} \tag{C.7}$$

Using integration by parts one can write

$$\begin{aligned}
 \int v_j \frac{\partial f}{\partial v_i} d^3\mathbf{v} &= \int \frac{\partial(v_j f)}{\partial v_i} d^3\mathbf{v} - \int \frac{\partial v_j}{\partial v_i} f d^3\mathbf{v} \\
 &= \int v_j f d^2\mathbf{S} - \int \delta_{ij} f d^3\mathbf{v} \\
 &= -\delta_{ij} \rho,
 \end{aligned}$$

which gives us

$$\frac{\partial(\rho \bar{v}_j)}{\partial t} + \frac{\partial(\rho \bar{v}_i \bar{v}_j)}{\partial x_i} + \rho \frac{\partial \Phi}{\partial x_j} = 0. \tag{C.8}$$

Note that this represent a set of three moment equations for  $j = (1, 2, 3)$  and that a summation over  $i$  is implied. The so-called Jeans equations are obtained by subtracting  $\bar{v}_j$  times the continuity equation from the 1<sup>st</sup>-order momentum equations:

$$\begin{aligned}
 \bar{v}_j \frac{\partial \rho}{\partial t} + \bar{v}_j \frac{\partial(\rho \bar{v}_i)}{\partial x_i} &= 0 \\
 \Leftrightarrow \frac{\partial(\rho \bar{v}_j)}{\partial t} - \rho \frac{\partial \bar{v}_j}{\partial t} + \frac{\partial(\rho \bar{v}_i \bar{v}_j)}{\partial x_i} - \rho \bar{v}_i \frac{\partial \bar{v}_j}{\partial x_i} &= 0
 \end{aligned}$$

Subtracting this from the first-order moment equations (C.8) yields

$$\frac{\partial(\rho \bar{v}_i \bar{v}_j)}{\partial x_i} + \rho \frac{\partial \Phi}{\partial x_j} + \rho \frac{\partial \bar{v}_j}{\partial t} - \frac{\partial(\rho \bar{v}_i \bar{v}_j)}{\partial x_i} + \rho \bar{v}_i \frac{\partial \bar{v}_j}{\partial x_i} = 0.$$

If we define  $\sigma_{ij}^2 = \bar{v}_i \bar{v}_j - \bar{v}_i \bar{v}_j$ , we obtain

$$\rho \frac{\partial \bar{v}_j}{\partial t} + \rho \bar{v}_i \frac{\partial \bar{v}_j}{\partial x_i} = -\rho \frac{\partial \Phi}{\partial x_j} - \frac{\partial(\rho \sigma_{ij}^2)}{\partial x_i}. \tag{C.9}$$

Once again, this represent a set of three equations for  $j = (1, 2, 3)$  and the implied summation over  $i$  remains. These are called the Jeans equations.

Using spherical coordinates, that is  $j = (r, \theta, \phi)$ , equation C.2 becomes

$$\frac{df}{dt} = \frac{\partial f}{\partial t} + \dot{r} \frac{\partial f}{\partial r} + \dot{\phi} \frac{\partial f}{\partial \phi} + \dot{\theta} \frac{\partial f}{\partial \theta} + \dot{v}_r \frac{\partial f}{\partial v_\theta} + \dot{v}_\phi \frac{\partial f}{\partial v_\phi} + \dot{v}_\theta \frac{\partial f}{\partial v_\theta} = 0. \tag{C.10}$$

Deriving the velocity components

$$\dot{r} = v_r, \quad \dot{\theta} = \frac{v_\theta}{r}, \quad \dot{\phi} = \frac{v_\phi}{r \sin \theta}, \tag{C.11}$$

gives

$$\dot{v}_r = \ddot{r}, \quad \dot{v}_\theta = r\ddot{\theta} + \dot{r}\dot{\theta}, \quad \dot{v}_\phi = \sin \theta \dot{r}\dot{\phi} + r \sin \theta \ddot{\phi} + r\dot{\phi}\dot{\theta} \cos \theta. \tag{C.12}$$

Matching the acceleration given by

$$\mathbf{a} = -\nabla \Phi = -\frac{\partial \Phi}{\partial r} \hat{r} - \frac{1}{r} \frac{\partial \Phi}{\partial \theta} \hat{\theta} - \frac{1}{r \sin \theta} \frac{\partial \Phi}{\partial \phi} \hat{\phi}, \tag{C.13}$$

to the acceleration in spherical coordinates

$$\mathbf{a} = (\ddot{r} - r\dot{\theta}^2 + r\dot{\phi}^2 \sin^2 \theta)\hat{r} + (r\ddot{\theta} + 2\dot{r}\dot{\theta} - r\dot{\phi}^2 \sin \theta \cos \theta)\hat{\theta} + (r\ddot{\phi} \sin \theta + 2\dot{r}\dot{\phi} \sin \theta + 2r\dot{\theta}\dot{\phi} \cos \theta)\hat{\phi}, \quad (\text{C.14})$$

yields the identities

$$\begin{aligned} \dot{v}_r &= -\frac{\partial\Phi}{\partial r} + r\dot{\theta}^2 - r\dot{\phi}^2 \sin^2 \theta = -\frac{\partial\Phi}{\partial r} + \frac{v_\theta^2 + v_\phi^2}{r}, \\ \dot{v}_\theta &= -\frac{1}{r}\frac{\partial\Phi}{\partial\theta} - \dot{r}\dot{\theta} + r\dot{\phi}^2 \sin \theta \cos \theta = -\frac{1}{r}\frac{\partial\Phi}{\partial\theta} + \frac{v_\phi^2 \cot \theta - v_r v_\theta}{r}, \\ \dot{v}_\phi &= -\frac{1}{r \sin \theta}\frac{\partial\Phi}{\partial\phi} - \dot{r}\dot{\phi} \sin \theta - r\dot{\theta}\dot{\phi} \cos \theta = -\frac{1}{r \sin \theta}\frac{\partial\Phi}{\partial\phi} - \frac{v_\phi v_r + v_\theta v_\phi \cot \theta}{r}. \end{aligned} \quad (\text{C.15})$$

Hence the collisionless Boltzmann equation in spherical coordinates can be written

$$\begin{aligned} 0 &= \frac{\partial f}{\partial t} + v_r \frac{\partial f}{\partial r} + \frac{v_\theta}{r} \frac{\partial f}{\partial \theta} + \frac{v_\phi}{r \sin \theta} \frac{\partial f}{\partial \phi} + \left( \frac{v_\theta^2 + v_\phi^2}{r} - \frac{\partial\Phi}{\partial r} \right) \frac{\partial f}{\partial v_r} \\ &\quad + \frac{1}{r} \left( v_\phi^2 \cot \theta - v_r v_\theta - \frac{\partial\Phi}{\partial \theta} \right) \frac{\partial f}{\partial v_\theta} - \frac{1}{r} \left( v_\phi (v_r + v_\theta \cot \theta) + \frac{1}{\sin \theta} \frac{\partial\Phi}{\partial \theta} \right) \frac{\partial f}{\partial v_\phi}. \end{aligned} \quad (\text{C.16})$$

Assuming a spherically symmetric system in a steady state, and that the galaxy have spherical symmetry with respect to velocity, and gravitational potential  $\Phi$ , it can be assumed that

$$\frac{\partial f}{\partial \theta} = \frac{\partial f}{\partial \phi} = 0, \quad \text{and} \quad \frac{\partial\Phi}{\partial \theta} = \frac{\partial\Phi}{\partial \phi} = 0 \quad \text{since} \quad \Phi = -\frac{GM(r)}{r}, \quad (\text{C.17})$$

leaving the equation

$$\frac{\partial f}{\partial t} + v_r \frac{\partial f}{\partial r} + \left( \frac{v_\theta^2 + v_\phi^2}{r} - \frac{\partial\Phi}{\partial r} \right) \frac{\partial f}{\partial v_r} + \frac{1}{r} (v_\phi^2 \cot \theta - v_r v_\theta) \frac{\partial f}{\partial v_\theta} - \frac{1}{r} (v_\phi (v_r + v_\theta \cot \theta)) \frac{\partial f}{\partial v_\phi} = 0. \quad (\text{C.18})$$

By multiplying this equation with  $v_i$  and integrate over  $v$ -space, we derive the 1<sup>st</sup> moment equations in spherical coordinates. For each term in eq. (C.18), we get

$$\begin{aligned} \int v_i \frac{\partial f}{\partial t} d^3\mathbf{v} &= \frac{\partial}{\partial t} \int v_i f d^3\mathbf{v} = \frac{\partial(\rho \bar{v}_i)}{\partial t}, \\ \int v_i v_r \frac{\partial f}{\partial r} d^3\mathbf{v} &= \frac{\partial}{\partial r} \int v_i v_r f d^3\mathbf{v} = \frac{\partial(\rho \bar{v}_i \bar{v}_r)}{\partial r}, \\ \int v_i \frac{v_\theta^2 + v_\phi^2}{r} \frac{\partial f}{\partial v_r} d^3\mathbf{v} &= \frac{1}{r} \left[ \int \frac{\partial(v_i (v_\theta^2 + v_\phi^2) f)}{\partial v_r} d^3\mathbf{v} - \int \frac{\partial(v_i (v_\theta^2 + v_\phi^2))}{\partial v_r} f d^3\mathbf{v} \right] = -\frac{\rho}{r} (\bar{v}_\theta^2 + \bar{v}_\phi^2) \delta_{ir} \\ &\quad - \int v_i \frac{\partial\Phi}{\partial r} \frac{\partial f}{\partial v_r} d^3\mathbf{v} = -\frac{\partial\Phi}{\partial r} \left[ \int \frac{\partial(v_i f)}{\partial v_r} d^3\mathbf{v} - \int \frac{\partial v_i}{\partial v_r} f d^3\mathbf{v} \right] = \rho \frac{\partial\Phi}{\partial r} \delta_{ir} \\ \int v_i \frac{v_\phi^2 \cot \theta}{r} \frac{\partial f}{\partial v_\theta} d^3\mathbf{v} &= \frac{\cot \theta}{r} \left[ \int \frac{\partial(v_i v_\phi^2 f)}{\partial v_\theta} d^3\mathbf{v} - \int \frac{\partial v_i v_\phi^2}{\partial v_\theta} f d^3\mathbf{v} \right] = -\frac{\rho \bar{v}_\phi^2 \cot \theta}{r} \delta_{i\theta} \\ &\quad - \int v_i \frac{v_r v_\theta}{r} \frac{\partial f}{\partial v_\theta} d^3\mathbf{v} = -\frac{1}{r} \left[ \int \frac{\partial(v_i v_r v_\theta f)}{\partial v_\theta} d^3\mathbf{v} - \int \frac{\partial(v_i v_r v_\theta)}{\partial v_\theta} f d^3\mathbf{v} \right] = \frac{\rho \bar{v}_i \bar{v}_r}{r} (1 + \delta_{i\theta}), \\ &\quad - \int v_i \frac{v_\phi v_r}{r} \frac{\partial f}{\partial v_\phi} d^3\mathbf{v} = -\frac{1}{r} \left[ \int \frac{\partial(v_i v_\phi v_r f)}{\partial v_\phi} d^3\mathbf{v} - \int \frac{\partial(v_i v_\phi v_r)}{\partial v_\phi} f d^3\mathbf{v} \right] = \frac{\rho \bar{v}_i \bar{v}_r}{r} (1 + \delta_{i\phi}), \\ &\quad - \int v_i \frac{v_\phi v_\theta \cot \theta}{r} \frac{\partial f}{\partial v_\phi} d^3\mathbf{v} = -\frac{\cot \theta}{r} \left[ \int \frac{\partial(v_i v_\phi v_\theta f)}{\partial v_\phi} d^3\mathbf{v} - \int \frac{\partial(v_i v_\phi v_\theta)}{\partial v_\phi} f d^3\mathbf{v} \right] = \frac{\rho \bar{v}_i \bar{v}_\theta \cot \theta}{r} (1 + \delta_{i\phi}). \end{aligned} \quad (\text{C.19})$$

Evaluating the moment equations for all velocities  $v_i$ , where  $i = (r, \theta, \phi)$ , the 1<sup>st</sup> moment equations can be written separately for every coordinate as

$$\begin{aligned} \frac{\partial(\rho\bar{v}_r)}{\partial t} + \frac{\partial(\rho\bar{v}_r^2)}{\partial r} + \frac{\rho}{r} \left( 2\bar{v}_r^2 - \bar{v}_\theta^2 - \bar{v}_\phi^2 + \bar{v}_r\bar{v}_\theta \cot\theta \right) + \rho \frac{\partial\Phi}{\partial r} &= 0, \\ \frac{\partial(\rho\bar{v}_\theta)}{\partial t} + \frac{\partial(\rho\bar{v}_r\bar{v}_\theta)}{\partial r} + \frac{\rho}{r} \left( 3\bar{v}_r\bar{v}_\theta + (\bar{v}_\theta^2 - \bar{v}_\phi^2)\cot\theta \right) &= 0, \\ \frac{\partial(\rho\bar{v}_\phi)}{\partial t} + \frac{\partial(\rho\bar{v}_r\bar{v}_\phi)}{\partial r} + \frac{\rho}{r} \left( 3\bar{v}_r\bar{v}_\phi + 2\bar{v}_\theta\bar{v}_\phi\cot\theta \right) &= 0. \end{aligned} \quad (\text{C.20})$$

Assuming a spherically symmetric system in a steady state, and that the galaxy have spherical symmetry with respect to velocity, there can be no streaming motions and all mixed second-order terms vanish. Consequently we have that

$$\frac{\partial(\rho\bar{v}_i)}{\partial t} = 0, \quad \bar{v}_r = \bar{v}_\theta = \bar{v}_\phi = \bar{v}_r\bar{v}_\theta = \bar{v}_r\bar{v}_\phi = \bar{v}_\theta\bar{v}_\phi = 0, \quad \text{and} \quad \bar{v}_\theta^2 = \bar{v}_\phi^2. \quad (\text{C.21})$$

Under these assumptions, only the radial Jeans equation remains

$$\frac{d(\rho\bar{v}_r^2)}{dr} + \frac{2\rho}{r} [\bar{v}_r^2 - \bar{v}_\theta^2] = -\rho \frac{d\Phi}{dr}. \quad (\text{C.22})$$

Defining the so-called anisotropy parameter of the velocity distribution;

$$\beta \equiv 1 - \frac{\bar{v}_\theta^2}{\bar{v}_r^2}, \quad (\text{C.23})$$

and writing out the potential, the radial Jeans equation can be written

$$\frac{1}{\rho} \frac{d(\rho\bar{v}_r^2)}{dr} + 2\frac{\beta\bar{v}_r^2}{r} = -\frac{d\Phi}{dr} = -\frac{GM(r)}{r^2}. \quad (\text{C.24})$$

# Appendix D

## Additional Results

For the sake of completeness, and in case it may be useful for future studies, this chapter is devoted to showing the parameter region and binned likelihood plots from the results section for all 20 dSphs investigated.

### D.1 Parameter regions

The  $1\sigma$ ,  $2\sigma$ ,  $3\sigma$  confidence levels in the parameter space  $r_0, v_0$  for 20 dSphs are plotted together with contour lines of the Sommerfeld enhanced J-factor in figs. D.1 to D.5.

### D.2 Binned Likelihood Functions

The binned likelihood function  $\mathcal{L}(\mathcal{J}_S)$  for 20 dSphs is plotted for 20 dSphs each modeled both by an NFW and a cored Zhao DM profile in figs. D.6 to D.10.

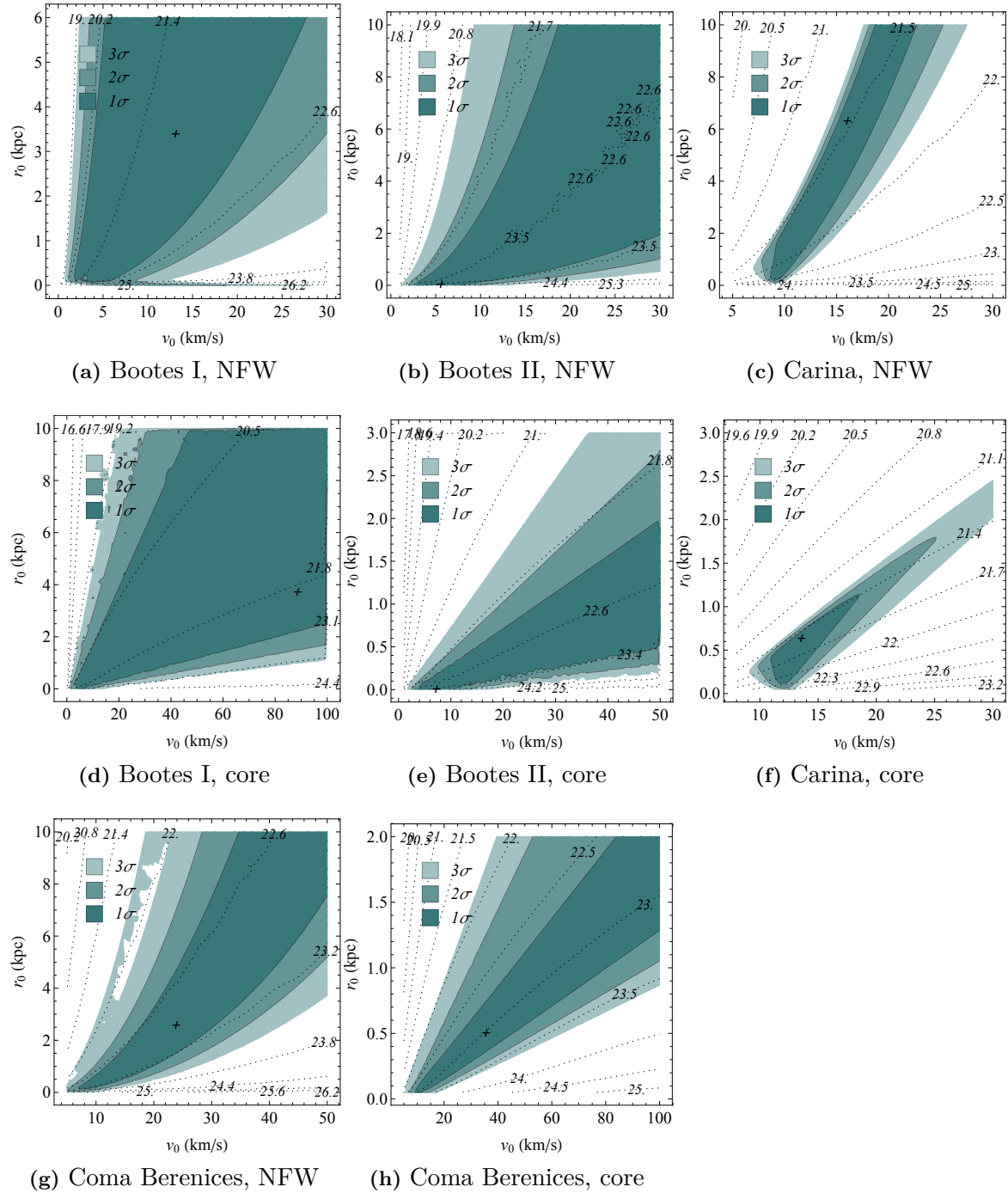


**Figure D.1:** Evaluated likelihood function and  $\mathcal{J}_S$  for Bootes I and II, Carina and Coma Berenices, modelled with NFW and cored Zhao DM profiles respectively. The coloured regions correspond to  $1\sigma$ ,  $2\sigma$ ,  $3\sigma$  confidence levels and the dotted lines are contour lines for  $\mathcal{J}_S$ .

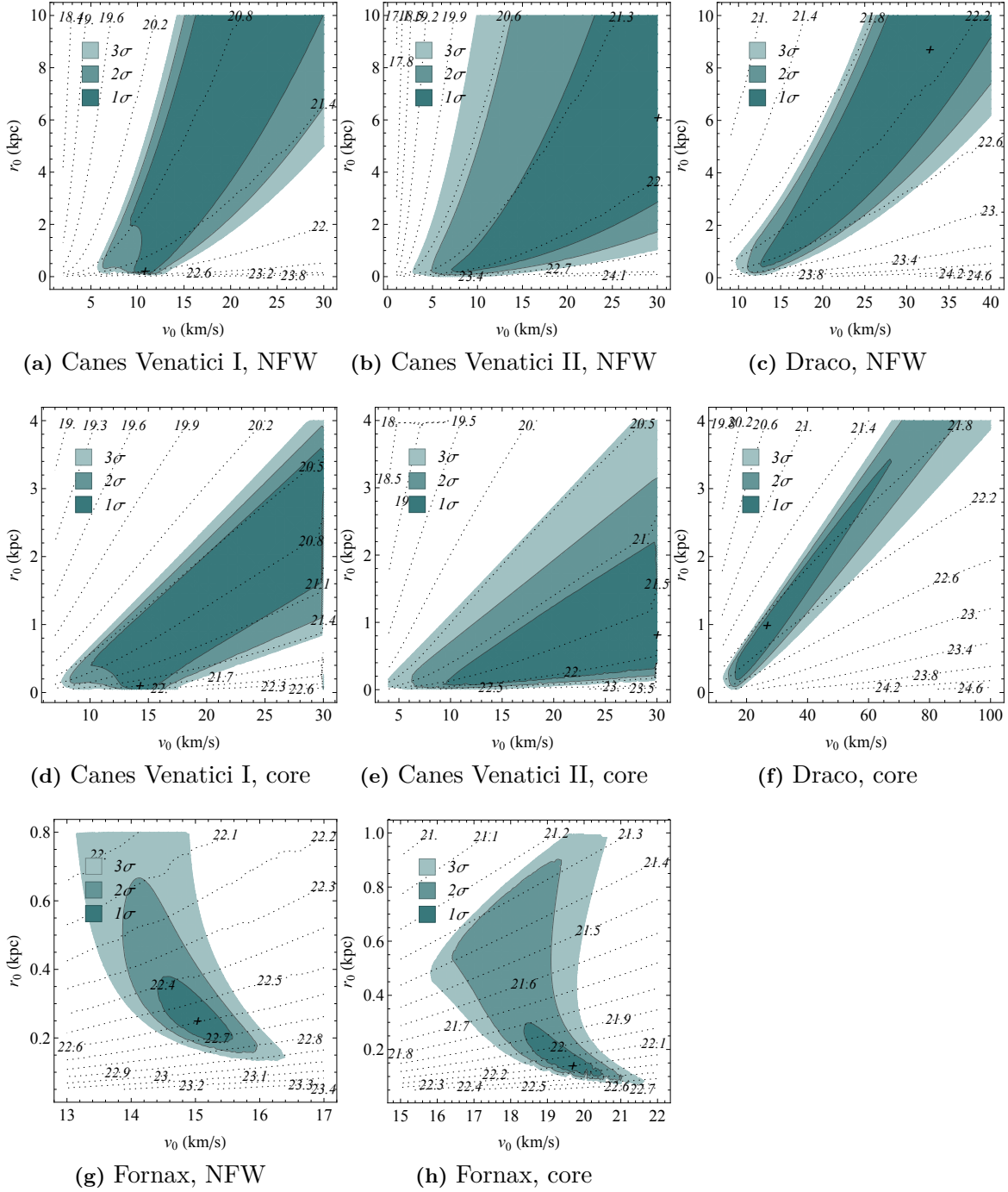


**Figure D.2:** Evaluated likelihood function and  $\mathcal{J}_S$  for Canes Venatici I and II, Draco and Fornax, modelled with NFW and cored Zhao DM profiles respectively. The coloured regions correspond to 1 $\sigma$ , 2 $\sigma$ , 3 $\sigma$  confidence levels and the dotted lines are contour lines for  $\mathcal{J}_S$ .

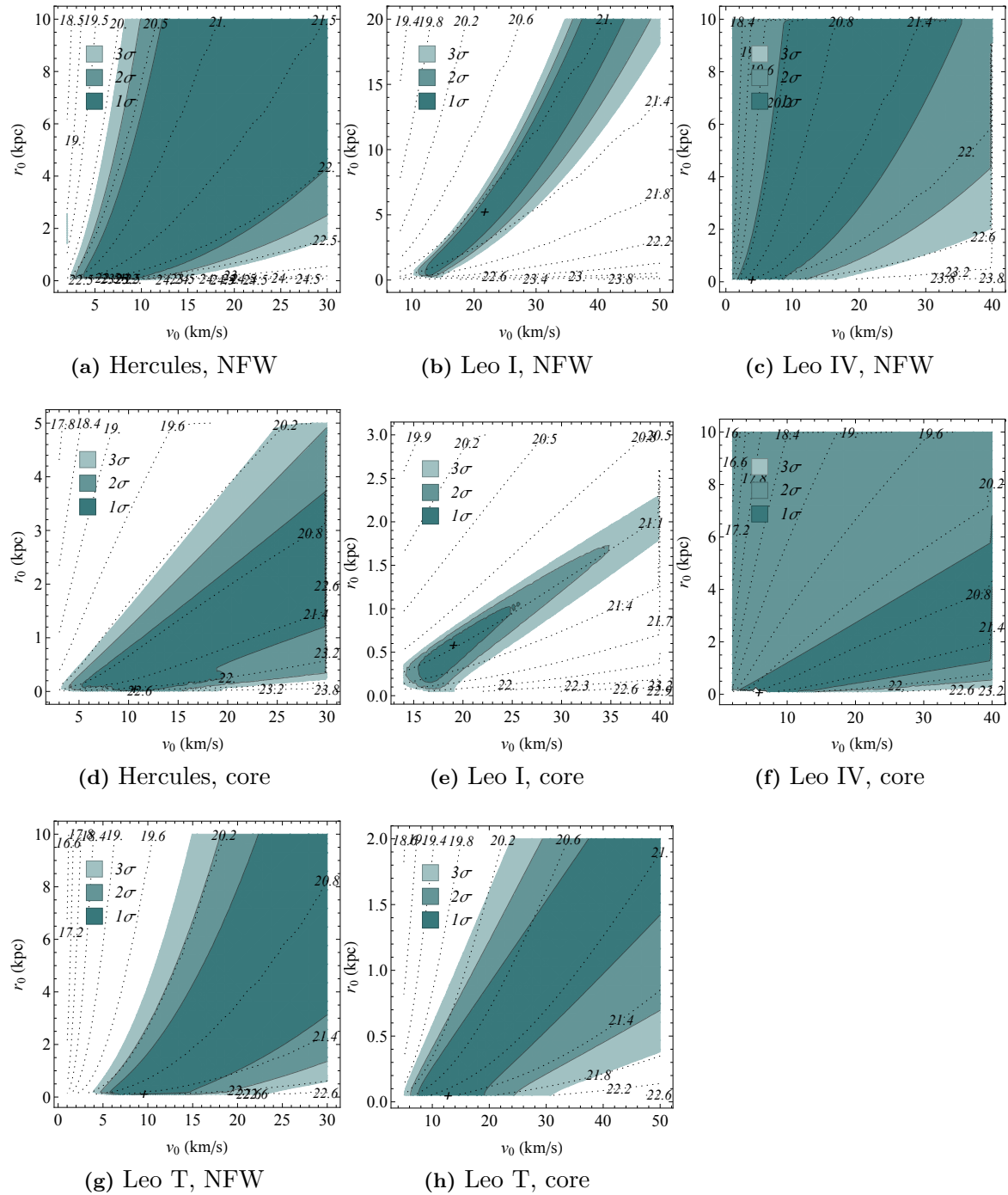


**Figure D.3:** Evaluated likelihood function and  $\mathcal{J}_S$  for Hercules, Leo I, Leo IV and Leo T, modelled with NFW and cored Zhao DM profiles respectively. The coloured regions correspond to  $1\sigma$ ,  $2\sigma$ ,  $3\sigma$  confidence levels and the dotted lines are contour lines for  $\mathcal{J}_S$ .

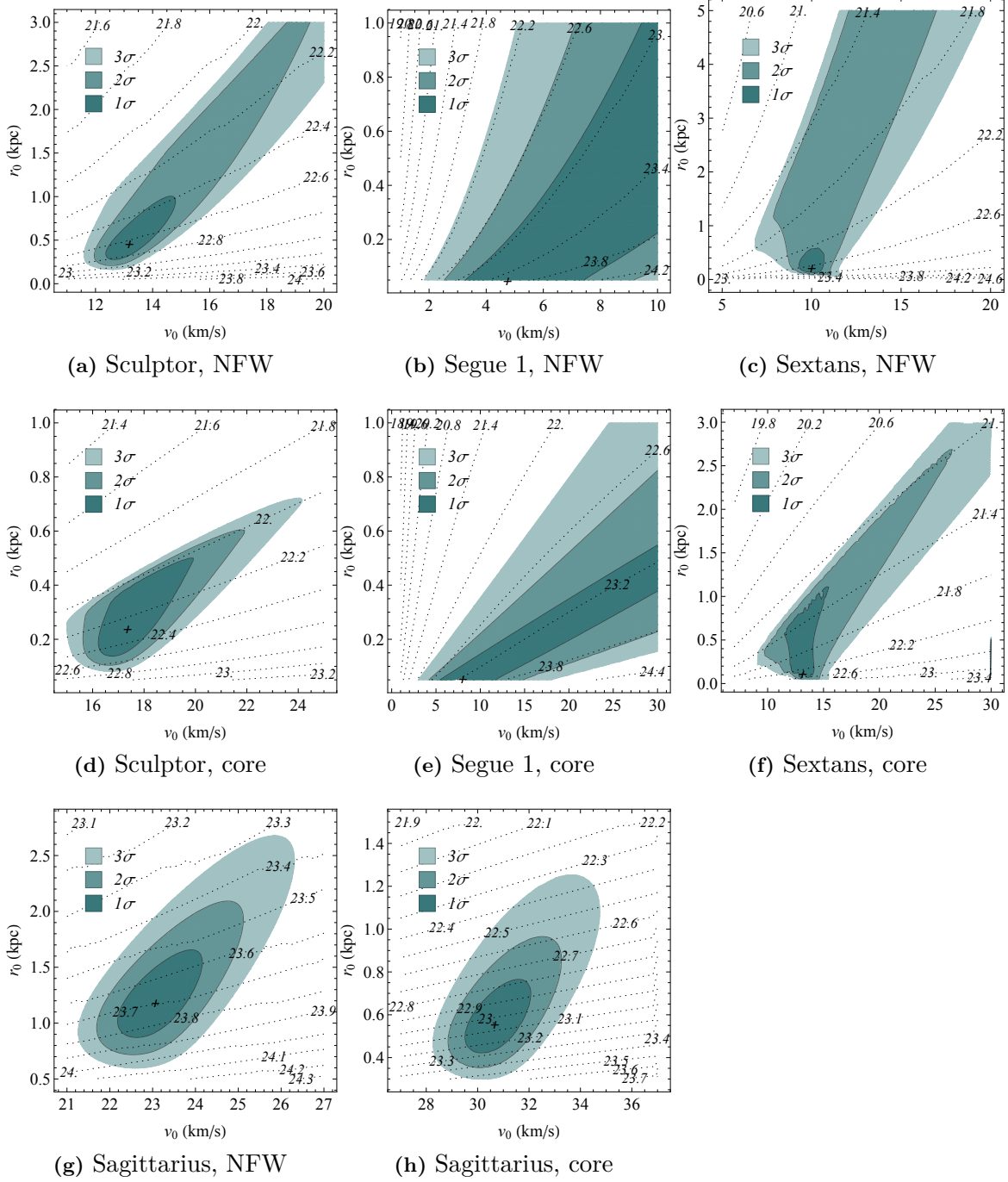


**Figure D.4:** Evaluated likelihood function and  $\mathcal{J}_S$  for Sculptor, Segue 1, Sextans and Sagittarius, modelled with NFW and cored Zhao DM profiles respectively. The coloured regions correspond to  $1\sigma$ ,  $2\sigma$ ,  $3\sigma$  confidence levels and the dotted lines are contour lines for  $\mathcal{J}_S$ .

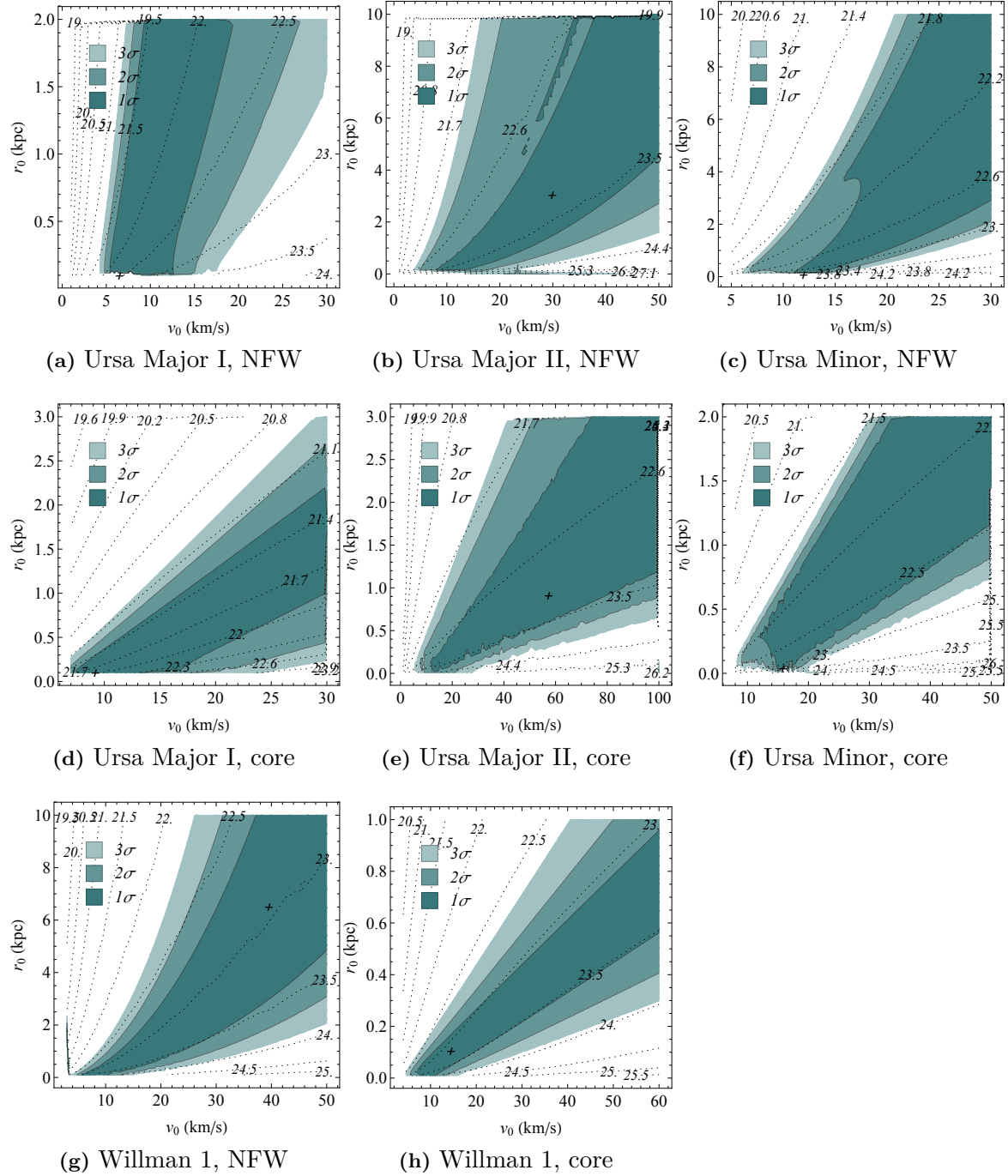


**Figure D.5:** Evaluated likelihood function and  $\mathcal{J}_S$  for Ursa Major I and II, Ursa Minor and Willman 1, modelled with NFW and cored Zhao DM profiles respectively. The coloured regions correspond to  $1\sigma$ ,  $2\sigma$ ,  $3\sigma$  confidence levels and the dotted lines are contour lines for  $\mathcal{J}_S$ .

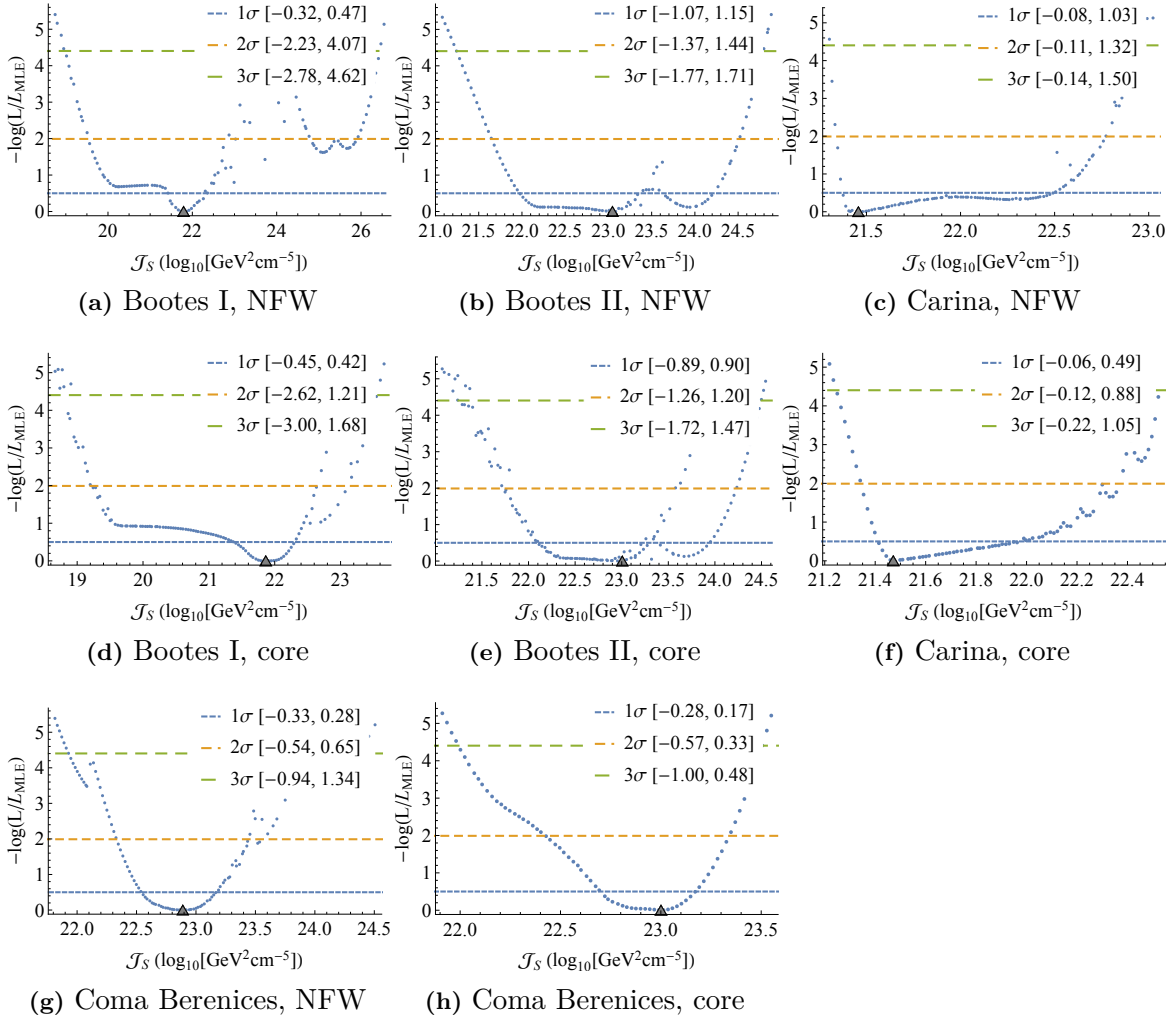


**Figure D.6:** Binned likelihood as a function of  $\mathcal{J}_S$  for Bootes I and II, Carina and Coma Berenices, modelled with NFW and cored Zhao DM profiles respectively. The grey triangle marks the MLE and the horizontal lines correspond to  $1\sigma$ ,  $2\sigma$ ,  $3\sigma$  confidence levels.

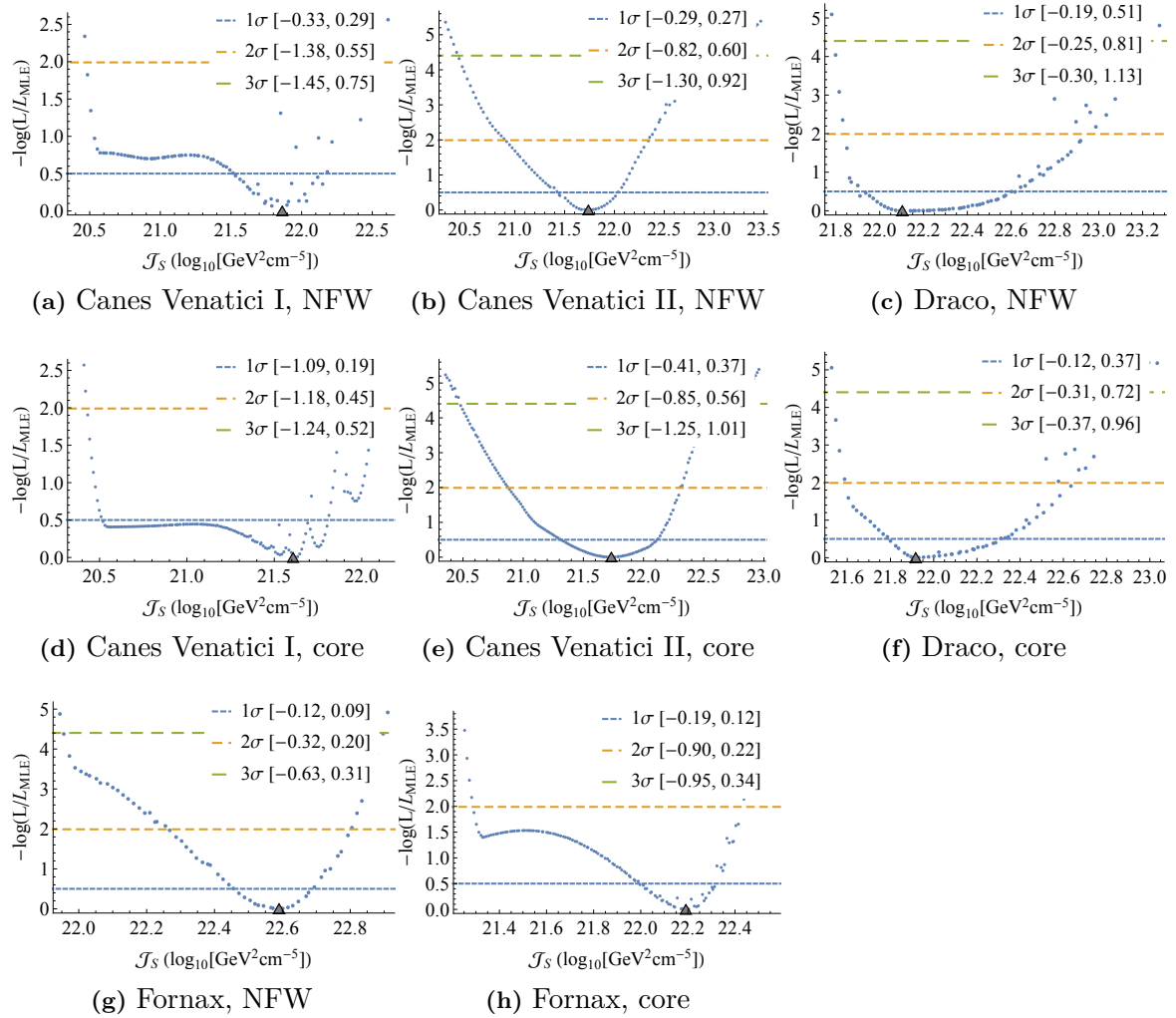


**Figure D.7:** Binned likelihood as a function of  $\mathcal{J}_S$  for Canes Venatici I and II, Draco and Fornax, modelled with NFW and cored Zhao DM profiles respectively. The grey triangle marks the MLE and the horizontal lines correspond to  $1\sigma$ ,  $2\sigma$ ,  $3\sigma$  confidence levels.

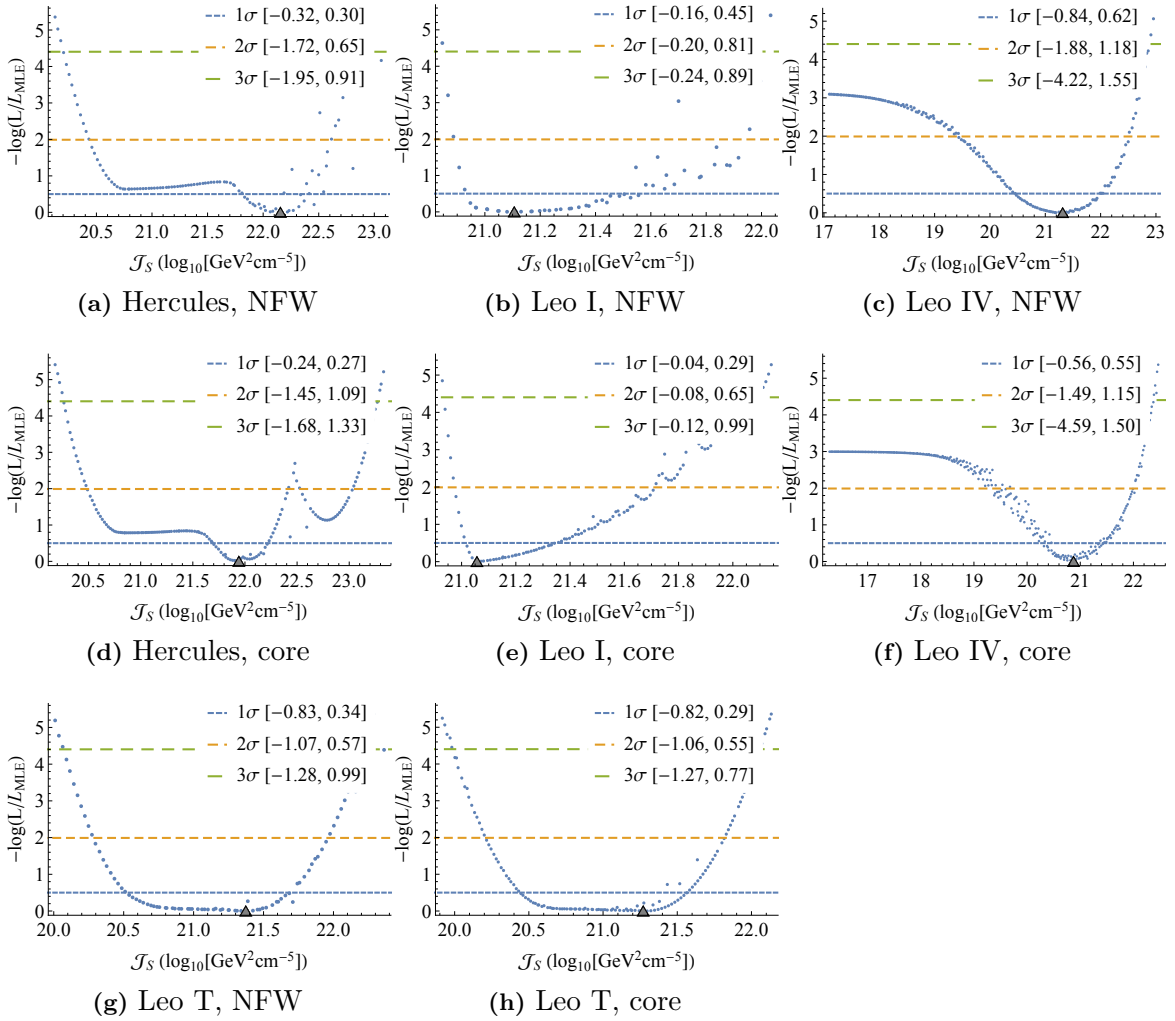


**Figure D.8:** Binned likelihood as a function of  $\mathcal{J}_S$  for Hercules, Leo I, Leo IV and Leo T, modelled with NFW and cored Zhao DM profiles respectively. The grey triangle marks the MLE and the horizontal lines correspond to  $1\sigma$ ,  $2\sigma$ ,  $3\sigma$  confidence levels.

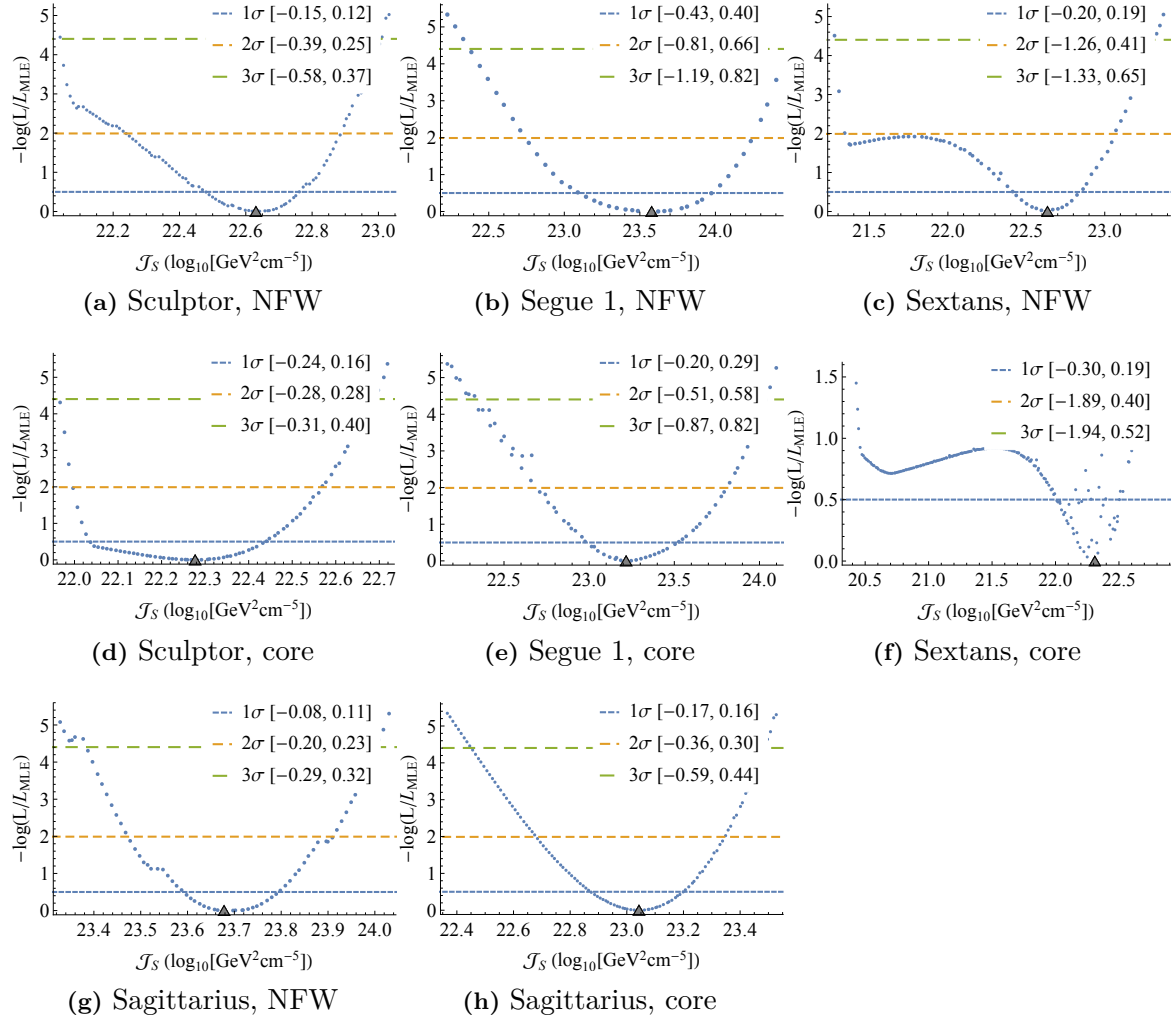


**Figure D.9:** Binned likelihood as a function of  $\mathcal{J}_S$  for Sculptor, Segue 1, Sextans and Sagittarius, modelled with NFW and cored Zhao DM profiles respectively. The grey triangle marks the MLE and the horizontal lines correspond to  $1\sigma$ ,  $2\sigma$ ,  $3\sigma$  confidence levels.

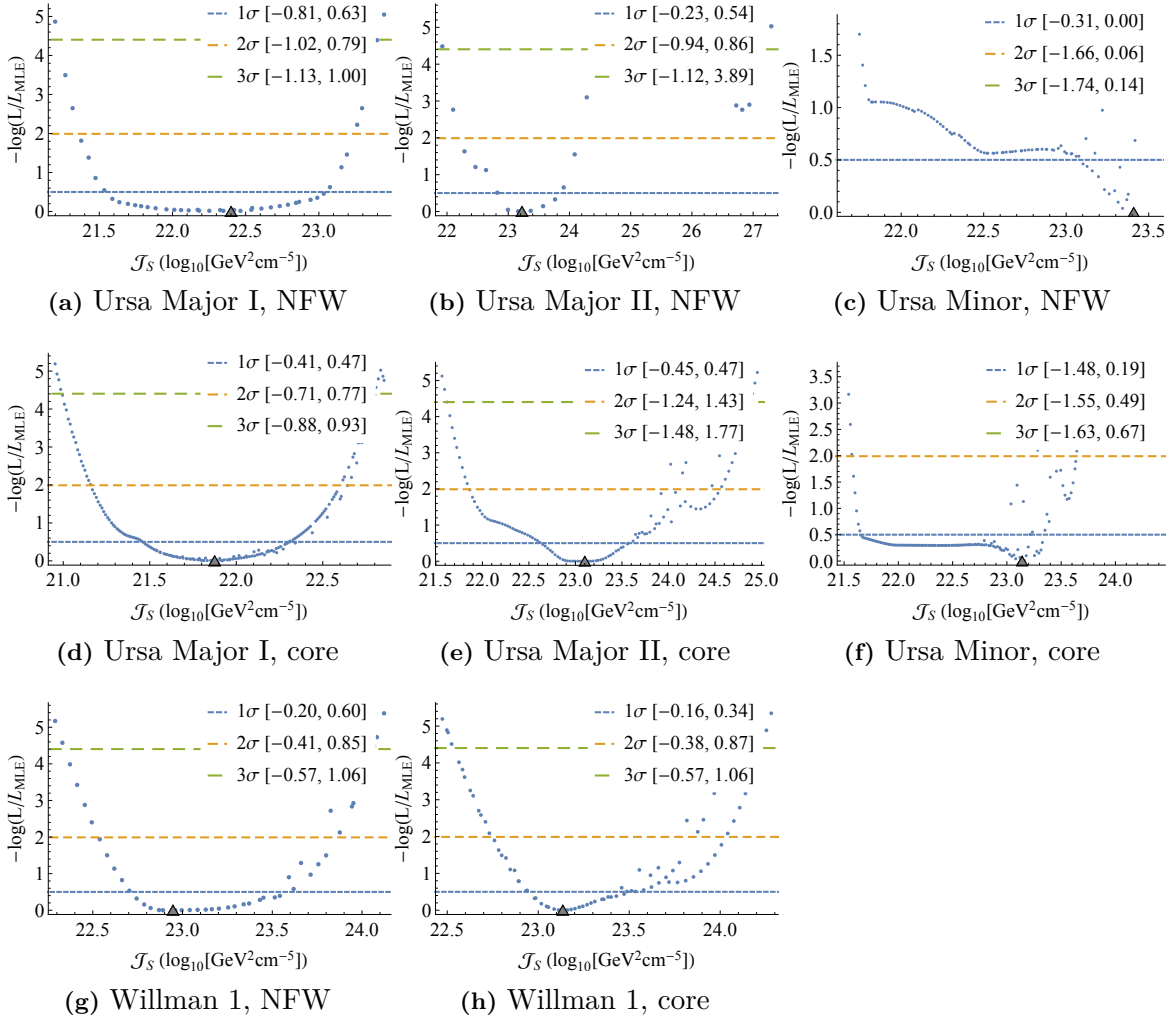


**Figure D.10:** Binned likelihood as a function of  $\mathcal{J}_S$  for Ursa Major I and II, Ursa Minor and Willman 1, modelled with NFW and cored Zhao DM profiles respectively. The grey triangle marks the MLE and the horizontal lines correspond to  $1\sigma$ ,  $2\sigma$ ,  $3\sigma$  confidence levels.

# Appendix E

## Mathematica code

Almost all numerical calculations in this project have been done using Wolfram Mathematica, and because of the nature of the individual calculations and the amount of data in the analysis, a quite significant code base have been developed. In order to supply a greater transparency as to what calculations were actually performed, the most significant parts of the code is included in this chapter. On the off-chance that someone might be interested in performing similar calculations, these code snippets might provide a good starting point and maybe help that someone avoid the most time consuming pit falls.

Included in this chapter is code for, in order:

- (i) The dimensionless version of the Eddington formula  $f(\mathcal{E})$  from section 5.1,
- (ii) The dimensionless version of the relative velocity distribution  $P_{r,\text{rel}}(v_{\text{rel}})$  from section 5.2,
- (iii) The Sommerfeld enhancement  $S(v_{\text{rel}})$  from chapter 4,
- (iv) The dimensionless version of the line of sight velocity dispersion from section 7.2.
- (v) The integral  $\Gamma(x) = \int dv_{\text{rel}} S(v_{\text{rel}}) P_{x,\text{rel}}(v_{\text{rel}})$ , which is part of the  $J_S$ -factor.
- (vi) The different flavours of  $J$ -factors that have been evaluated – the original  $J$  which doesn't take Sommerfeld enhancement into account,  $S(v^*)J$  which does so, but assumes  $P_{x,\text{rel}} = \delta(v - v^*)$  and  $J_S$ , which is the one derived in this thesis.
- (vii) The negative log likelihood function  $-\mathcal{L}$  for parameter space  $r_0, v_0$ , as defined in section 7.3.
- (viii) The minimization of this  $-\mathcal{L}$  used to find the maximum likelihood estimate.
- (ix) The calculation of a grid of  $\mathcal{L}, J$  and  $J_S$  over a parameter space in  $r_0, v_0$  for a chosen galaxy.
- (x) The construction of a binned likelihood function  $\mathcal{L}(J)$  or  $\mathcal{L}(J_S)$  from such a grid.

The code has been edited and significantly reduced before publishing, meaning that some minor errors may have trickled in. Nevertheless, most of the code supplied in this chapter correspond more or less exactly to the code that was run for this thesis.

## E.1 Eddington Formula

```

ClearAll["Global'*"];
G = 4.30227*10(-6) (*kpc/solarmass * (km/s)2 *)

(*NFW density distribution*)
rho[x_] := 1/(x (1+x)2);
Drho[x_] = D[rho[x],x];
DDrho[x_] = D[rho[x],{x, 2}];

(*Dimless gravitational potential for an NFW dSph*)
Psi[x_] := Piecewise[ {{4Pi Log[1+x]/x, x>1*-7}, {4Pi(1-x/2),x<=1*-7}}];
DPsi[x_] = D[Psi[x],x];
DDPsi[x_] = D[Psi[x],{x, 2}];

(* The integrand in the Eddington formula *)
f[x_, eps_] := ( Drho[x] DDPsi[x]/DPsi[x]2-DDrho[x]/DPsi[x])/Sqrt[Abs[eps-
  Psi[x]]];

(*Finds the lower limit of integration xmin for a given relative energy eps
*)
xmin[eps_?NumericQ] := x/. Assuming[x >0,
  FindRoot[
    SetPrecision[Psi[x] - eps + 1*-40, 64],
    {x, 1/eps},
    WorkingPrecision->64,
    PrecisionGoal->50,
    AccuracyGoal->Infinity
  ]
];

(* Evaluates the Eddington formula *)
FF[eps_?NumericQ] := Re[NIntegrate[
  f[x, eps],
  {x, xmin[eps], Infinity},
  MaxRecursion->250,
  WorkingPrecision->64,
  Exclusions->xmin[eps]==x,
  Method->{
    "GlobalAdaptive",
    "SingularityDepth"->10000,
    "SymbolicProcessing"->0
  }
]];

(*
  Spacing function for points to be interpolated over.
  We want many points in the end of the spectrum, because of the
  singularity in the integrand
*)
EpsN[n_, NN_] := (4Pi-1*-20) 1/(1+Exp[(NN/4-n)/(NN/42)]);

(*A rudimentary attempt to remove the singularity in eps -> Psi[0]*)
EE[eps_] := 1/(4Pi-eps)(9999/10000);

(*

```

```
    Checks if Machine Precision is sufficient to separate most densely
    spaced points in interpolation
*)
EpsNWorks[NN_]:=N[12+N[EpsN[NN,NN]-EpsN[NN-1,NN] , 40], MachinePrecision
]-12!=0
t0 ={{0,0}};
t1 = ParallelTable[{N[EpsN[n]], N[FF[EpsN[n]]/EE[EpsN[n]]]}, {n, 0,N}];
t =Join[t0, t1];
Export["interp/F_Eddington_cusp.csv", t];
SetDirectory[NotebookDirectory[]];
(*Slight cheat in not including imaginary part *)
Export["interp/F_Eddington_cusp", Re[t], "CSV"];
```

## E.2 Relative Velocity Distribution

```

ClearAll["Global'"];

G = 4.30227*10^(-6);(*kpc/solarmass * (km/s)^2 *)

(*A rudimentary attempt to remove the singularity in eps\[Rule]Psi[0]*)
EE[eps_] := 1/(4Pi-eps)^(9999/10000);

SetDirectory[NotebookDirectory[]];
TT=Import["interp/F_Eddington_cusp", "CSV"];
Fint = Interpolation[TT, InterpolationOrder->1];

(*Now, EE[eps] must be multiplied back in*)
F[eps_] = Fint2[eps]*EE[eps];

(* Prel integral *)
Pintegral[x_?NumericQ, vrel_?NumericQ] := (

  (* relative potential and density for NFW distribution*)
  psix = 4Pi Log[1+x]/x;
  rhox = 1/(x (1+x)^2) ;

  (*Epsilon in vcm and vrel*)
  Epsrel[vcm_, z_] := Epsrel[vcm,z] = psix-vcm^2/2 -vrel^2/8 + vcm vrel z
    /2;
  NEpsrel[vcm_, z_] := NEpsrel[vcm,z] = psix-vcm^2/2 -vrel^2/8 - vcm vrel
    z/2;

  (*Limits of integration*)
  skew = 10^(-30);
  vcmMin1 = 0 + skew;
  vcmMin2 = Sqrt[2psix] - vrel/2 + skew;
  vcmMax1 = Sqrt[2psix] - vrel/2;
  vcmMax2 = Sqrt[8psix - vrel^2]/2;

  zMax2[vcm_] := (8psix - vrel^2 - 4 vcm^2)/(4 vrel vcm);
  (*The integral itself*)
  vrel^2/rhox^2 NIntegrate[
    vcm^2
    F[NEpsrel[vcm, z]]
    F[Epsrel[vcm, z]],
    {vcm, vcmMin1, vcmMax1},
    {z, 0, 1},
    AccuracyGoal->6,
    PrecisionGoal->6,
    Exclusions->{Epsrel[vcm,z]==4Pi,NEpsrel[vcm,z]==4Pi},
    Method->{"InterpolationPointsSubdivision"}
  ] + NIntegrate[
    vcm^2
    F[NEpsrel[vcm, z]]
    F[Epsrel[vcm, z]],
    {vcm, vcmMin2, vcmMax2},
    {z, 0, zMax2[vcm]},
    AccuracyGoal->6,
    PrecisionGoal->6,

```

```
Exclusions->{Epsrel[vcm,z]==4Pi,NEpsrel[vcm,z]==4Pi},
Method->{"InterpolationPointsSubdivision"}
]
);

(*Compile the integral for slightly faster calculations*)
cPintegral = Compile[{x,vrel}, Evaluate[Pintegral[x,vrel]]];
(*Limits of vrel*)
vrelMax[x_] = 2Sqrt[2Psi[x]];
vrelMax0 = Limit[vrelMax[x],x->0];
(* Construct and export table over Prel *)
PintT = Table[
  {
    x^10,
    vrel^4,
    Piecewise[{
      {cPintegral[x^10,vrel^4], vrel^4<= vrelMax[x^10]},
      {0, vrel^4 >vrelMax[x^10]}
    ]
  },
  {x,1*^-7^(1/10), 50^(1/10), 0.02},
  {vrel, 0, vrelMax0^(1/4), 0.02}
];
fPintT = Flatten[PintT, 1];
SetDirectory[NotebookDirectory[]];
Export["interp/P_rel_cusp", fPintT, "CSV"];
```

### E.3 Sommerfeld Enhancement factor

```

ClearAll["Global'*"]
epsilon = 1*^-100;
alpha = 1/100;
vmin = 10^(-7); (*only lower limit of vel dist we want*)
vmax = 0.1;
(*mph is mediator particle mass, m is DM particle mass, mphdivm = mph/m
*)

(*limits for mphdivm *)
mmin = 3*^-7;
mmax = 11/3;

(* a = alpha/v/2 comes from that we don't use reduced mass for m *)
a[v_] = alpha/v/2;

b[mphdivm_, v_] = mphdivm/v;

(*Solve the reduced SE and return the sommerfeld enhancement as S(vrel,
mph/m) *)
S = ParametricNDSolveValue[
{
  y''[x] + (2/x) y'[x] + (1 + 2/x*a[v] Exp[-x b[mphdivm, v]]) (y[x])
    == 0,
  y[epsilon] == 1, y'[epsilon] == -a[v]
},
(1/((30*y[30])^2 + ((30 - 0.5 Pi)*y[30 - 0.5 Pi])^2)),
{x, epsilon, 30},
{v, mphdivm},
MaxSteps -> Infinity
];

LogLogPlot[S[v, 1/650], {v, vmin, vmax}]
points = 1000000;
vpoints = 500;
mpoints = points/vpoints;
deltav = (Log10[vmax] - Log10[vmin])/vpoints;
deltam = (Log10[mmax] - Log10[mmin])/mpoints;
vt = RandomReal[{1*^-7, 1*^-6}]; mt = RandomReal[{3*^-7, 1*^-5}];

(*create interpolating function*)
tab = Flatten[
  ParallelTable[
    {10^v, 10^mpdivm, S[10^v, 10^mpdivm]},
    {v, Log10[vmin], Log10[vmax], deltav},
    {mpdivm, Log10[mmin], Log10[mmax], deltam}
  ], 1];
sommer = Interpolation[tab, InterpolationOrder -> 1]

(* Store interpolating function *)
SetDirectory[NotebookDirectory[]];
sommer = Interpolation[tab, InterpolationOrder -> 1]
DumpSave["interp/Sommermint1div30.mx", sommer]

```

## E.4 Line of Sight Velocity Dispersion

```
(*
  This interpolates velocity dispersion sigma2 without a factor
  v0^2 in front.
  The variables used for interpolation are
  x = r/r0
  Rdivr0 = R/r0
  r0divrstar = r0/rstar
*)
ClearAll["Global'*" ]

(*Luminosity profile, Plummer or gen. Hernquist (2,5,0)*)

nu[x_] := (1 + x^2)^(-5/2);

(*Id2 = I(R)/2*)
Id2[Rdivrstar_] = Assuming[RR > 0,
  Integrate[nu[r]*r/Sqrt[r^2 - RR^2], {r, RR, Infinity}]
] /. RR -> Rdivrstar

Hernquist[alpha_, beta_, gamma_, x_] :=
  x^-gamma (1 + x^alpha)^(-((beta - gamma)/alpha));

(*Hernquist[1,3,1,x] for NFW, Hernquist[1,3,0,x] for core *)

rho[x_] := Hernquist[1, 3, 1, x];

(*reduced mass within reduced radius x*)

m[x_] = Assuming[x > 0 , 4 Pi Integrate[s^2 rho[s], {s, 0, x}]]

exp = r/Sqrt[r^2 - Rdivr0^2]*nu[s*r0divrstar]/s^2*m[s]

(*change of variable r to r^2+Rdivr0 to remove singularity*)

sigmared[Rdivr0_, r0divrstar_] := r0divrstar/Id2[Rdivr0*r0divrstar]
  NIntegrate[
    ( 2 (Rdivr0 + r^2) m[s] nu[r0divrstar s]) / (s^2 Sqrt[2 Rdivr0 + r^2]),
    {r, 0, Infinity},
    {s, r^2 + Rdivr0, Infinity},
    AccuracyGoal -> 6,
    PrecisionGoal -> 6,
    MaxRecursion -> 250,
    MinRecursion -> 50
  ];

sigma2tab = Flatten[ParallelTable[
  {Rdivr0^10, r0divrstar^10, sigmared[Rdivr0^10, r0divrstar^10]},
  {Rdivr0, 10^(-5/10), 500^(1/10), 0.0025},
  {r0divrstar, 10^(-2/10), 1000^(1/10), 0.0025}
], 1];

(*Here it would probably have been better to use InterpolationOrder->1*)
sigma2i = Interpolation[sigma2tab];
```

## E.5 Integral over relative velocity

```
(*
  Creates an interpolation of Gamma[x, v0], excluding the constant before
  Prel.
  Both a v0-dependent single-mass and a mass-dependent single-v0
  interpolation is created.
*)
ClearAll["Global`*"]
SetDirectory[NotebookDirectory[]]
c = 299792.458; (*km/s*)
(* Setup Prel(vrel) file according to desired profile *)
profile = "cusp";
PrelFile = If[profile == "core", "interp/P_rel_core", "interp/P_rel_cusp"];

(*load sommerfeld for single mass*)
<< "interp/Sommerldiv100single.mx";
(*
  rename sommer to sommersinglem since the mass-dependent
  sommerfeld interpolation has the same variable name
*)
sommersinglem = sommer;
(* Extends sommerfeld function to lower speeds *)
Sommer[x_] := Sommer[x] = Piecewise[{
  {sommersinglem[1*^-7], x < 1*^-7},
  {sommersinglem[x], 1*^-7 <= x < 0.1},
  {0, x > 0.1}
}];

(*load mass dependent sommerfeld*)
<< "interp/Sommermintldiv100.mx"
sommer
Sommerm[v_, m_] := Sommerm[v, m] = Piecewise[{{sommer[1*^-7, m], v <
  1*^-7}, {sommer[v, m], 1*^-7 <= v < 0.1}, {0, v > 0.1}}];

(* Load Prel(vrel) *)
PrelTab = SetPrecision[Import[PrelFile, "CSV"], MachinePrecision];
vrelmaxDimless = Max[PrelTab[[All, 2]]];
vrelmax[v0_] := v0 vrelmaxDimless;

(* highest x-value in Prel data *)
xmax = Max[PrelTab[[All, 1]]];
PrelInterp = Interpolation[PrelTab, InterpolationOrder -> 1];

(* Rudimentary extension beyond limits of Prel interpolation *)
PrelDimless[x_, vrel_] := PrelDimless[x, vrel] =
  Piecewise[{
    {
      PrelInterp[x, vrel],
      5*^-6 < x <= xmax && 0 < vrel <= vrelmaxDimless
    },
    {0, x > xmax || x < 0},
    {
      PrelInterp[5*^-6, vrel],
      0 <= x <= 5*^-6 && 0 <= vrel <= vrelmaxDimless
    }
  }
```

```
    ]];

(* defines gamma for single-mass and massdependent Sommerfeld *)
gamma[x_, v0_] := NIntegrate[
  PreDimless[x, vrel/v0] Sommer[vrel/c],
  {vrel, 0, vrelmax[v0]},
  Method -> {"GlobalAdaptive", "SymbolicProcessing" -> 0},
  AccuracyGoal -> 6,
  PrecisionGoal -> 6,
  MaxRecursion -> 20
];

gammam[x_, v0_, m_] := NIntegrate[
  PreDimless[x, vrel/v0] Sommerm[vrel/c, m],
  {vrel, 0, vrelmax[v0]},
  Method -> {"GlobalAdaptive", "SymbolicProcessing" -> 0},
  AccuracyGoal -> 6,
  PrecisionGoal -> 6,
  MaxRecursion -> 20
];

(*
  Creates a table for single-mass Gamma
*)
points = 20000;
xmin = 0;
xmax = 50;
v0min = 1;
v0max = 80;
deltax = N[(xmax^(1/6) - xmin^(1/6))/Sqrt[points]]
deltav0 = N[(v0max - v0min)/Sqrt[points]]

ptable = ParallelTable[
  {x^6, v0, gamma[x^6, v0]},
  {x, xmin^(1/6), xmax^(1/6), deltax},
  {v0, v0min, v0max, deltav0}
];
Export["interp/gamma_" <> profile <> ".csv", Flatten[ptable, 1]];

(* Creates a table for massdependent Gamma at Sculptor's MLE *)
xmin = 0;
xmax = 50;
v00 = 13.160371122115722;
v0min = 1;
v0max = 80;
mmin = 5*^-6;
mmax = 1.1;
deltax = N[(xmax^(1/6) - xmin^(1/6))/180]
deltam = N[(Log10[mmax] - Log10[mmin])/300]

ptable = ParallelTable[
  {x^6, 10^m, gammam[x^6, v00, 10^m]},
  {x, xmin^(1/6), xmax^(1/6), deltax},
  {m, Log10[mmin], Log10[mmax], deltam}
];
Export["interp/gammam_" <> profile <> ".csv", Flatten[ptable, 1]];
```

## E.6 J-factors

```

Clear[Js]
SetDirectory[NotebookDirectory[]];
G = 4.30227*10^(-6);(*kpc/solarmass * (km/s)^2 *)

<< "interp/Sommer1div100single.mx"
Hernquist[alpha_,beta_, gamma_, x_] := x^-gamma (1+x^alpha)^(-((beta-gamma)/
  alpha));

(* set up rho for core and cusp DM *)
rhoCore[x_] = Hernquist[1,3,0,x];
rhoCusp[x_] = Hernquist[1,3,1,x];

(* Import Gamma interpolation for core and cusp *)
gammaCoretab = Import["interp/gamma_core.csv"];
gammaCoreInt = Interpolation[gammaCoretab, InterpolationOrder->1];
gammaCore[x_, v0_] := gammaCore[x, v0] = gammaCoreInt[x,v0];
gammaCusptab = Import["interp/gamma_cusp.csv"];
gammaCuspInt = Interpolation[gammaCusptab, InterpolationOrder->1];
gammaCusp[x_, v0_] := gammaCusp[x, v0] = gammaCuspInt[x,v0];
xmaxCore = Max[gammaCoretab[[All, 1]]];(* highest x-value in Prel data *)
xmaxCusp = Max[gammaCusptab[[All, 1]]];(* highest x-value in Prel data *)

(* *)
r[s_, d_, cosalpha_] := Sqrt[d^2 + s^2 - 2d s cosalpha];

(* Sommerfeld-enhanced J factor, with Pr(vrel) derived from Eddington *)
Js[r00_ ?NumericQ, v00_ ?NumericQ, dd_ ?NumericQ, prof_] := Module[
  {r0 = r00, v0=v00, d=dd, profile=prof},
  If[profile=="core",
    rho = rhoCore;
    gamma = gammaCore;
    xmax = xmaxCore;
  ,
    rho = rhoCusp;
    gamma = gammaCusp;
    xmax = xmaxCusp
  ];

(*
  unitfactor is for conversion from astronomical units to GeV/cm^5
*)
unitfactor = 4.4476653533889630255052795'6.648848047656568*^6;
(*
  The constant is
  2/(pi^2v0) from Prel, times
  (v0^2/(G r0^2))^2 from rho, times
  2pi from cylindrical symmetry of J
*)
smin =N[d-xmax r0];
smax =N[d+xmax r0];
Log10[unitfactor NIntegrate[
  4/pi v0^3/(G^2 r0^4) rho[r[s, d, cosalpha]/r0]^2
  gamma[r[s, d, cosalpha]/r0,v0],
  {s,smin, smax},

```

```

    {cosalpha, Cos[0.5Degree], 1},
    MaxRecursion->200,
    Method -> {
        "GlobalAdaptive",
        "SymbolicProcessing" -> 0,
        "SingularityDepth" -> 10000,
        "MaxErrorIncreases" -> 3000
    },
    AccuracyGoal->4,
    PrecisionGoal->4
  ]]
];

(* Sommerfeld enhanced J-factor using characteristic velocity *)
SJ[r00_ ?NumericQ, v00_ ?NumericQ, dd_ ?NumericQ, prof_] := Module[
  {r0 = r00, v0=v00, d=dd, profile=prof},
  If[profile=="core",
    rho = rhoCore;
    gamma = gammaCore;
    xmax = xmaxCore;
  ,
    rho = rhoCusp;
    gamma = gammaCusp;
    xmax = xmaxCusp
  ]];

(*
unitfactor is for conversion from astronomical units to GeV/cm^5
*)
unitfactor = 4.4476653533889630255052795'6.648848047656568*^6;
(*
The constant is
(v0^2/(G r0^2))^2 from rho, times
2pi from cylindrical symmetry of J
*)
smin =N[d-xmax r0];
smax = N[d+xmax r0];
Log10[unitfactor sommer[1*^-5] NIntegrate[
  2 Pi v0^4/(G^2 r0^4) rho[r[s, d, cosalpha]/r0]^2,
  {s,smin, smax},
  {cosalpha, Cos[0.5Degree], 1},
  MaxRecursion->200,
  Method -> {
    "GlobalAdaptive",
    "SymbolicProcessing"->0
  },
  AccuracyGoal->4,
  PrecisionGoal->4
  ]]
];

(* J factor for cold dark matter - no sommerfeld enhancement *)
Jorig[r00_ ?NumericQ, v00_ ?NumericQ, dd_ ?NumericQ, prof_] := Module[
  {r0 = r00, v0=v00, d=dd, profile=prof},
  If[profile=="core",
    rho = rhoCore;

```

```

    gamma = gammaCore;
    xmax = xmaxCore;
    ,
    rho = rhoCusp;
    gamma = gammaCusp;
    xmax = xmaxCusp
];

(*
unitfactor is for conversion from astronomical units to GeV/cm^5
*)
unitfactor = 4.4476653533889630255052795'6.648848047656568*^6;
(*
The constant is
(v0^2/(G r0^2))^2 from rho, times
2pi from cylindrical symmetry of J
*)
smin =N[d-xmax r0];
smax = N[d+xmax r0];
Log10[unitfactor NIntegrate[
  2 Pi v0^4/(G^2 r0^4) rho[r[s, d, cosalpha]/r0]^2,
  {s,smin, smax},
  {cosalpha, Cos[0.5Degree], 1},
  MaxRecursion->200,
  Method->{
    "GlobalAdaptive",
    "SymbolicProcessing"->0,
    "SingularityDepth"->10000
  },
  AccuracyGoal->4,
  PrecisionGoal->4
]]
];

```

## E.7 Log Likelihood function

```
(*
  Assuming variables galaxyName and profile have been set,
  this piece of code imports velocity data for the selected galaxy
  and declares one LogLikelihood function Likely[r0,rstar,v0] over three
  parameters,
  and one Likel[r0, v0], which is the three-parameter version minimized
  over rstar
*)

Clear[Likely, Likel]
SetDirectory[NotebookDirectory[]];

(*
  The naming convention we used in this work
  cusp => no suffix, core => suffixed by _core
*)
file=galaxyName<>"_"<>profile;
If[profile!="core", profile=""; file = galaxyName];

(* Import params, and veldata *)
params = Import["data/params/params_"<>galaxyName<>".dat"];
veldata = Import["data/velocities/velocities_"<>galaxyName<>".dat"];
(* Import the limits on r0, v0 which are defined in a separate file *)
limits = Import["limits/limits_"<>file<>".dat"];

(* Import the velocity dispersion interpolation, according to DM profile *)
If[profile=="core", <<"interp/sigmacorenew.mx", <<"interp/sigmacuspnew.mx"
];
G=4.30227*10^(-6);

(* half light radius *)
rhalf = params[[3, 1]];
(*mean velocity of stars in galaxy *)
meanvel = Part[Mean[veldata],2];

(* measured velocity dispersion vector for galaxy *)
v2 = (veldata[[All, 2]]-meanvel)^2;

(* Setup DM and baryonic density profiles *)
dmHernquist =If[profile=="core", {1,3,0}, {1,3,1}];
Hernquist[alpha_,beta_, gamma_, x_]:= x^-gamma (1+x^alpha)^(-((beta-gamma)/
alpha));

rho[x_] := Hernquist[dmHernquist[[1]],dmHernquist[[2]],dmHernquist[[3]],x];
nu[x_] := Hernquist[2,5,0,x];

(* construct theoretical sigma2 function from interpolated one *)
sigma2[R_, r0_ , rstar_ , v0_] :=v0^2 sigma2i[R/r0,r0/rstar];

(*
  Here is the likelihood function.
  The If statement excludes for values that are considered too
  implausible
*)
```

```

*)
Likely [r0_ ,rstar_ ,v0_ ] := (
  If[rstar < 10^-6 || rstar > 3rhalf
    || v0 < 0 || r0 < 10^-6 || r0/rstar < 0.001 || r0/rstar > 1000,
    10^10,
    (
      sigma2tot = sigma2[velformat[[All,1]],r0,rstar,v0] + velformat
        [[All,3]]^2;
      1/2 Total[v2/sigma2tot + Log[2\[Pi] sigma2tot]]
    )
  ]
);

(*
  This is the function that is mainly used to calculate Likelihood
*)
Likel[r0_ , v0_] := Flatten[
  {#[[1]], rstar/#[[2]]} &/@ {
    Flatten[FindMinimum[
      {Likely[r0, rstar, v0]},
      {rstar, 0.1rhalf, 0.2rhalf},
      Method->"PrincipalAxis"
    ]
  ]
  }
];

```

## E.8 Maximum Likelihood Estimate

```
(* Finds the MLE in r0,rstar,v0 space *)
minpoint = NMinimize{
    Likely[r0, rstar, v0],
    v0min<v0<v0max && r0min<r0<r0max && 0.0001<rstar<2rhalf
},
    {r0, rstar, v0},
    Method->"DifferentialEvolution",
    MaxIterations->80,
    AccuracyGoal->10
];

(* Exports the found MLE to file *)
r00 = minpoint[[2,1,2]];
rstarr = minpoint[[2,2,2]];
v00 = minpoint[[2,3,2]];
Jmle = J[r00, v00, DD];
SetDirectory[NotebookDirectory];
Export["likely/"<>file<>"_minpoint.csv", {minpoint[[1]],r00, rstarr, v00,
    Jmle}];
```

## E.9 Tabulation of Likelihood and J-factors

```
galaxyName = "scl";
profile = "cusp";
file = If[profile == "core", galaxyName<>"_"<>profile, galaxyName]
(* Imports likelihood function *)
<<"likely.m"
(* Imports J functions *)
<<"Js.m"

(* Creates table of r0, v0, L, rstar, J, Js *)
tab = Flatten[Table[
    Flatten[
        {
            r0,
            v0,
            Likel[r0, v0],
            Jorig[r0,v0,DD, profile],
            Js[r0,v0,DD, profile]
        }
    ],
    {r0,r0min,r0max, deltar0},
    {v0,v0min, v0max, deltav0}
],1];
Export["likely/"<>file<>"_Jslikely.csv", tab]
```

## E.10 Construction of confidence levels

```
(* Creates a Latex table of dSph J-factors and 1sigma errors from tabulated
data*)
ClearAll["Global`*"]
SetDirectory[NotebookDirectory[]];
(* Finds all dSphs for which there is velocity data *)
galaxies = StringReplace[FileNames["*.dat", NotebookDirectory[] <> "data/
params/"], {NotebookDirectory[] <> "data/params/" -> "", ".dat" -> "" }];

(* Counts the number of stars in a dSph for which there is velocity data *)
NStars[galaxy_] := Length[Import["data/velocities/velocities_" <> galaxy <> ".
dat"]];

(* Represent a confidence level with n degrees of freedom *)
confidence[n_, p_] := 1/2 Quantile[ChiSquareDistribution[n], p];
(* 1sigma confidence level *)
sigma = confidence[1, 0.683];
(* Imports a list of galaxy names *)
GalaxyNames = Import["data/galaxies.dat", "CSV"];
(* Gets the name of a galaxy from its short name *)
Name[galaxy_] := SelectFirst[GalaxyNames, #[[1]] == galaxy &][[2]];

galaxies = SortBy[galaxies, NStars]
(* Import J functions *)
<<"Js.m"

(* Constructs a binned likelihood function from the given table, for the
given J factor type *)
BinnedLikelihood[T_, Lmin_, JFactor_] := (
Jindex = If[JFactor == "Js", 6, 5];
JT = {#[[Jindex]], #[[3]] - Lmin} & /@ T;
minJ = Min[JT[[All, 1]]];
maxJ = Max[JT[[All, 1]]];
(* Each bin should have around 40 data points *)
binwidth = 40(maxJ - minJ) / Length[JT];
(* No need to go beyond 0.01 in precision *)
binwidth = If[binwidth < 0.01, 0.01, binwidth];
T2 = Flatten[BinLists[
JT,
{minJ, maxJ, binwidth},
{0, confidence[1, 0.999], confidence[1, 0.999]}
], 1];
T2 = Replace[T2, x_List :> DeleteCases[x, {}], {0, Infinity}];
Second[x_] := x[[2]];
Minvals = Flatten[MinimalBy[#, Second] & /@ T2, 1]
);

(* Finds the 1sigma constraints on the JFactor given as argument, for the
given table T *)
Binned1sigma[T_, Lmin_, JFactor_] := (
lik = Select[BinnedLikelihood[T, Lmin, JFactor], #[[2]] < sigma &];
{
MinimalBy[lik, #[[1]] &][[1, 1]],
MaximalBy[lik, #[[1]] &][[1, 1]]
}
)
```

```

);
(*
  J calculates and returns the MLE with 1sigma error bars for a given
  profile and Jfactor type.
  The return is formatted as LaTeX.
*)
Options[J]= {Profile->"cusp", JFactor->"Js"};
J[galaxy_, OptionsPattern[]]:= (
  file=If[OptionValue[Profile]=="cusp", galaxy, galaxy<>"_core"];
  mle = Import["likely/"<>file <>"_minpoint.csv"];
  params = Import["data/params/params_"<>galaxy<>".dat"];
  limits = Import["limits/limits_"<>file<>".dat"];
  T = Import["likely/"<>file<>"_Jslikely.csv"];
  r0max = limits[[3,1]];
  r0min = limits[[2,1]];
  v0max = limits[[5,1]];
  v0min = limits[[4,1]];
  (* Remove points outside of limits *)
  T = Select[T, r0min <=#[[1]]<=r0max && v0min <=#[[2]] <= v0max &];

  (* Find the MLE in the grid *)
  minT = MinimalBy[T, #[[3]]&][[1]];

  (* Sometimes the points in the grid are lower than the free MLE, choose
  the one that is lowest *)
  If[mle[[1,1]]< minT[[3]]
    && v0min < mle[[4,1]] < v0max
    && r0min < mle[[2,1]] < r0max,
    Lmin = mle[[1,1]];
    v0mle = mle[[4,1]];
    r0mle = mle[[2,1]];
    Lmin = minT[[3]];
    v0mle = minT[[2]];
    r0mle = minT[[1]];
  ];

  d = params[[2,1]];
  (* Sets which J function to use *)
  Jfun = If[OptionValue[JFactor]=="Js",
    Js,
    If[OptionValue[JFactor]=="J",
      Jorig,
      SJ
    ]
  ];
  Jmle = Jfun[r0mle,v0mle, d, OptionValue[Profile]];
  If[OptionValue[JFactor]=="SJ",
    "$"<>ToString[NumberForm[Jmle, {Infinity,2}]]<>"$",
    pm= Binned1sigma[T, Lmin, OptionValue[JFactor]]-Jmle;
    "$"<>ToString[NumberForm[Jmle, {Infinity,2}]]
    <>"_{"<>ToString[NumberForm[pm[[1]],{Infinity,2}]]
    <>"^{"<>ToString[NumberForm[pm[[2]],{Infinity,2}]]
    <>"}$"
  ]
);

```

---

```

(* Constructs a table row containing all J factors for a galaxy *)
Jrow[galaxy_] := ToString[Row[
  {
    Name[galaxy], ToString[NStars[galaxy]],
    J[galaxy, Profile->"cusp", JFactor->"J"],
    J[galaxy, Profile->"cusp", JFactor->"SJ"],
    J[galaxy, Profile->"cusp", JFactor->"Js"],
    J[galaxy, Profile->"core", JFactor->"J"],
    J[galaxy, Profile->"core", JFactor->"SJ"],
    J[galaxy, Profile->"core", JFactor->"Js"]
  },
  "&"]
]]<>"\\\\"n";

(* Goes through all galaxies and constructs a table *)
tab = "";
Do[tab = tab<>Jrow[galaxies[[i]]];, {i, 1, Length[galaxies]};
(* Export the table *)
Export["Jtable.txt", tab]

```